



MECHANISTIC STUDIES OF THE HYDROGENATION OF IMINO BONDS

Thesis submitted in accordance with the requirements
of the University of Liverpool for the degree of Doctor in Philosophy

by

Steven Johnston

September 2013

Acknowledgements

First of all, I am very thankful to my supervisor Professor Jianliang Xiao for giving me the opportunity to carry out a PhD within such a great group. I am indebted to your guidance and ability to motivate me throughout the four years.

I would also like to thank my other supervisors Dr Jon Iggo and Dr Neil Berry for their guidance and teaching over the course of the research. Your help and advice during the countless hours of analysing data was invaluable. Thanks also go to Professor Luyun Lian and Dr Marie Phelan for their assistance and time in helping me when working in the biology department.

One of the best parts about working in a research group is the people you meet and work with during the PhD and I have had the pleasure of working with a wonderful group. Thanks to Weijun for being a brilliant postdoc to work with, your drive and ability showed me the level I needed to achieve. To Barbara for your help and making me laugh in the office. To Jonathan for the many discussions on chemistry and infrequent badminton. To Ángela and Dinesh for keeping me sane in the office. Thanks also to Jianjun, Jen, Ed, Chao, Paul, Xiaofeng, Mike and group members past and present.

I am eternally grateful to my parents for their constant support throughout my life. The encouragement you have given me to achieve as much as I could is the reason I have managed to go so far and I am indebted for you being there whenever I needed you. The same also goes to my brother who has supported me throughout. Thanks also to my grandparents for the part they have played in helping me achieve my goals. I am also grateful to all my friends who have supported me over the past four years.

Finally the biggest thanks of all goes to my wonderful girlfriend Jenna, who has been the most important and supportive person throughout the past eight years. There is no way I could have got this far without you. When I doubted I could do this you were the one who told me I could, you always cheered me up when I was down and have been there no matter what happened. I am forever grateful for all you have done.

Abstract

The reduction of imino bonds produces highly valuable amine products of significance in a range of industries. The development of new systems for their production relies on knowledge of the mechanisms for these catalytic processes. While the mechanisms have been widely studied for metal catalysed asymmetric hydrogenation there is much less work for the emerging area of metal–Brønsted acid cooperative catalysis. Chapter 1 describes the recent developments in both metal catalysed and organocatalysed asymmetric reduction of imines with an emphasis on the mechanistic details. This will be followed by the mechanistic studies carried out for the reduction of imino bonds.

Chapter 2 describes the development of a new cooperative achiral metal–Brønsted acid system for the asymmetric reduction of imines with high ee's. There then follows the mechanistic study which shows that the chiral Brønsted acid plays a dual role in protonating the catalyst and mediating the key hydride transfer step, through hydrogen bonding. The hydrides of the catalyst are shown to be formed in a mixture of *cis* and *trans* orientations but only the *cis* hydride carries out the enantioselective reaction.

Chapter 3 describes the work carried out to identify the existence of a supramolecular structure involving the imine, Brønsted acid and catalyst. Through a combination of NMR measurements and subsequent constrained computational calculations the structure of this tertiary complex is determined. From this the *cis*- $S_{Ir}S_N$ hydride is shown to carry out the hydride transfer step with the aid of non-covalent interactions.

Chapter 4 looks at how the levels of conjugation present in a range of cyclometallated iridium (III) complexes influences their reactivity towards a range of hydrogen transfer reactions. Computational studies on the hydride transfer step for imine reduction show a combination of steric and electronic factors affect reactivity. Crucially, the ability of the ligand to stabilise the negative charge build up on the metal centre allows for higher conversions.

Publications

- **Cooperative Catalysis through Noncovalent Interactions**
Tang, W.; Johnston, S.; Iggo, J. A.; Berry, N. G.; Phelan, M.; Lian, L.; Bacsá, J.; Xiao, J.L. *Angew Chem. Int. Ed. Engl.* **2013**, 52, 1688.
Featured in Synfacts 2013, 9(5), 0519.
- **Acceptorless Dehydrogenation of Nitrogen Heterocycles with a Versatile Iridium Catalyst**
Wu, J.; Talwar, D.; Johnston, S.; Yan, M.; Xiao, J.L. *Angew Chem. Int. Ed. Engl.* **2013**, 52, 6983.
- **Cooperative Catalysis: Combining an Achiral Metal Catalyst with a Chiral Brønsted Acid Enables Highly Enantioselective Hydrogenation of Imines**
Tang, W.; Johnston, S.; Iggo, J. A.; Bacsá, J.; Xiao, J.L. *Chem. Eur. J.* **2013**, DOI: 10.1002/chem.201302437.

Definitions and Abbreviations

α	alpha
β	beta
Δ	diffusion delay
δ	chemical shift
η	solvent viscosity
\AA	angstrom
Ac	acyl
acac	acetylacetone
AOT	sodium bis(2-ethylhexyl) sulfosuccinate
ACS	American Chemical Society
aq	aqueous
Ar	aryl
ATH	asymmetric transfer hydrogenation
B3LYP	Becke, three-parameter, Lee-Yang-Parr exchange-correlation functional
BARF	tetrakis[3,5-bis(trifluoromethyl)phenyl]borate
BDPP	2,4-bis(diphenylphosphino)pentane
BINAP	2,2'-bis(diphenylphosphino)-1,1'-binaphthyl
Bn	benzyl group
Bt	benzotriazolyl
brs	broad singlet
Bu	butyl
$^{\circ}\text{C}$	degree Celsius
CI	chemical ionisation
cm	centrimetre(s)
cm^{-1}	wavenumber
COD	1,5-cyclooctadiene
conv.	conversion
COSY	correlation spectroscopy
Cp*	pentamethylcyclopentadienyl

Cy	cyclohexyl
d	doublet
<i>D</i>	Diffusion Constant
DARA	direct asymmetric reductive amination
DCE	1,2-dichloroethane
DCM	dichloromethane
DFT	density functional theory
DIOP	2,2-dimethyl-4,5-(diphenylphosphino)dimethyldioxolane
DKR	dynamic kinetic resolution
DPEN	1,2-diphenyl-1,2-ethylenediamine
DPPB	1,4-Bis(diphenylphosphino)butane
DPPP	1,3-Bis(diphenylphosphino)propane
ee	enantiomeric excess
ECP	effective core potential
eq	equivalent(s)
Et	ethyl
f-BINAPHANE	1,1'-bisphosphanoferrocene
F/T	formic acid/triethylamine mixture
GC-MS	gas chromatography-mass spectrometry
h	hour(s)
HEH	Hantzsch 1,4-dihydropyridine
Het	heterocyclic
HMBC	heteronuclear multiple-bond correlation spectroscopy
HOMO	highest occupied molecular orbital
HPLC	high pressure liquid chromatography
HRMS	high resolution mass spectrometry
HSCQ	heteronuclear single quantum correlation
Hz	hertz
<i>i</i> Pr	isopropyl
IR	infrared
<i>J</i>	coupling constant value
K	Kelvin

kT	Boltzmann constant, k, and the temperature T
kJ	kilojoules
kcal	kilocalories
<i>L</i>	levorotatory
LUMO	lowest unoccupied molecular orbital
<i>m</i>	meta
m	multiplet
Me	methyl
mg	milligram(s)
MHz	megahertz
min	minute(s)
mL	mililitre
mM	millimolar
mmol	milimole(s)
mol	mole(s)
MS	molecular sieves
<i>m/z</i>	mass to charge ratio
NBD	norbornadiene
nm	nanometre(s)
NMR	nuclear magnetic resonance
NOE	nuclear Overhauser effect
NOESY	nuclear Overhauser effect spectroscopy
<i>o</i>	ortho
OAc	acetate
o/n	overnight
<i>p</i>	para
p-cymene	1-methyl-4-(1-methylethyl)benzene
PFGSE	pulsed field gradient spin-echo
Ph	phenyl
PPY*	4-pyrrolidinopyridine
q	Quadruplet
<i>r_H</i>	hydrodynamic radius

rt	room temperature
s	singlet
s	strong
S/C	substrate to catalyst ratio
t	triplet
T1	spin lattice relaxation time
<i>t</i> Boc	<i>tert</i> -butyl carbonate
<i>t</i> Bu	<i>tert</i> -butyl
TMS	Tetramethylsilane
TFE	2,2,2-trifluoroethanol
TH	transfer hydrogenation
THF	tetrahydrofuran
TOCSY	total correlation spectroscopy
TOF	turnover frequency
Tol	<i>p</i> -methylphenyl
TON	turnover number
<i>t</i> _R	retention time
Ts	<i>p</i> -methylbenzenesulfonyl
<i>vs</i>	<i>versus</i>
μL	microliter
μs	microsecond (s)

Contents

Acknowledgements	iii
Abstract	v
Publications	vi
Definitions and Abbreviations	vii
Chapter 1: Introduction	
1.1 Importance of chiral amines	1
1.2 Methodology for chiral amine synthesis	2
1.3 Metal catalysed asymmetric hydrogenations of imines	6
- 1.3.1 Chiral rhodium metal catalyst	7
- 1.3.2 Chiral ruthenium catalysts	9
- 1.3.3 Chiral iridium metal catalysts	10
1.4 Mechanistic considerations for chiral metal asymmetric hydrogenation of imines	12
1.5 Organocatalysis asymmetric imine reduction	18
- 1.5.1 Organocatalysed DARA	19
- 1.5.2 Mechanistic considerations of organocatalysts	21
1.6 Metal–Brønsted acid cooperative catalysis	23
- 1.6.1 Metal catalysed DARA	
1.7 Catalytic supramolecular assemblies	30
1.8 Aims of the thesis	31
1.9 References	32

Chapter 2: Cooperative Catalysis: Mechanistic Studies of an Achiral Metal Catalyst Coupled with Chiral Brønsted Acid for Asymmetric Hydrogenation of Imines

2.1 Introduction	39
2.2 Results and discussion	42
- 2.2.1 Identification of catalysts	42
- 2.2.2 Asymmetric hydrogenation of acyclic aromatic imines	45
- 2.2.3 Asymmetric hydrogenation of aliphatic ketone-derived imines	48
- 2.2.4 Proposed mechanism	53
- 2.2.5 Protonation of the 16e catalyst and catalyst deactivation	55
- 2.2.6 Hydride formation	56
- 2.2.7 Importance of hydrogen bonding	62
- 2.2.8 Hydride Exchange	67
- 2.2.9 Importance of hydrogen bonding and the effect of the chiral phosphate on the rate of reaction	68
2.3 Conclusions and future work	72
2.4 Experimental	72
2.5 Analytical data	77
2.6 References	82

Chapter 3: Cooperative Catalysis: Made Possible by Noncovalent Interactions

3.1 Introduction	87
3.2 Results and discussion	91

- 3.2.1 NMR structural characterisation	91
- 3.2.2 Structural characterisation of HA and 1a	93
- 3.2.3 Structural Characterisation of HA + C	95
- 3.2.4 Structural characterisation of tertiary structure via NMR	96
- 3.2.5 Diffusion ordered spectroscopy (DOSY) of the tertiary structure	105
3.3 Conclusions and future work	117
3.4 Experimental	118
3.5 Analytical data	122
3.6 References	122

Chapter 4: Computational Studies of the effect of ligand conjugation on the activity of cyclometallated iridium (III) complexes

4.1 Introduction	125
4.2 Results and discussion	131
- 4.2.1 Ground state structures and energies	136
- 4.2.2 HOMO of ground state complexes	140
- 4.2.3 Location of transition states for the hydride transfer step	143
4.3 Conclusions and future work	151
4.4 Experimental	153
4.5 References	154

Chapter 5: Conclusions and Perspectives	158
--	------------

Chapter 1

Introduction

1.1 Importance of chiral amines

Chiral amines are an important functionality present in an array of bioactive compounds as well as having uses in agrochemical, pharmaceutical and materials products. Around one third of prescription drugs on the market are chiral with 40% of these chiral drugs on the market containing an amine moiety.^{1,2} Below (Figure 1.1) is shown some important chiral amines that are used in the pharmaceutical industry, repaglinide is used in the treatment of type II diabetes and works by stimulating the release of insulin from the pancreas.³ Rivastigmine is a parasymphomimetic or cholinergic agent for the treatment of Alzheimer's disease while tamsulosin marketed under the name Flomax, is used for the treatment of chronic prostatitis.^{4,5}

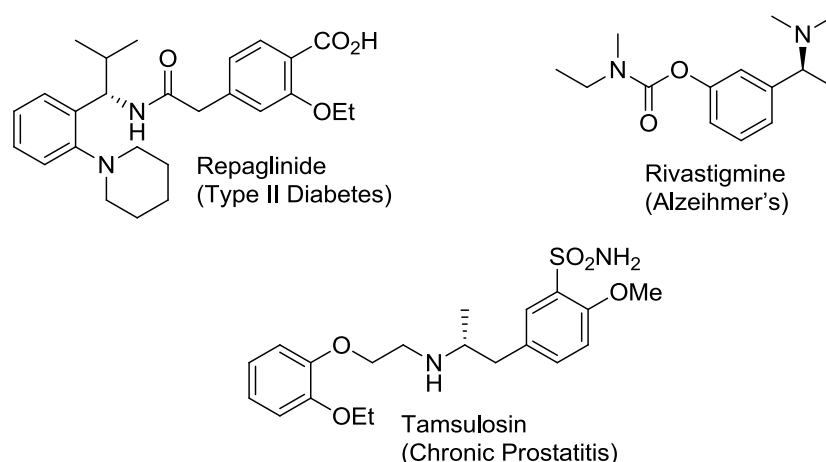


Figure 1.1: Examples of chiral amines used in the pharmaceutical industry.

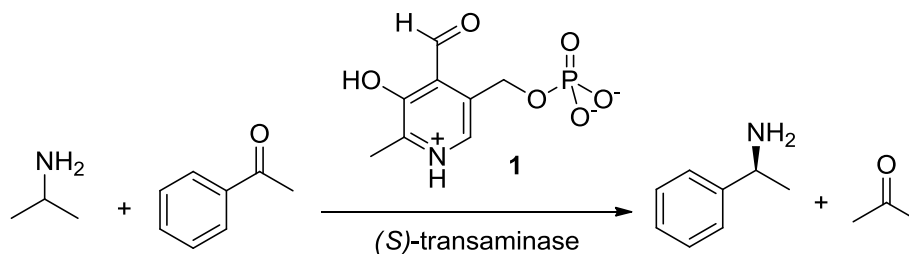
Chiral amines have also found utility in asymmetric catalysis. Amino catalysts have been demonstrated for a variety of reactions.^{6,7} In particular, *L*-proline coupled with DMTC (5,5-dimethyl thiazolidinium-4-carboxylate) was shown to catalyse the direct asymmetric aldol reaction. A variety of aldehydes and unmodified ketones were reacted giving excellent regio-, diastereo-, and enantioselectivity to form anti-1,2-diols.⁸ Amines are also prevalent through a range of ligands^{9,10} with one of the most successful being DPEN (1,2-diphenyl-1,2-ethylenediamine).¹¹

1.2 Methodology for chiral amine synthesis

The traditional route to amines yields the achiral product employing borohydrides as the reductant. The development of processes to access chiral amines with low wastage has been highlighted as a key green chemistry research area.¹² This has led to a number of methodologies being developed to form chiral amines.

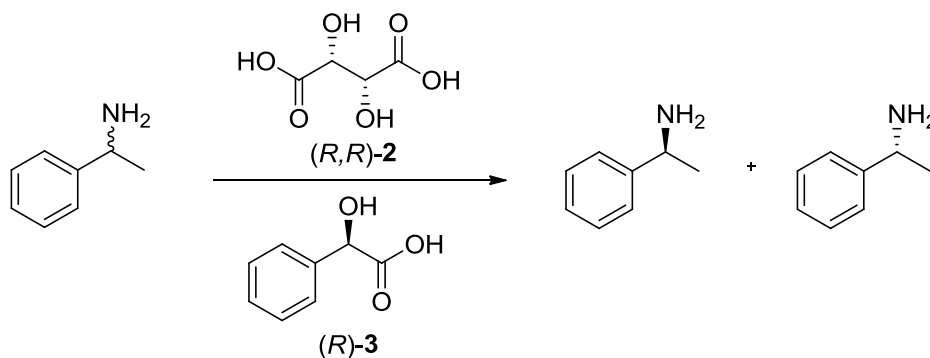
Transamination is a process that exploits enzymatic catalysis. The process was developed to form chiral amines from prochiral ketones in the presence of transaminases and cofactor pyridoxal phosphate **1** (Scheme 1.1).^{1,13} Due to the reaction being carried out in an aqueous (aq.) solution, the resultant amine products are poorly soluble; therefore low concentrations of products are attained. Recent work in this area has seen more complex enzymatic examples reported making use of direct evolutions of the enzymes to fine tune the catalyst.¹⁴ The combination of enzyme catalysis and metal co-catalysts has also been explored with yields of single enantiomers approaching 100% and a

recent mechanistic study has shown that for the Shvo catalyst an inner-sphere mechanism with metal coordination of the racemic amine is crucial in the hydrogen transfer step.^{15,16}



Scheme 1.1: Transamination of prochiral ketones by use of transaminase and cofactor **1**.

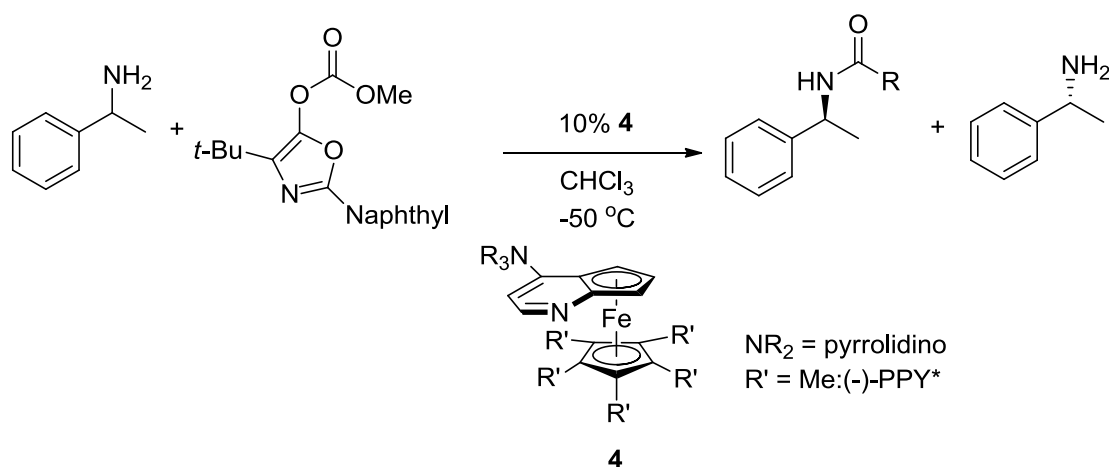
The resolution of amines via crystallisation of diastereomeric amine salts with chiral carboxylic acids such as (*R,R*)-tartaric acid **2** and (*R*)-mandelic acid **3** has been shown to form chiral amines (Scheme 1.2). However, this method suffers from a maximum yield of 50% for each enantiomer.¹



Scheme 1.2: Resolution of amines via crystallisation of diastereomeric amine salts.

This concept of resolution was extended to the kinetic resolution of amines by a nonenzymatic acylation catalyst (Scheme 1.3).¹⁷ A ferrocene

derivate **4** was used as an acylation catalyst for primary amines but again suffers from a maximum yield of 50%.



Scheme 1.3: Kinetic resolution of amines by a nonenzymatic acylation catalyst **4**. PPY= 4-pyrrolidinopyridine.

While asymmetric catalysis has proven an important method in the synthesis of chiral amines the asymmetric hydrogenation of imines remains an underused method in industry.¹ Ideally a one pot synthesis to access chiral amines from the prochiral ketone would yield a greener, more efficient process that could utilise a catalyst and a green reductant in H_2 (Figure 1.2).

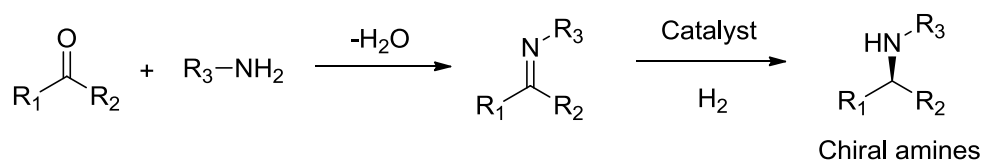


Figure 1.2: General method for imine hydrogenation.

In comparison to asymmetric imine hydrogenation, the asymmetric hydrogenation of ketones and olefins by homogeneous metal catalysis is an extensively researched area, with numerous publications utilising a range of

metals and ligands.^{18,19} This is due to the asymmetric hydrogenation of imines posing different challenges:

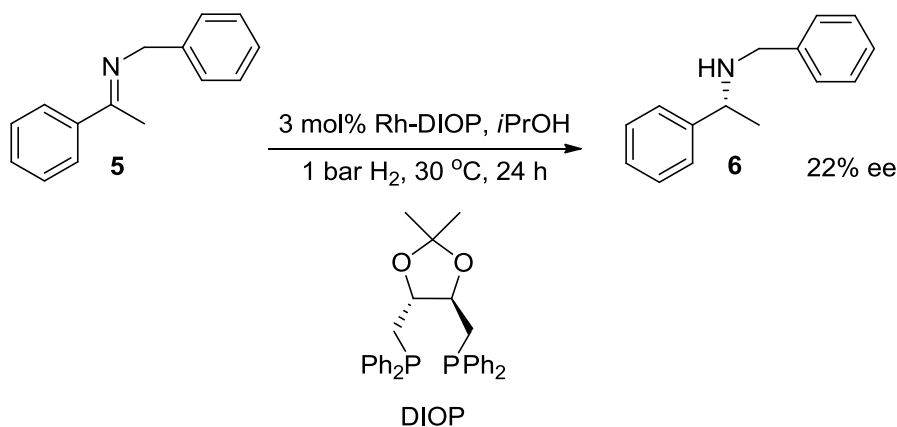
- The C=N bond has the ability to isomerise unlike the C=O bond, with a small energy barrier between the *E* and *Z* isomers.
- The C=N bond also possesses a higher lowest unoccupied molecular orbital (LUMO) compared to carbonyl and olefins, making reduction more difficult.
- The net hydrogenation processes for the reduction of C=N or C=O bonds has a smaller thermodynamic gain ($\sim 60 \text{ kJ mol}^{-1}$), relative to an olefinic bond ($\sim 130 \text{ kJ mol}^{-1}$).²⁰
- Olefins favour side on η^2 binding which allows effective overlap of the orbitals with the metal centre. However, imines and ketones tend to bind to the metal catalyst η^1 through the lone pairs on the N and O giving a less effective orbital overlap.
- Catalyst deactivation by coordination of both imine and the amine product (amines>alcohols>saturated hydrocarbons) also add to the challenges of a successful catalytic cycle.²⁰

Despite the drawback of this method the asymmetric hydrogenation of imines is a desirable process due to the atom economy, green reductant in H_2 and the straightforward nature of the methodology. The thesis will review the development of both metal and organocatalysed asymmetric hydrogenations of imines. This will then move on to the looking at the emerging area of cooperative catalysis, combining a metal catalyst with an organocatalysis.

There will be an emphasis on the mechanistic studies of the systems that have been developed.

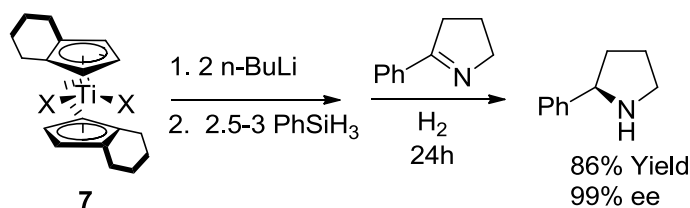
1.3 Metal catalysed asymmetric hydrogenations of imines

The first catalytic enantioselective hydrogenation of imine was reported by Scorrano in 1975.²¹ An enantiomeric excess (ee) of 22% was achieved for **6** by use of a rhodium DIOP ((2,2-Dimethyl-4,5-(diphenylphosphino)dioxolane)) complex (Scheme 1.4).



Scheme 1.4: First reported enantioselective imine hydrogenation by Scorrano.

This early result wasn't improved dramatically until the 1990s when examples like Buchwald's titanocene **7** catalyst were reported. Cyclic imines were hydrogenated in good yields and enantioselectivities (ee's) of up to 99% (Scheme 1.5).²²



Scheme 1.5: Buchwald's titanocene catalyst.

This substrate scope was then extended into acyclic imines and the mechanism was deduced by kinetics to show it being consistent with a fast 1,2-insertion step in a classical manner. The imine reacts with titanium hydride followed by the slow reaction of the amide complex with dihydrogen; this produces the amine and regenerates the titanium hydride.²³

Since this first example a wide range of chiral catalysts have been reported utilising late row transition metals.^{24,25,26,27} So far iridium has proven the most successful metal with regards to enantioselectivity but rhodium and ruthenium catalysts have found utility as well.

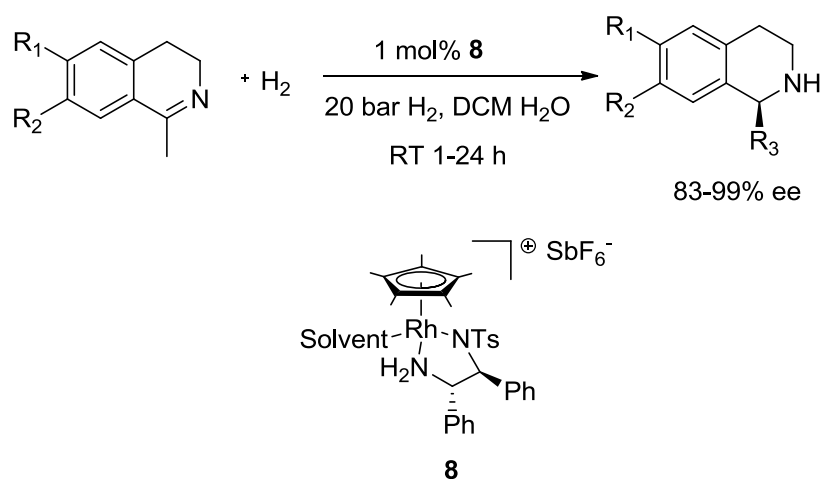
1.3.1 Chiral rhodium metal catalyst

Following the first rhodium catalyst reported by Scorrano a significant improvement was not reported until Bakos in 1991.²⁸ The system made use of a Rhodium(I)–sulfonated-bdpp (bdpp = 2,4-bis(diphenylphosphino)pentane) catalyst in an aqueous–organic two-phase solvent system. High pressures of 70 bar H₂ were required to hydrogenate **5** giving an excellent ee of 94% in 24 h.

Buriak and Osborn reported in 1996 that exploiting the presence of reverse micelles formed by AOT (AOT: sodium bis(2-ethylhexyl) sulfosuccinate) with the [Rh((*S,S*)-BDPP)(NBD)]ClO₄ catalyst (NBD:

norbornadiene) **6** could be obtained with 87% ee. Lowering the temperature from 25 °C to 4°C increased the ee to 92%, under 70 bar H₂. From these early examples a range of diphosphine ligands have since proven successful with rhodium gaining ee of up to 95%.^{29,30}

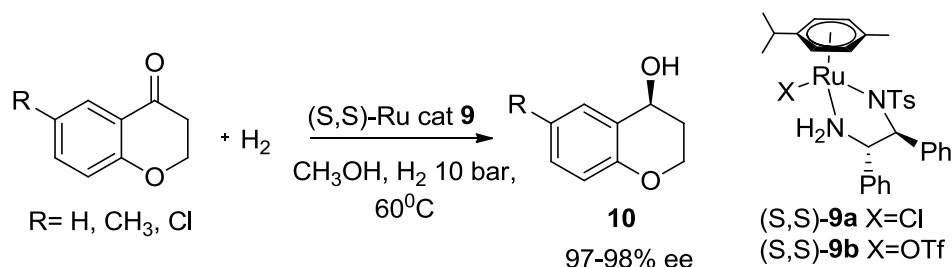
Work within the Xiao group described that an Rh-TsDPEN catalyst with an AgSbF₆ counterion could access amongst the highest ee's to date. The system reduced a range 3,4-dihydroisoquinolines and 3,4-dihydro-6,7-dimethoxyisoquinolines, giving excellent yields and ee, tolerating both electron donating and withdrawing groups (Scheme 1.6).³¹ The bulky SbF₆⁻ anion was shown to be key to the success. Changing to a smaller coordinating anion such as chloride reduced the activity of the system likely due to the anion binding to the metal centre therefore hindering hydride formation.



Scheme 1.6: Asymmetric hydrogenation of cyclic imines using a Rh-TsDPEN catalyst with an SbF₆⁻ counterion.

Noyori and co-workers had previously shown how an anion can change reactivity. When replacing the chloride in **9a** (Scheme 1.7) with a triflate anion

9b the system could be changed from asymmetric transfer hydrogenation (ATH) to asymmetric hydrogenation of ketones.³²



Scheme 1.7: ATH vs AH anion effect.

1.3.2 Chiral ruthenium catalysts

Noyori type catalysts of ruthenium diphosphine/diamine catalysts were reported by Morris for the asymmetric hydrogenation of imines.³³ The catalyst **11** was capable of hydrogenating both *N*-alkyl and *N*-aryl acyclic imines with ee's up to 71% (Figure 1.3). Key to the reaction working is the use of the base KO*i*Pr, which is likely to be involved in aiding the loss of the chloride to form HCl, allowing the catalyst to form an active dihydride species.

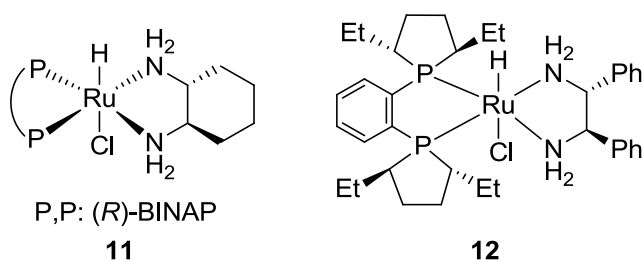
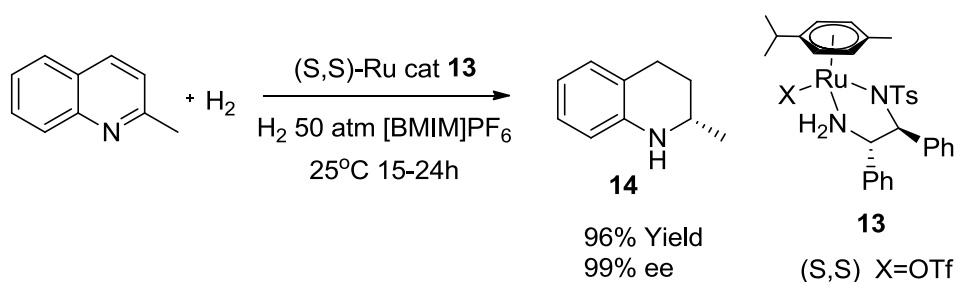


Figure 1.3: Noyori's type catalyst used for the asymmetric hydrogenation of imines.

Cobley also investigated the use of Noyori type catalysts, using **12**.³⁴ For *N*-aryl imines **12** gave a best result of 91% ee at 65 °C under 15 bar H₂ at 1 mol% catalyst, in the presence of 1 eq of base in *i*PrOH.

Chan *et al* has also shown the hydrogenation of quinolones using a Ru catalyst (Scheme 1.8) in ionic liquids, demonstrating a phosphine free system.³⁵ Using the system shown below a wide range of substrates were hydrogenated tolerating a range of electron withdrawing and donating groups. With the cyclic amine **14** being achieved in 99% ee. An ionic mechanism was predicted with a proton transfer step to form an iminium ion, followed by a hydride transfer to an iminium to form the chiral amine.

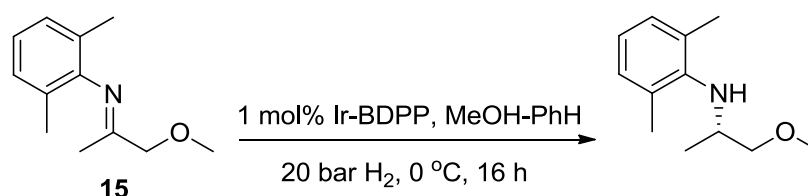


Scheme 1.8: Chan's Hydrogenation of quinolones.

1.3.3 Chiral iridium metal catalysts

In comparison to asymmetric rhodium hydrogenation catalysis there is a larger number of examples of iridium catalysis.²⁵ The earliest example of enantioselective iridium catalysed asymmetric imine hydrogenation was reported by Spindler.³⁶ A series of diphosphine ligands were tested with [Ir(COD)Cl]₂, with the catalyst being formed *in situ*. Use of the ligand (*S,S*)-BDPP yielded 84% ee for the reduction of imine **15**, with 1 mol% catalyst

loading, 20 bar H₂ at 0 °C (Scheme 1.9). The bulky *N*-aryl group was needed in order for a high ee to be achieved. This is probably due to the need for restrictive movement along for the *N*-aryl bond.



Scheme 1.9: First reported example of iridium catalysed asymmetric imine hydrogenation.

Osborn reported at the same time, the discovery of a series of iridium(III)-diphosphine-monohydrido complexes **16** (Figure 1.4) that were able to hydrogenate imines. Ligands DIOP and BDPP were found to be the most effective diphosphines for the reaction. With lower catalyst loadings of 0.2 mol% the enantioselectivities were lower, giving 22-63% ee for hydrogenation of **15**.

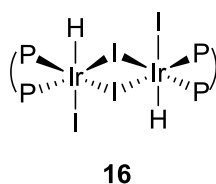
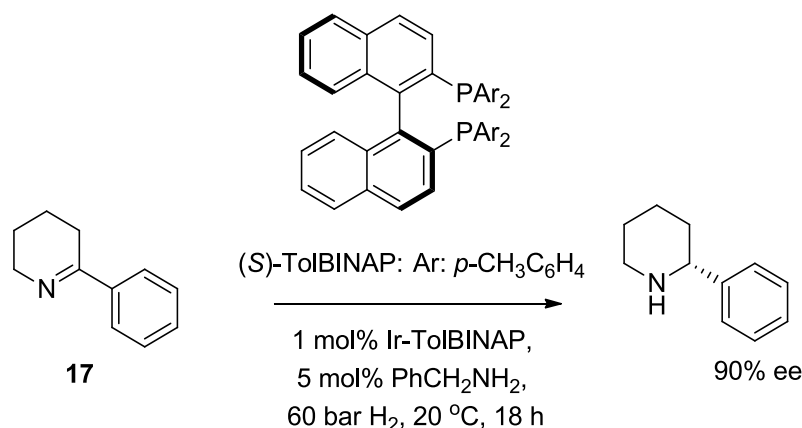


Figure 1.4: Osborn's iridium-diphosphine catalyst.

Since these early examples a range of phosphine ligands have been used to carry out the asymmetric hydrogenation of imines, with increasing yields and ee's.^{25,27}

Tani demonstrated the use of the iridium(I)-TolBINAP catalytic system to hydrogenate imine **17** (Scheme 1.10).³⁷ A good enantioselectivities of 90% ee, was achieved at 1 mol% catalyst, 60 bar H₂ and 20 °C in MeOH. Interestingly, addition of 5 mol% of a protic amine, such as benzylamine, increased both the catalytic activity and the enantioselectivity.



Scheme 1.10: Ir-TolBINAP catalyst for the asymmetric hydrogenation of **17**.

Work by Zhou showed a successful route to cyclic chiral amines using a system of [Ir(COD)Cl]₂/MeO-Biphep/I₂ to reduce quinolines to tetrahydroquinoline. This showed high yields and ee of up to 96% with a wide substrate range.³⁸

1.4 Mechanistic considerations for chiral metal asymmetric hydrogenation of imines

Previous work with catalysts used in the asymmetric hydrogenation of ketones has shown that the Noyori metal ligand bifunctional mechanism (Figure 1.5) is normally observed.^{39,40} This mechanism for ketone

hydrogenation occurs without direct complexation of the substrate to the metal centre and has been shown through nuclear magnetic resonance (NMR) spectra and computational calculations to proceed through a six membered transition state as shown below. The two hydrogens are transferred simultaneously on to one face of the substrate.

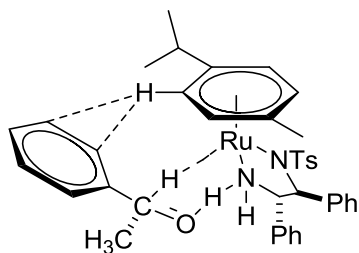


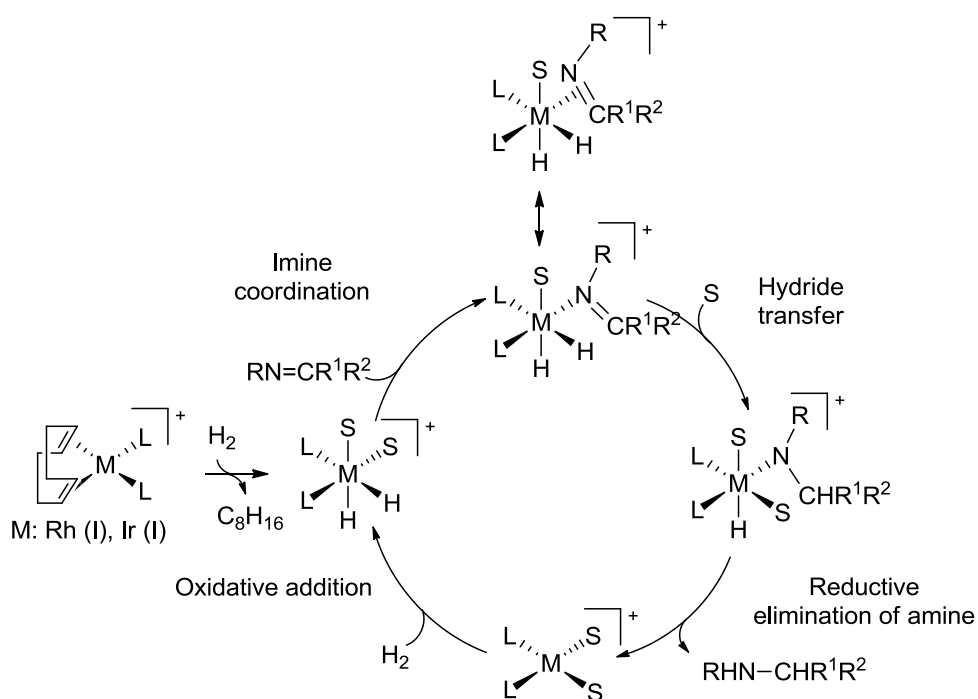
Figure 1.5: Noyori metal ligand bifunctional transition state for ketones.

The calculated structures also show that a π -CH interaction from a cymene C-H to the aromatic ring of the substrate can account for the high selectivity for the re-face (Figure 1.5). While this mechanism prevails for ketones it does not necessarily occur for imines due to the differences outlined earlier.

Casey carried out work using a catalyst similar to that of Shvo,⁴¹ showing that the mechanism of hydrogenation of benzaldehyde occurs simultaneously. The isotope effects suggest that the proton and hydride are transferred simultaneously while also regenerating the catalyst.⁴² Work with imine hydrogenation also suggests a metal ligand bifunctional mechanism but with the electronic nature of the imines influencing the rate determining step. For electron deficient imines the limiting step is the concerted addition while electron rich imines are subject to back hydrogen transfer to ruthenium. The limiting step then becomes the coordination of the amine to Ru where

isomerisation of the imine is possible before hydrogen transfer forms the product.⁴³

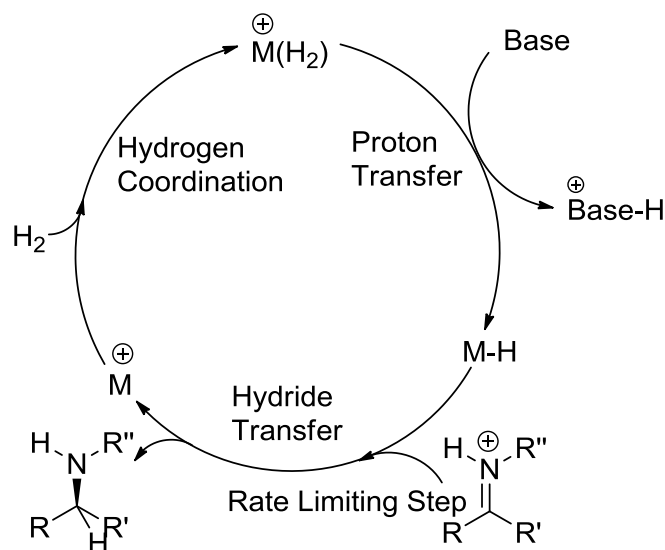
Few studies have been carried out purely on the mechanism of the homogenous hydrogenation of imines. The suggested mechanisms fall into two categories; the classical pathway and the ionic pathway. Scheme 1.11 below shows a representation of the classical pathway, this involves coordination of hydrogen, oxidative addition, and coordination of the substrate prior to hydride transfer, followed by reductive elimination to release the product (Scheme 1.11).



Scheme 1.11: General scheme for imine hydrogenation via a classic pathway; L: ligand; S: solvent.

Work by both James⁴⁴ and Wilkinson⁴⁵ independently studied the case of rhodium-phosphine complexes. It was shown that a hydrogen bonding alcohol solvent was needed to interact with the imine to promote η^2 -C,N-bonding of the substrate. The alcohol solvent is likely to be bound to the metal therefore facilitating imine binding. This classical mechanism is also observed in Buchwald's titanocene catalyst discussed earlier.^{22,23}

Support for the ionic mechanism come from work by Norton. He has shown that a CpRu(II)(P^P) catalyst will catalyse the hydrogenation of iminium ions through an ionic mechanism for half sandwich metal complexes.⁴⁶ Through stoichiometric reactions with the metal hydride and a non-coordinating solvent in the presence of H₂, the mechanism was deduced to involve coordination of H₂ to the Ru cation (Scheme 1.12). This is then followed by heterolytic cleavage to form a proton and a hydride, with the resulting hydride being transferred to the iminium cation in a rate limiting and enantioselective determining step (Scheme 1.12). The mechanism can be described as an outer-sphere mechanism and does not involve imine binding to the metal centre in contrast to the classical mechanism. Moderate enantioselectivities were reported for a methyl aryl pyrrolidinium salt (up to 60% ee).



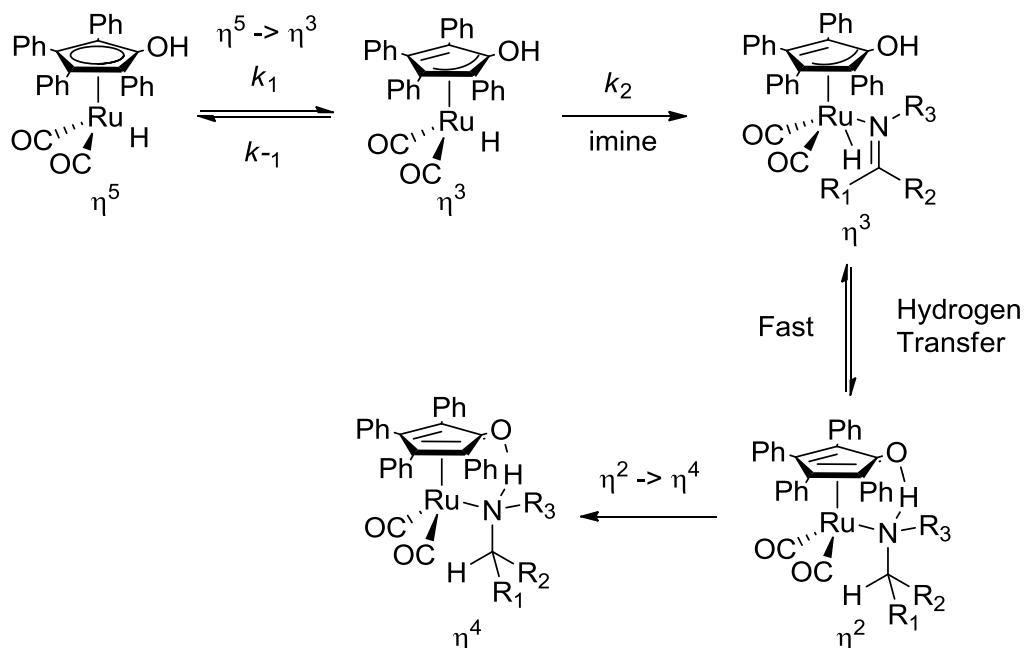
Scheme 1.12: Norton's proposed ionic mechanism.

Norton also monitored the reaction by 1H NMR, observing the formation of monohydride but not dihydrogen or dihydride species, confirming the hydride transfer step as the limiting step. They also determined that the smaller the chelate ring size, the higher the reaction rate is. This means the smaller the ring the more space for the iminium cation to approach the hydride.

Stoichiometric experiments carried out by both Fan³⁵ and Norton⁴⁷ support the ionic mechanism. Fan reported no reduction for a neutral imine even in the presence of an excess of the hydride but upon protonation the reaction occurs to give the product. Norton determined that the hydride transfer rate is first-order for both the Ru-hydride and the iminium cation, being second order overall, supporting the ionic mechanism.

Bäckvall's work on stoichiometric transfer hydrogenation of imines also shows a step wise mechanism that proceeds via protonation of the imine.^{48,49} Through kinetic and isotope studies it was shown that concerted

hydrogen transfer was not the rate determining step, giving support to the stepwise ionic mechanism rather than the concerted alternative. It was proposed that ring slippage from η^5 to η^3 allowed imine co-ordination and was the rate determining step (Scheme 1.13).



Scheme 1.13: Ring slippage mechanism proposed by Bäckvall.

Work by Bullock has shown an ionic mechanism with the H^+/H^- transfer occurring in separate steps for ketones. The system used, looked at a $[\text{W}(\text{Cp})(\text{CO})_2(\text{PMe}_3)(\text{H})_2]^+$ catalyst and a triflate counter ion.⁵⁰ Using stoichiometric reaction with ketones and following the reaction with ^1H NMR, a key $[\text{W}(\text{Cp})(\text{CO})_2(\text{PR}_3)(\text{Et}_2\text{CHOH})]^+$ species was observed demonstrating the protonation of the ketone in a stepwise manner. This was then followed by hydride transfer with the rate limiting step being the release of the product; the catalyst was then regenerated by uptake of H_2 .

Rauchfuss has demonstrated that the 16e $[\text{Cp}^*\text{Ir}(\text{H}_2\text{NCHPhCHPhNTs})]^+$ complex can be converted into a range of organometallic Lewis acids upon reaction with Brønsted acids, displaying a wide range of reactivity.⁵¹⁻⁵³ These generated cationic derivatives are sufficiently electrophilic to activate H_2 directly; conversion to amino hydrides is then possible with the ability to reduce ketones and imines. This demonstrates that the ligands can play a large part in the activation of dihydrogen when assisted by a Brønsted acid.

1.5 Organocatalysis asymmetric imine reduction

An alternative method for producing chiral amines makes use of organocatalysis rather than the metal catalysts so far described. A wide range of organocatalysts have been shown to catalyse the asymmetric transfer hydrogenation of imines.⁵⁴⁻⁵⁶

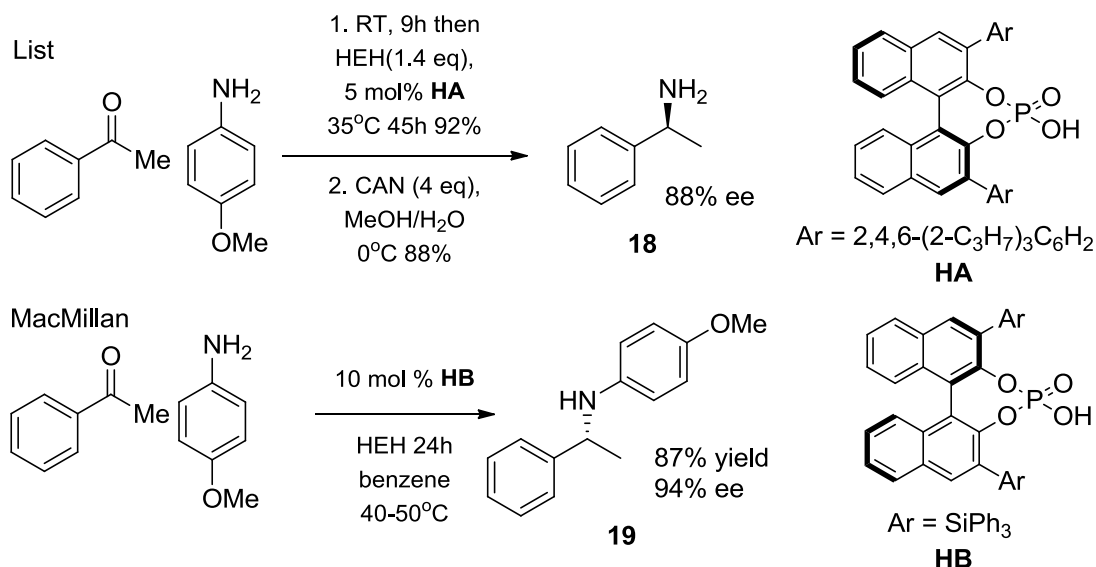
Organocatalysed asymmetric imine reduction makes use of organocatalysts typically with Hantzsch esters (HEH) employed as the hydrogen source. Instead of using metal catalysts, a range of chiral Brønsted acids have been shown to catalyse reactions. Brønsted acids based on chiral thioureas,⁵⁷ diols⁵⁸ and phosphates have been reported. It is however the chiral phosphoric acids which have found the most applications in imine reduction. The groups of List,⁵⁹ Rueping⁶⁰ and MacMillan⁶¹ have all published results on a range of substrates including examples of direct asymmetric reductive amination (DARA).

Rueping's work focused on the reduction of acyclic imines achieving moderate to good yields and ee's of around 70%. The proposed mechanism involves the ion pair formation of a protonated iminium ion with the chiral acid followed by hydride transfer from the Hantzsch ester. The possibility of ion pair formation can be seen in the solvent screening, when polar protic solvents were used no reduction took place. The best results were seen in the non-polar solvents such as toluene and benzene. The non-polar solvents will solvate the ions least and allow for the biggest chance of a successful ion pair formation.

The initial work from List focused on acyclic imines also but achieved higher ee's and yields by using the sterically congested tri-isopropyl aromatic substituted phosphoric acid. The system had a lower loading of the catalyst of 1 mol %, shorter reaction times and a lower temperature of 35°C than previous work. The substrate scope was also extended with the system tolerating both aromatic and aliphatic imines.

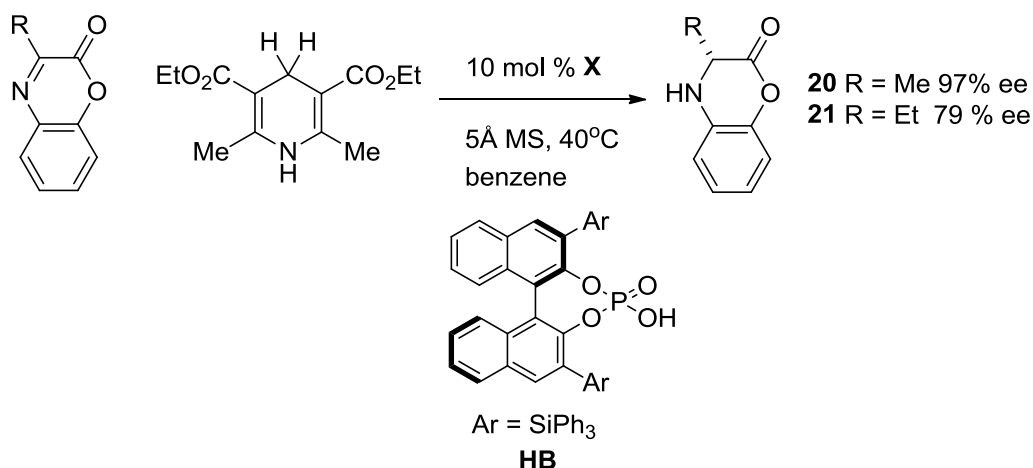
1.5.1 Organocatalysed DARA

List demonstrated that imine generation from a pro-chiral ketone could be done in tandem with the imine reduction thus achieving DARA.⁶² MacMillan also showed a similar concept but using the bulkier triphenylsilyl substituent **HB** with a higher catalyst loading of 10 mol% (Scheme 1.14).⁶¹



Scheme 1.14: Organocatalytic reductive aminations.

The results show a range of substrates tolerating electron withdrawing groups as well as electron donating groups with high ee's of 95%; the system was also applied to an alanine amino ester with 82% yield and 97% ee achieved for **20** (Scheme 1.15). When the corresponding ethyl substituent was used however, the ee was reduced to 79% for **21**, this was rationalised by use of a computational model. It showed that if R= Me the *Si* face was exposed but upon changing to R= Et the extra unit blocks the approach of the hydride so the extra methyl has to be positioned away from the catalyst framework therefore blocking the *si*-face.



Scheme 1.15: Rationale of stereochemical outcome for the MacMillan system.

1.5.2 Mechanistic considerations of organocatalysts

Further to this basic modelling of the mechanism there have been much more extensive studies undertaken by Himo⁶³ and Goodman.⁶⁴ Both propose a three point model to account for the high selectivity observed with the proposed possible modes of interactions shown below (Figure 1.6) making use of hydrogen bonding.

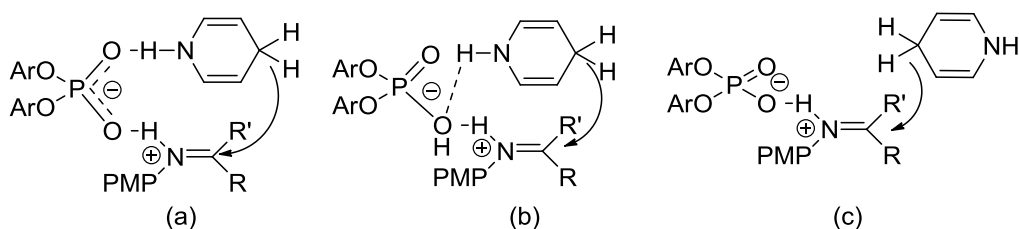


Figure 1.6: Proposed possible interactions of hydride delivery.

The initial protonation of the imine by the acid to form the iminium phosphate ion pair was shown to be fast with a barrier of 1-1.5 kcal mol⁻¹. From this, model (a) is shown to have the lowest barriers of reaction in

comparison to (b) and (c), and the value of just below 20 kcal mol⁻¹ is in agreement with the reported experimental conditions.

The origin of the enantioselectivity is attributed to the steric effects of the bulky aryl groups on the phosphate; the imine shown above is seen by ¹H NMR to be in the *E* conformation but the barrier between *E* and *Z* is calculated to be slightly higher than 2 kcal mol⁻¹. This is low enough so that on the timescale of the reaction they will interconvert and both can therefore feasibly take place in the key hydride transfer step. In the case of this imine the steric repulsion between the aryl rings of the iminium and the mesityl groups of the catalyst are responsible for the selectivity observed. The hydride transfer then takes place on the *Re* face of the *Z* conformation of the iminium ion - this is more compact and fits better in the binding pocket of the phosphate in comparison to the *E* conformation. The *Z* conformation minimises these steric interactions and is therefore the lower energy transition state.

When the reaction is considered with the cyclic 3,4-dihydroquinolinium, the planar nature of the compound and its rigidity lead it to having the transfer occurring on the opposing *Si* face. This minimises the unfavourable interactions with the mesityl groups of the phosphate.

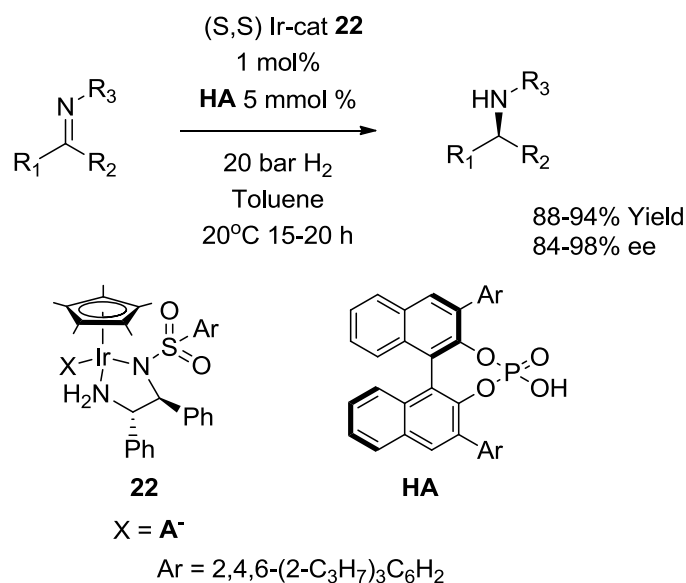
Goodman's work also looked at the same reaction and comes to similar conclusions supporting a three point model of interaction. As in the work by Himo, Figure 1.16(a) is the likeliest pathway and helps explain the enantioselectivity with the two hydrogen bonds and steric interactions. The paper also proposes that in the case of Rueping's work and the majority of MacMillan's, the *Z* isomer of the imine is the likeliest form for the transition

state during the hydride transfer, with the *E* isomer being important as a minor pathway for substrates with different steric constraints e.g. 3,4-dihydroquinolinium.

1.6 Metal–Brønsted acid cooperative catalysis

Previous examples have shown that combining a metal catalyst with a strong acid helps to protonate the catalyst, allowing it to readily activate hydrogen. Brønsted acids meanwhile, have been demonstrated as ideal activators of C=N bonds in asymmetric transfer hydrogenation. From this, the combination of a metal catalyst working with a Brønsted acid has opened up new ways of reducing the imino bond.⁶⁵⁻⁶⁷

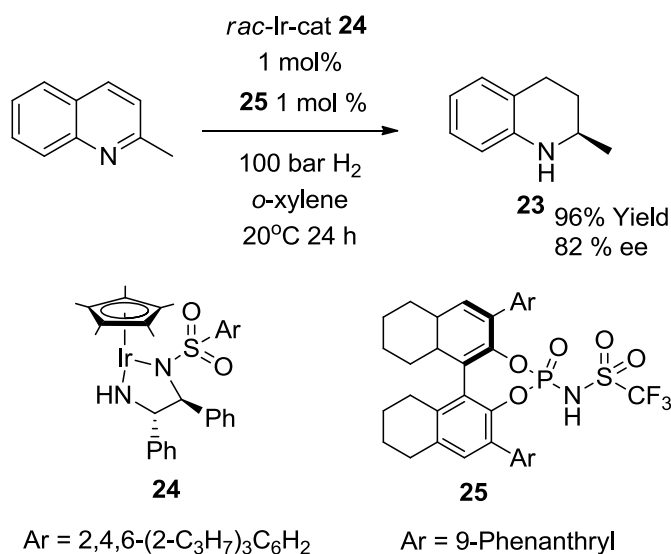
The concept of using chiral Brønsted acids was taken by the group and combined with the rhodium catalytic system that had been used to hydrogenate cyclic imines.⁶⁸ The previous system had not been able to hydrogenate the acyclic imines giving only 3% ee. The metal was changed to iridium, as this had shown the highest activity for the acyclic imines (Scheme 1.16). Once the 16e complex was protonated by the chiral phosphoric acid to form **22**, good yields and high enantioselectivity were observed for a range of aromatic imine substrates. Aliphatic imines were also hydrogenated along with toleration of functionality including olefins and cyclopropyl rings with ee's up to 98%.



Scheme 1.16: Asymmetric hydrogenation of aromatic and aliphatic imines

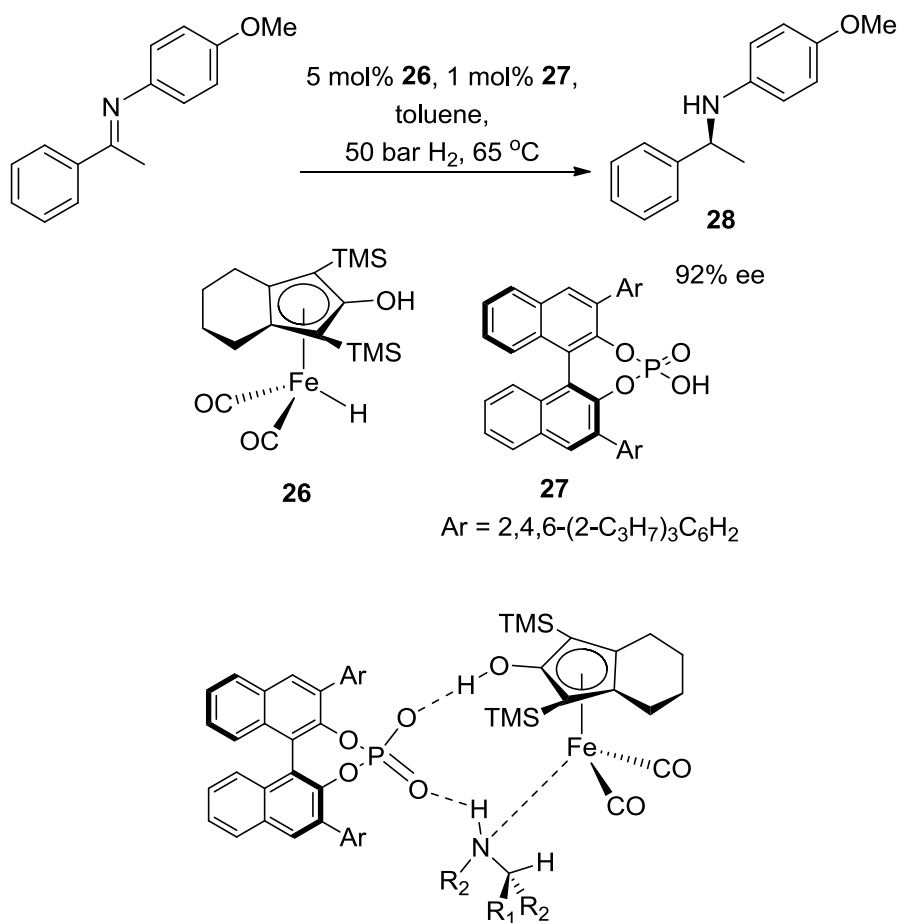
An interesting trend was observed with respect to the size of the aryl groups on the phosphoric acid. When the steric size of the group was increased as well as noting a higher ee, a change in the product configuration from (*R*) to (*S*) was seen. If the diamine ligand had its configuration also switched from (*S,S*) to (*R,R*), the product configuration was again swapped but with much lower yields and ee's than previously seen (98% vs 40% ee).

Rueping took the concept further when he reported the first example of an achiral metal catalyst combined with an (*R*)-*N*-triflylphosphoramidate Brønsted acid. (Scheme 1.17).⁶⁹ The system carries out kinetic discrimination by the Brønsted acid deactivating the (*S,S*)-**24** form of the catalyst, leaving the (*R,R*)-**24** to carry out the enantioselective reaction. The hydrogenation of quinaldine was achieved with 96% yield and 82% ee.



Scheme 1.17: Brønsted acid differentiated metal catalysis by kinetic discrimination.

The Beller group in 2011 reported an iron based cooperative transition-metal and chiral Brønsted acid catalytic system for the asymmetric reduction of imines.⁷⁰ Using iron catalyst **26** and Brønsted acid **27** a range of imines were hydrogenated giving good yields and high selectivities (92% ee in the case of **28**). ³¹P NMR was used to probe the mechanism and the structure shown below involving a three body interaction (Scheme 1.18) was postulated to be the key intermediate in the hydride transfer step.



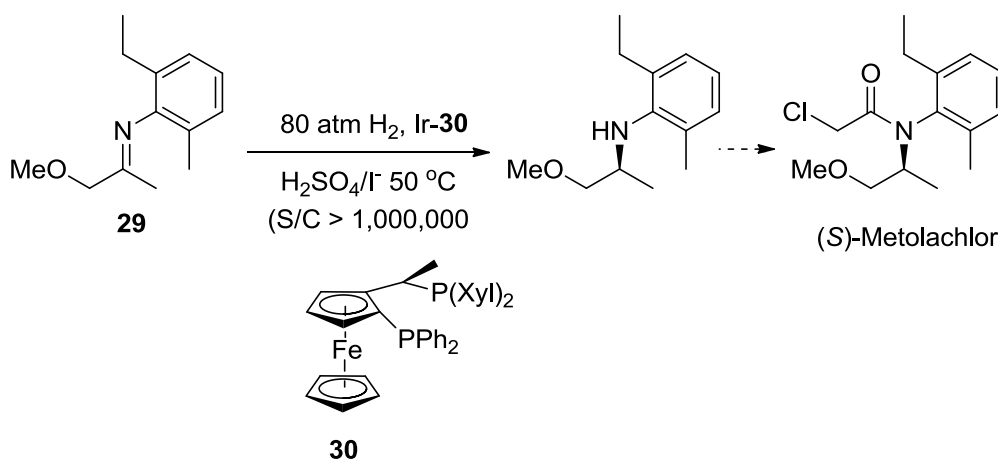
Scheme 1.18: Asymmetric hydrogenation of imines using an iron catalyst and Brønsted acid.

1.6.1 Metal catalysed DARA

One of the most desirable pathways to the production of chiral amines is the DARA of ketones, utilising H₂ gas to perform the key hydrogenation step.¹ This method has major advantages in comparison to other employed routes due its atom efficiency and the ability for it to be carried out in one pot without the need to isolate potentially unstable imine intermediates.

Previous reported work on DARA using metal catalysis has been carried out but with a limited substrate range and with only a few examples involving homogeneous catalysis.²⁴ Blaser reported the first example of DARA

for the synthesis of (*S*)-metolachlor from **29** in 79% ee using an Ir-xyliphos catalyst (Ir-**30**) but this was an isolated example and no substrate scope was examined (Scheme 1.19).⁷¹



Scheme 1.19: First example of DARA for the synthesis of (*S*)-metolachlor.

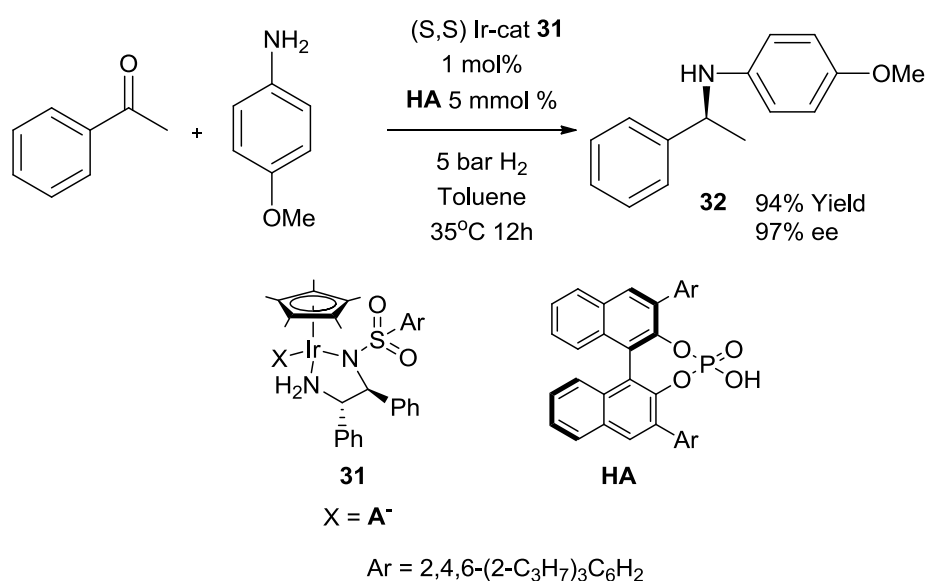
Zhang reported the DARA of aromatic ketones with a system containing an Ir-f-binaphane catalyst with I₂ and Ti(O^{*i*}Pr)₄ but this did not transpose to the aliphatic ketones.⁷²

Asymmetric transfer hydrogenation has also been used to achieve DARA of aromatic ketones and an intra-molecular example, each achieving excellent selectivity but with a limited substrate scope.^{73,74} Work by Rubio-Pérez however has achieved DARA of the aliphatic ketones using a Pd-(*R*)-BINAP catalyst with excellent ee's of 99% but this again is isolated to the aliphatic ketones and does not transfer to the aromatic ketones.⁷⁵

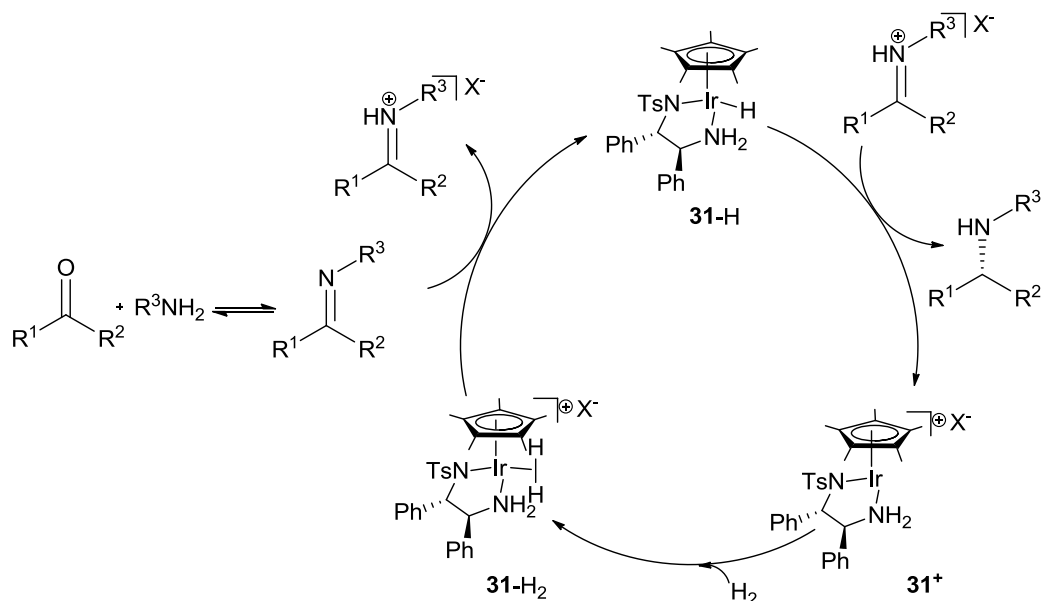
Recently the Beller group reported the achiral reductive amination of aldehydes and ketones with anilines with a simple iron catalyst of triiron

dodecacarbonyl.⁷⁶ Yields of up to 97 % for 28 examples were achieved after 6 h at 65°C under 50 bar of H₂.

Previous work in the Xiao group has led to the development of DARA using a chiral metal Ir(III)-diamine catalyst **31** in combination with a chiral Brønsted acid **HA**.^{77,78} A wide range of aliphatic and aromatic ketones were converted to chiral amines with high yields and ee's reported, giving 97% ee for **32** (Scheme 1.20). The system tolerated electron withdrawing and donating groups as well as olefin functionality. The slight excess of phosphoric acid compared to the catalyst was predicted to help drive the imine formation and then in combination with the metal catalyst, hydrogenate the formed imine.



Scheme 1.20: Catalytic system for DARA developed within the Xiao group.

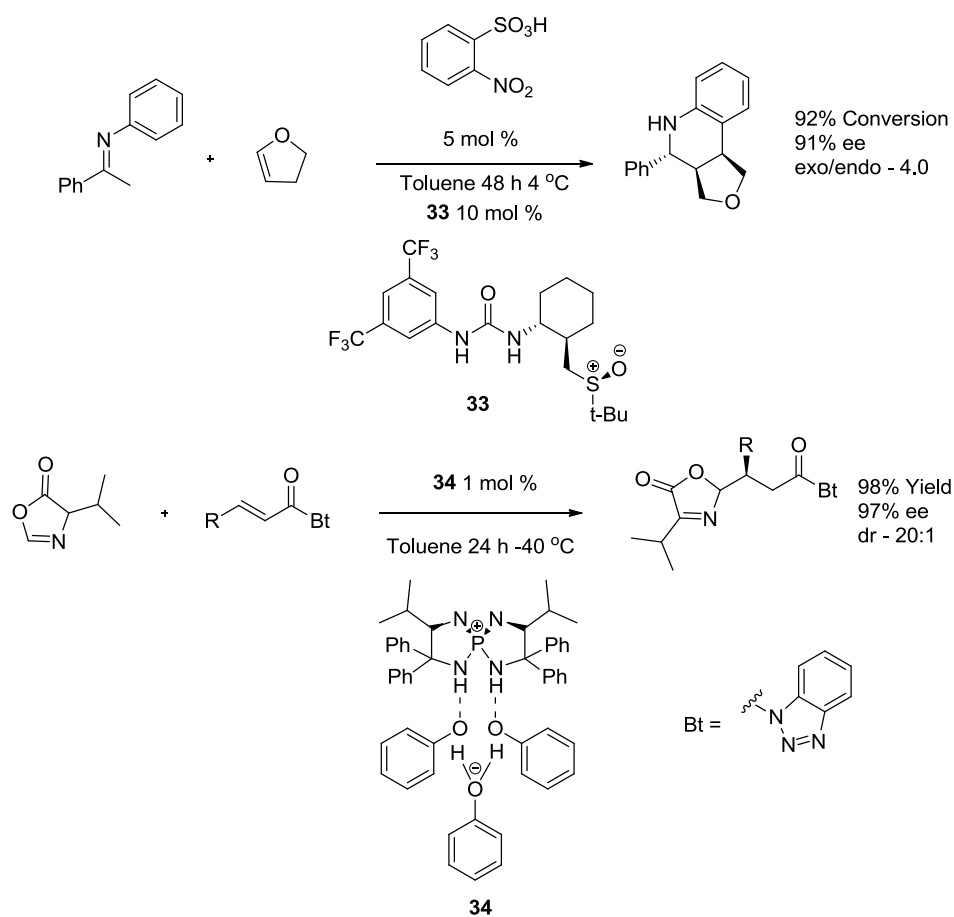


Scheme 1.21: Proposed mechanism for DARA.

Mechanistically the postulated mechanism is shown above (Scheme 1.21). The condensation of the ketone and amine is aided by both **HA** and the removal of water by molecular sieves, thus forming the imine. The H_2 activated by the catalyst **31-H₂**, is heterolytically cleaved forming the iminium cation and the catalyst hydride **31-H**. The iminium phosphate ion pair is then involved in the hydride transfer step, where the chiral amine is formed and the catalyst regenerated. This predicted mechanism is an ionic mechanism rather a concerted bifunctional mechanism and postulates that a three body interaction occurs during the hydride transfer, probably involving hydrogen bonding of **HA** to both **31-H** and the iminium.

1.7 Catalytic supramolecular assemblies

The concept that a three body interaction exists between the two catalysts and the substrate forming a supramolecular assembly is a theory that will be investigated within this thesis. While there are no fully characterised examples in the literature involving a metal catalyst there are examples involving organocatalysts. Publications by both Ooi⁷⁹ and Jacobsen⁸⁰ have shown supramolecular assemblies that form active catalysts (Figure 1.22).



Scheme 1.22: Catalytic Supramolecular Assemblies.

Jacobsen showed that the Povarov reaction could be cocatalyzed by *o*-nitrobenzenesulfonic acid and chiral urea **33**. The assembly above allows for

concerted addition of a dihydrofuran in a highly selective manner giving excellent ee's. The work by Ooi shows a similar principle; a chiral tetraaminophosphonium cation, two phenols, and a phenoxide anion self-assemble into a catalytically active supramolecular structure **34** through hydrogen bonding. The complex promotes a stereoselective conjugate addition of acyl anion equivalents to α,β -unsaturated esters. All the components of the catalytic assembly participate in the selectivity defining step. This kind of supramolecular assembly although identified in organocatalysis has yet to be fully confirmed with the involvement of a metal catalyst.

1.8 Aims of the thesis

The introduction has described the methodology developed for the asymmetric hydrogenation of imines with particular focus on metal catalysed, organocatalysed and the subsequent advance to cooperative catalysis. The improvements described have seen higher yields and ee's for a range of imine substrates under milder conditions. The mechanistic considerations for each of these types of catalysis have also been described. These have shown evidence for metal catalysts operating via either a concerted or ionic mechanism. Organocatalysts however, can play a dual role in the protonation of the imine, followed by facilitating the hydride delivery by use of hydrogen bonding to both the hydride donor and iminium ion.

While the mechanisms for both the metal catalysed and organocatalysed enantioselective hydrogenations have been elucidated individually, the mechanism of how these high selectivities are achieved in the

case of cooperative catalysis remains unclear. Questions remain over the exact role of the organocatalyst, how the chirality is transferred from the metal catalyst and organocatalyst to the substrate and whether this proceeds with the catalysts working cooperatively. The nature of the interactions present during the catalysis needs examining to see if the previously postulated supramolecular structure, between all three compounds exists.

In Chapter 2 the development of a cooperative system for the enantioselective hydrogenation of imines using an achiral metal catalyst and Brønsted acid is described. The mechanism is then studied for this system with each of the key steps examined in turn. By the use of stoichiometric reactions, isolation of intermediates and *in-situ* NMR the full mechanism is determined.

Chapter 3 is a natural extension of the previous chapter and looks at the key hydride transfer step where the chirality is transferred. The nature of the interactions present in this step are determined by a combinations of NMR and computational calculations. Crucially this allows for the key active catalytic species to be identified.

The work in Chapter 4 looks at how the levels of conjugation present in a range of cyclometallated iridium catalysts effects the levels of activity for a range of hydrogen transfer reactions. A full computational study is carried out on a selected series of the cyclometallated iridium catalysts and the key structural and electronic factors affecting reactivity revealed.

1.9 References

- (1) Breuer, M.; Ditrich, K.; Habicher, T.; Hauer, B.; Kessler, M.; Stürmer, R.; Zelinski, T. *Angew. Chem., Int. Ed.* **2004**, *43*, 788.
- (2) Spindler, F.; Blaser, H.-U. In *The Handbook of Homogeneous Hydrogenation*; Wiley-VCH Verlag GmbH: 2008, p 1193.
- (3) Culy, C. R.; Jarvis, B. *Drugs* **2001**, *61*, 1625.
- (4) Polinsky, R. J. *Clinical Therapeutics* **1998**, *20*, 634.
- (5) Ye, Z. Q.; Lan, R. Z.; Yang, W. M.; Yao, L. F.; Yu, X. *Journal of International Medical Research* **2008**, *36*, 244.
- (6) Xu, L.-W.; Luo, J.; Lu, Y. *Chem. Commun.* **2009**, 1807.
- (7) Marigo, M.; Melchiorre, P. *Chemcatchem* **2010**, *2*, 621.
- (8) Sakthivel, K.; Notz, W.; Bui, T.; Barbas, C. F. *J. Am. Chem. Soc.* **2001**, *123*, 5260.
- (9) Fache, F.; Schulz, E.; Tommasino, M. L.; Lemaire, M. *Chem. Rev.* **2000**, *100*, 2159.
- (10) He, Y.-M.; Fan, Q.-H. *Org. Biomol. Chem.* **2010**, *8*, 2497.
- (11) Ikariya, T.; Murata, K.; Noyori, R. *Org. Biomol. Chem.* **2006**, *4*, 393.
- (12) Constable, D. J. C.; Dunn, P. J.; Hayler, J. D.; Humphrey, G. R.; Leazer, J. L., Jr.; Linderman, R. J.; Lorenz, K.; Manley, J.; Pearlman, B. A.; Wells, A.; Zaks, A.; Zhang, T. Y. *Green Chem.* **2007**, *9*, 411.
- (13) Murakami, Y.; Kikuchi, J.; Hisaeda, Y.; Hayashida, O. *Chem. Rev.* **1996**, *96*, 721.

- (14) Savile, C. K.; Janey, J. M.; Mundorff, E. C.; Moore, J. C.; Tam, S.; Jarvis, W. R.; Colbeck, J. C.; Krebber, A.; Fleitz, F. J.; Brands, J.; Devine, P. N.; Huisman, G. W.; Hughes, G. J. *Science* **2010**, 329, 305.
- (15) Kim, Y.; Park, J.; Kim, M. J. *Chemcatchem* **2011**, 3, 271.
- (16) Vaz, B. G.; Milagre, C. D. F.; Eberlin, M. N.; Milagre, H. M. S. *Org. Biomol. Chem.* **2013**, 11, 6695.
- (17) Arai, S.; Bellemin-Laponnaz, S.; Fu, G. C. *Angewandte Chemie-International Edition* **2001**, 40, 234.
- (18) Noyori, R.; Ohkuma, T. *Angew. Chem., Int. Ed.* **2001**, 40, 40.
- (19) Blaser, H. U.; Malan, C.; Pugin, B.; Spindler, F.; Steiner, H.; Studer, M. *Adv. Synth. Catal.* **2003**, 345, 103.
- (20) James, B. R. *Catal. Today* **1997**, 37, 209.
- (21) Levi, A.; Modena, G.; Scorrano, G. *J. Chem. Soc., Chem. Commun.* **1975**, 6.
- (22) Willoughby, C. A.; Buchwald, S. L. *J. Org. Chem.* **1993**, 58, 7627.
- (23) Willoughby, C. A.; Buchwald, S. L. *J. Am. Chem. Soc.* **1994**, 116, 11703.
- (24) Nugent, T. C.; El-Shazly, M. *Adv. Synth. Catal.* **2010**, 352, 753.
- (25) Xie, J. H.; Zhu, S. F.; Zhou, Q. L. *Chem. Rev.* **2011**, 111, 1713.
- (26) Wang, C.; Villa-Marcos, B.; Xiao, J. *Chem. Commun.* **2011**, 47, 9773.
- (27) Fleury-Bregeot, N.; de la Fuente, V.; Castillon, S.; Claver, C. *Chemcatchem* **2010**, 2, 1346.
- (28) Bakos, J.; Orosz, A.; Heil, B.; Laghmari, M.; Lhoste, P.; Sinou, D. *J. Chem. Soc., Chem. Commun.* **1991**, 1684.

- (29) Shang, G.; Yang, Q.; Zhang, X. *Angew. Chem. Int. Ed.* **2006**, *45*, 6360.
- (30) Zhong, Y.-L.; Krska, S. W.; Zhou, H.; Reamer, R. A.; Lee, J.; Sun, Y.; Askin, D. *Org. Lett.* **2008**, *11*, 369.
- (31) Li, C.; Xiao, J. *J. Am. Chem. Soc.* **2008**, *130*, 13208.
- (32) Ohkuma, T.; Utsumi, N.; Tsutsumi, K.; Murata, K.; Sandoval, C.; Noyori, R. *J. Am. Chem. Soc.* **2006**, *128*, 8724.
- (33) Abdur-Rashid, K.; Lough, A. J.; Morris, R. H. *Organometallics* **2001**, *20*, 1047.
- (34) Cobley, C. J.; Henschke, J. P. *Adv. Synth. Catal.* **2003**, *345*, 195.
- (35) Zhou, H.; Li, Z.; Wang, Z.; Wang, T.; Xu, L.; He, Y.; Fan, Q.-H.; Pan, J.; Gu, L.; Chan, A. S. C. *Angew. Chem., Int. Ed.* **2008**, *47*, 8464.
- (36) Spindler, F.; Pugin, B.; Blaser, H. U. *Angew. Chem., Int. Ed.* **1990**, *29*, 558.
- (37) Tani, K.; Onouchi, J.; Yamagata, T.; Kataoka, Y. *Chem. Lett.* **1995**, 955.
- (38) Wang, W. B.; Lu, S. M.; Yang, P. Y.; Han, X. W.; Zhou, Y. G. *J. Am. Chem. Soc.* **2003**, *125*, 10536.
- (39) Noyori, R.; Yamakawa, M.; Hashiguchi, S. *J. Org. Chem.* **2001**, *66*, 7931.
- (40) Sandoval, C. A.; Ohkuma, T.; Utsumi, N.; Tsutsumi, K.; Murata, K.; Noyori, R. *Chem. Asian. J.* **2006**, *1*, 102.
- (41) Shvo, Y.; Czarkie, D.; Rahamim, Y.; Chodosh, D. F. *J. Am. Chem. Soc.* **1986**, *108*, 7400.

- (42) Casey, C. P.; Singer, S. W.; Powell, D. R.; Hayashi, R. K.; Kavana, M. *J. Am. Chem. Soc.* **2001**, *123*, 1090.
- (43) Casey, C. P.; Johnson, J. B. *J. Am. Chem. Soc.* **2005**, *127*, 1883.
- (44) Becalski, A. G.; Cullen, W. R.; Fryzuk, M. D.; James, B. R.; Kang, G. J.; Rettig, S. J. *Inorg. Chem.* **1991**, *30*, 5002.
- (45) Longley, C. J.; Goodwin, T. J.; Wilkinson, G. *Polyhedron* **1986**, *5*, 1625.
- (46) Guan, H.; Iimura, M.; Magee, M. P.; Norton, J. R.; Zhu, G. *J. Am. Chem. Soc.* **2005**, *127*, 7805.
- (47) Magee, M. P.; Norton, J. R. *J. Am. Chem. Soc.* **2001**, *123*, 1778.
- (48) Samec, J. S. M.; Backvall, J. E. *Chem. Eur. J.* **2002**, *8*, 2955.
- (49) Samec, J. S. M.; Ell, A. H.; Backvall, J. E. *Chem. Commun.* **2004**, 2748.
- (50) Bullock, R. M. *Chem. Eur. J.* **2004**, *10*, 2366.
- (51) Heiden, Z. M.; Rauchfuss, T. B. *J. Am. Chem. Soc.* **2009**, *131*, 3593.
- (52) Letko, C. S.; Heiden, Z. M.; Rauchfuss, T. B. *Eur. J. Inorg. Chem.* **2009**, *2009*, 4927.
- (53) Heiden, Z. M.; Gorecki, B. J.; Rauchfuss, T. B. *Organometallics* **2008**, *27*, 1542.
- (54) Adolfsson, H. In *Modern Reduction Methods*; Wiley-VCH Verlag GmbH & Co. KGaA: 2008, p 339.
- (55) Kampen, D.; Reisinger, C.; List, B. In *Asymmetric Organocatalysis*; List, B., Ed.; Springer Berlin Heidelberg: 2009; Vol. 291, p 1.
- (56) de Vries, J. G.; Mrcic, N. *Catal. Sci. Tech.* **2011**, *1*, 727.

- (57) Akiyama, T. *Chem. Rev.* **2007**, *107*, 5744.
- (58) Huang, Y.; Unni, A. K.; Thadani, A. N.; Rawal, V. H. *Nature* **2003**, *424*, 146.
- (59) Hoffmann, S.; Seayad, A. M.; List, B. *Angew. Chem. Int. Ed.* **2005**, *44*, 7424.
- (60) Rueping, M.; Sugiono, E.; Azap, C.; Theissmann, T.; Bolte, M. *Org. Lett.* **2005**, *7*, 3781.
- (61) Storer, R. I.; Carrera, D. E.; Ni, Y.; MacMillan, D. W. *J. Am. Chem. Soc.* **2006**, *128*, 84.
- (62) Wakchaure, V. N.; Zhou, J.; Hoffmann, S.; List, B. *Angew. Chem. Int. Ed.* **2010**, *49*, 4612.
- (63) Marcelli, T.; Hammar, P.; Himo, F. *Chem. Eur. J.* **2008**, *14*, 8562.
- (64) Simon, L.; Goodman, J. M. *J. Am. Chem. Soc.* **2008**, *130*, 8741.
- (65) Yu, Z.; Jin, W.; Jiang, Q. *Angew. Chem. Int. Ed.* **2012**, *51*, 6060.
- (66) Shao, Z.; Zhang, H. *Chem. Soc. Rev.* **2009**, *38*, 2745.
- (67) Du, Z.; Shao, Z. *Chem. Soc. Rev.* **2013**, *42*, 1337.
- (68) Li, C.; Wang, C.; Villa-Marcos, B.; Xiao, J. *J. Am. Chem. Soc.* **2008**, *130*, 14450.
- (69) Rueping, M.; Koenigs, R. M. *Chem. Commun.* **2011**, *47*, 304.
- (70) Zhou, S. L.; Fleischer, S.; Junge, K.; Beller, M. *Angew. Chem. Int. Ed.* **2011**, *50*, 5120.
- (71) Blaser, H. U.; Buser, H. P.; Jalett, H. P.; Pugin, B.; Spindler, F. *Synlett* **1999**, 867.
- (72) Chi, Y. X.; Zhou, Y. G.; Zhang, X. M. *J. Org. Chem.* **2003**, *68*, 4120.

- (73) Kadyrov, R.; Riermeier, T. H. *Angew. Chem. Int. Ed.* **2003**, *42*, 5472.
- (74) Williams, G. D.; Pike, R. A.; Wade, C. E.; Wills, M. *Org. Lett.* **2003**, *5*, 4227.
- (75) Rubio-Perez, L.; Perez-Flores, F. J.; Sharma, P.; Velasco, L.; Cabrera, A. *Org. Lett.* **2009**, *11*, 265.
- (76) Fleischer, S.; Zhou, S.; Junge, K.; Beller, M. *Chem. Asian J.* **2011**, *6*, 2240.
- (77) Li, C.; Villa-Marcos, B.; Xiao, J. *J. Am. Chem. Soc.* **2009**, *131*, 6967.
- (78) Villa-Marcos, B.; Li, C.; Mulholland, K. R.; Hogan, P. J.; Xiao, J. *Molecules* **2010**, *15*, 2453.
- (79) Uraguchi, D.; Ueki, Y.; Ooi, T. *Science* **2009**, *326*, 120.
- (80) Xu, H.; Zuend, S. J.; Woll, M. G.; Tao, Y.; Jacobsen, E. N. *Science* **2010**, *327*, 986.

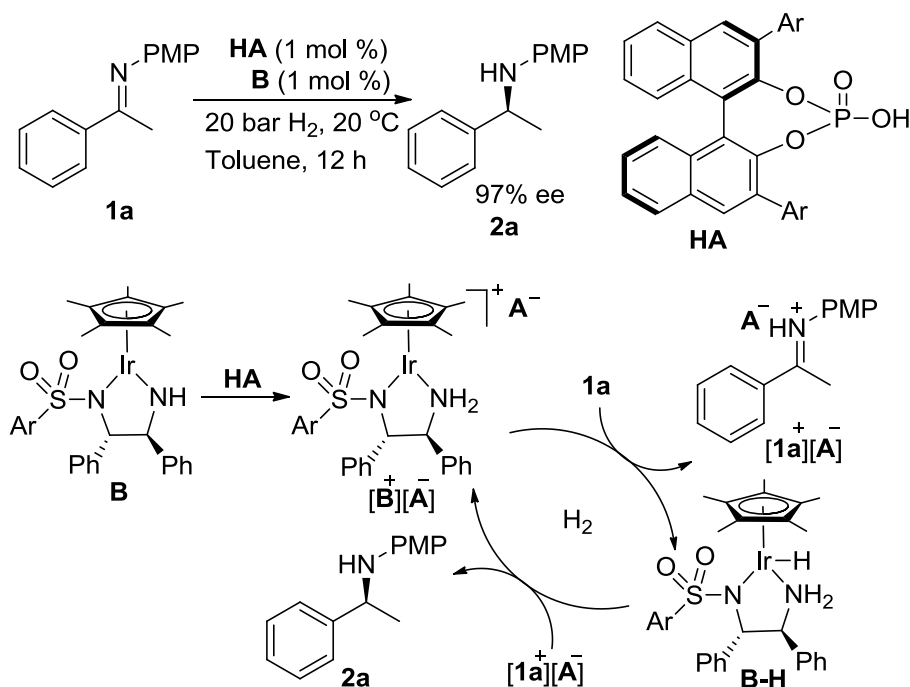
Chapter 2

Cooperative Catalysis: Mechanistic Studies of an Achiral Metal Catalyst Coupled with Chiral Brønsted Acid for Asymmetric Hydrogenation of Imines

2.1 Introduction

Over the past few decades, a great deal of effort has been made on asymmetric reduction of imines to access optically active amines,^{1-3,4-13,14-19,20-22,23} ubiquitous functionalities in fine chemical, agrochemical and pharmaceutical products.^{24,25} Among the approaches reported so far, asymmetric hydrogenation with cheap, clean hydrogen gas offers a totally atom-economic and most convenient route. However, in contrast to the great success in asymmetric hydrogenation of prochiral olefins and ketones,²⁶ highly enantioselective hydrogenation of imines is still challenging. In particular, apart from only a few isolated examples,^{27,28-30} few catalysts are known that can deliver enantioselectivity higher than 80% ee in the hydrogenation of imines derived from aliphatic ketones.^{4,6,9,10} This chapter describes that by exploiting *achiral-chiral* metal-organo cooperative catalysis, acyclic imines, including *aliphatic ones*, can be readily hydrogenated with enantioselectivities up to 98% ee. Leading on from this, the mechanism is fully investigated to elucidate the key intermediates and explain how high selectivities are achieved.

The combination of metal catalysts with organocatalysts has recently become one of the most active and exciting topics in catalysis, which allows reactivity and selectivity patterns inaccessible within the field of either homogeneous or organo-catalysis alone.³¹⁻³⁷ Previous work within the group showed that the *chiral* Cp*Ir(diamine) complex **[B⁺][A⁻]**, generated from the protonation of the *chiral* complex **B** with the *chiral* phosphoric acid **HA**, activates H₂ and catalyses asymmetric hydrogenation of acyclic imines²⁸ and reductive amination of ketones^{29,30} with excellent enantioselectivities (Scheme 2.1).



Scheme 2.1: Hydrogenation of imine with a cooperative catalytic system resulting from **B** + **HA** (Ar = 2,4,6-triisopropylphenyl).

The reduction was thought to proceed *via* an ionic pathway involving metal-organo cooperative catalysis,^{38,39} in which the phosphate anion ion-pairs with the iminium cation,⁴⁰ thereby influencing the face-selective addition of the

hydride **B-H** to the imino C=N bond and so the enantioselectivity. In line with this hypothesis, dramatic changes in enantioselectivity and reversal of amine configuration were observed on altering the steric bulkiness of (*R*)-**HA**, or on replacing the (*S,S*)-diamine with a (*R,R*)-diamine ligand in **B**.²⁸ These results suggested to us that it might be possible to combine a *chiral* **HA** with an *achiral* analogue of **B** to effect the same asymmetric hydrogenation, with the former inducing chirality at the latter.^{41,42}

This was not very far-fetched, since chiral phosphoric acids had been demonstrated to be able to direct highly enantioselective hydride transfer from achiral organo-hydride donors to imines.⁴³⁻⁴⁶ In fact, while our search for the optimal chiral-achiral “couple” was in progress, Rueping and co-workers reported in 2011 that chiral *N*-triflylphosphoramidate can induce chirality at an achiral analogue of **B**, although the enantioselectivity was low (32% ee) in the hydrogenation of quinoline.⁴⁷ More recently, Beller and co-workers developed a highly effective catalytic system which combines an achiral iron complex with a chiral phosphoric acid,⁶ affording excellent ee’s (up to 97%) for aryl ketone-derived imines, but lower values (up to 83%) for the analogous aliphatic imines.

The use of a chiral organocatalyst to induce chirality at an achiral metal complex, or *vice versa*, is interesting, not only because of “economy” in chirality but also due to widened catalyst space, opening up the potential for a range of noncovalent interactions to be exploited. Described below are our results on asymmetric hydrogenation of acyclic imines obtained using an easily accessible *achiral* Cp*Ir(diamine) catalyst coupled with a *chiral* phosphoric

acid and the determination of the mechanism with which the high selectivities are achieved.

2.2 Results and discussion

2.2.1 Identification of catalysts

The initial catalyst screening and substrate scope of the hydrogenation was carried out by Dr Weijun Tang followed by joint work on the mechanism.⁴⁸ Following on from the initial search for a viable chiral-achiral couple of catalysts, a series of neutral 16e complexes exemplified by **C**₁-**C**₆ from cheaply available ethylene diamine and its derivatives (Figure 2.1).^{49,50} Mixing the phosphoric acid **HA** with **C** leads to its protonation at the amido nitrogen, forming an analogue of **B**⁺, i.e. the active catalyst [**C**⁺][**A**⁻] (Scheme 2.2).^{28-30,}

41,51-53

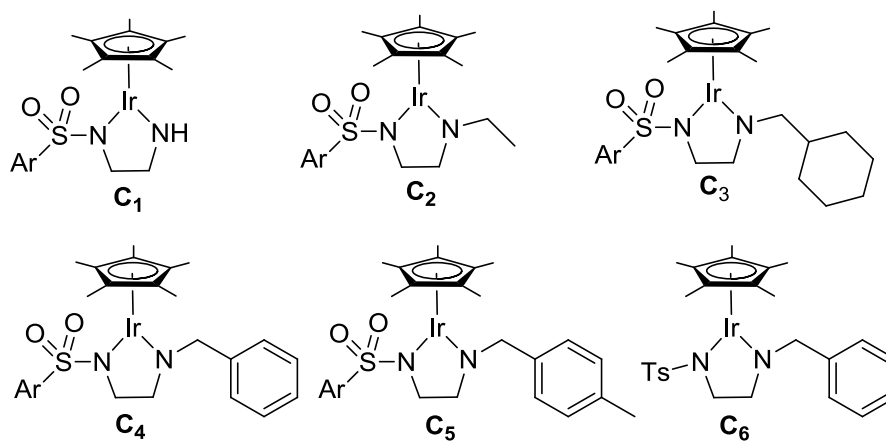
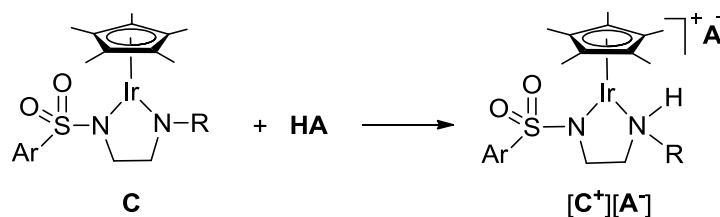


Figure 2.1: Achiral metal catalysts synthesized and studied for cooperative hydrogenation (Ar = 2,4,6-triisopropylphenyl).



Scheme 2.2: Protonation at the amido nitrogen, forming the active catalyst **[C⁺][A⁻]**.

With these complexes in hand, the asymmetric hydrogenation of a model imine **1a** was examined under the same conditions as reported before, i.e. 20 bar H₂ in a non-polar solvent toluene at room temperature (RT), with the catalyst **[C⁺][A⁻]** formed *in situ* by combining **C** with **HA**.²⁸ The results are shown in Table 1. Compared with those obtained with the chiral combination **[B⁺][A⁻]** (Scheme 2.1), the conversion and enantioselectivity were both decreased considerably when using the achiral **C₁** in the presence of **HA** (Table 2.1, entry 1). Replacing the hydrogen atom with an ethyl group on the nitrogen in **C₁** did not lead to a better catalyst (**C₂**) (Table 2.1, entry 2). And somewhat surprisingly, when a cyclohexylmethyl group was installed (**C₃**), little hydrogenation was observed (Table 2.1, entry 3), highlighting the critical effect of the diamine structure on the catalysis. Further search led to the discovery of **C₄**, in which the NH hydrogen is replaced with a benzyl group, and when **C₄** was combined with **HA**, an excellent enantioselectivity of 97% ee was observed along with complete conversion of **1a** (Table 2.1, entry 4).

Table 2.1: Screening of achiral metal catalysts for the asymmetric hydrogenation of imine **1a**^a

Entry	C	HA (%)	T (h)	Conv. (%) ^b	Ee (%) ^c
1	C ₁	2	5	10	50
2	C ₂	2	5	15	48
3	C ₃	2	5	2	-
4	C ₄	2	5	100	97
5	C ₅	2	5	100	94
6	C ₆	2	5	100	95
7	C ₄	1	5	82	97
8	C ₄	1	12	100	97
9 ^d	C ₄	1	12	87	98
10 ^e	C ₄	1	12	43	97

^aThe reaction was carried out with 0.15 mmol **1a** in 0.7 mL toluene. ^bThe conversion was determined by ¹H NMR. ^cDetermined by HPLC analysis; configuration was assigned by comparison with the literature. ^dThe temperature was 10 °C. ^e5 bar H₂.

Aiming to further improve the enantioselectivity, alteration to **C**₄ was undertaken and the resulting complexes were tested. Whilst neither **C**₅ nor **C**₆ gave better results when combined with **HA**, some interesting observations emerged. The bulky Ar group in **C**₄ is beneficial, as replacing the Ar with *p*-tolyl (**C**₆) led to a slight decrease in the ee (entry 4 vs 6) and a similar effect was observed for **C**₅ (entry 4 vs 5).

With **C**₄, the loading of the phosphoric acid **HA** can be reduced without compromising the ee; but the hydrogenation became slower (Table 2.1, entry

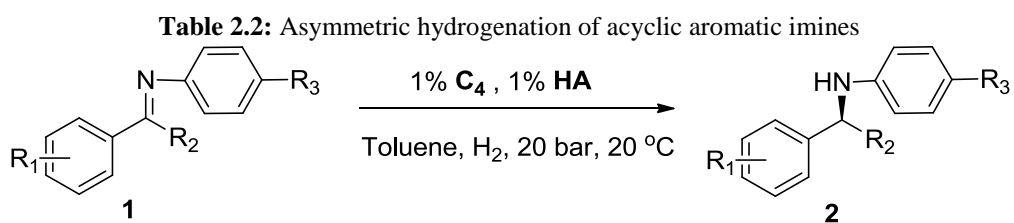
7). Full conversion was reached in a longer reaction time of 12 h (Table 2.1, entry 8). As maybe expected, lower temperature improved the enantioselectivity slightly but reduced the reaction rate (Table 2.1, entry 9). Additionally, hydrogen pressure also impacts on the hydrogenation rate, with lower pressure leading to a lower conversion (Table 2.1, entry 10).

2.2.2 Asymmetric hydrogenation of acyclic aromatic imines

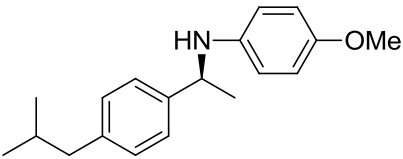
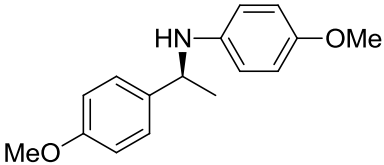
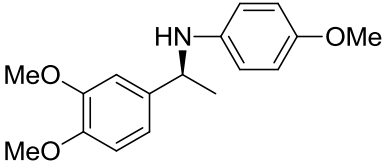
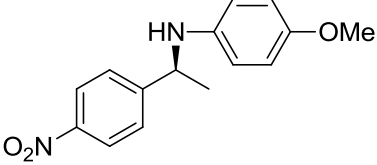
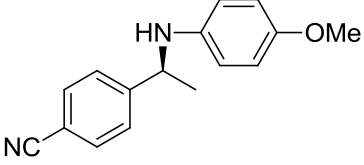
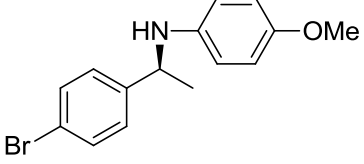
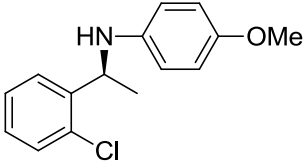
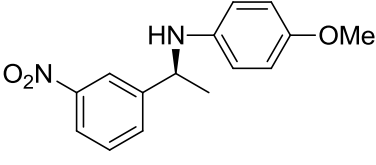
Having established a highly enantioselective achiral-chiral combination of catalysts for the hydrogenation of imine **1a**, we turned our attention to examining the scope of the **C₄-HA** couple-catalysed asymmetric hydrogenation of substituted acyclic aromatic imines **1b-p**. The results are shown in Table 2.2. In general, all substrates examined were reduced smoothly in excellent enantioselectivities and isolated yields, with ee's ranging from 92% to 98%. Notably, this catalytic system tolerates not only functional groups with diverse electronic properties, e.g. -MeO, -CN, -Br and -NO₂, but also at different substitution positions (Table 2.2, entries 2-4). Imine substrates bearing *ortho*-substituents on the phenyl ring necessitated more forcing conditions for the reaction to proceed with a reasonable rate; however, the enantioselectivity remained high (Table 2.2, entries 4 and 11). The low reactivity of these imines is likely to stem from the *ortho*-substituents, which increase the steric bulkiness of the imine, impeding its approach to the Ir-H hydride. Replacing the anisidine in **1** with other aryl groups, such as aniline or *p*-bromoaniline, does not appear to impact on the hydrogenation, with excellent enantioselectivities and high isolated yields again observed (Table 2.2, entries 14-15). Finally, α -substituted

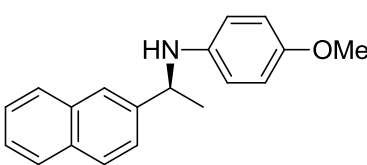
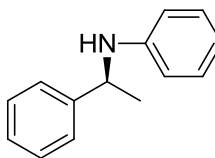
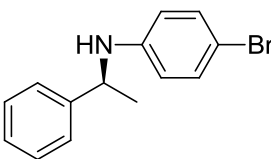
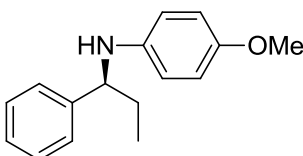
N-aryl ketimine could also be reduced with high enantioselectivity (Table 2.2, entry 16).

For most of the reactions in Table 2.2, the enantioselectivities obtained with the achiral-chiral couple **C**₄-**HA** are comparable to those from the chiral-chiral **B**-**HA**.²⁸ However, **C**₄-**HA** led to significantly higher ee's in the case of the –CN and –NO₂ substituted imines **1h**, **1i** and **1l**, e.g. 92% ee with **C**₄-**HA** (Table 2.2, entry 12) vs 84% ee with **B**-**HA** for **1l**.²⁸ Why this is the case is not immediately clear to us.



Entry	Product	Yield (%)	Ee (%) ^b
1		95	97
2		94	97
3		95	98
4 ^{d,e}		93	97

5		93	98
6		97	97
7		92	98
8		95	96
9		93	96
10		92	98
11 ^{d,e}		93	94
12		93	92

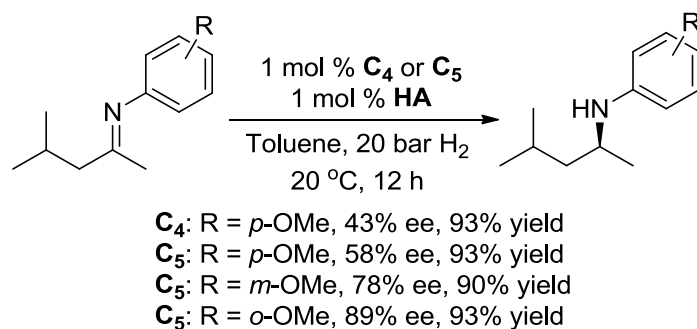
13		95	98
14		96	98
15		96	97
16		93	92

^aAll reactions were carried out with 0.15 mmol substrate, 0.7 mL toluene, 20 bar H₂, 20 °C for 12 h. ^bIsolated yields. ^cThe enantioselectivities were determined by HPLC; *S* configuration, assigned by comparison with the literature (See the SI). ^dThe reactions were carried out in 20 h with 2% of the phosphoric acid **HA**. ^eThe pressure was 30 bar.

2.2.3 Asymmetric hydrogenation of aliphatic ketone-derived imines

In contrast to aromatic imines, successful examples of asymmetric hydrogenation of imines derived from aliphatic ketones are rare.^{4,6,9,10} Subsequent to the study above, we explored the same catalytic system for asymmetric hydrogenation of the more challenging aliphatic *N*-aryl imines. We started our initial investigation using 4-methoxy-*N*-(4-methylpentan-2-ylidene)-aniline as a model substrate (Scheme 2.3, R = *p*-OMe), which afforded a high enantioselectivity of 92% ee under the catalysis by a chiral-chiral couple analogous to **B-HA**.^{9a} However, combining the achiral **C₄** with

HA resulted in a much lower enantioselectivity of 43% ee. A moderate increases in ee was observed when **C₄** was replaced with **C₅**. Since increasing the steric hindrance of imines may render their C=N faces easier to discriminate,^{4,10} we went on to study imines with different substitution pattern. As can be seen from Scheme 2.3, the enantioselectivity increased progressively when the imine became sterically more demanding, i.e. when the substitution position at the *N*-aryl ring changes from *p*, *m* to *o*, reaching a remarkable value of 89% ee. This observation may not be surprising, considering that the interaction between the phosphate **A⁻** and the iminium cation is non-covalent and weak⁴⁰; therefore the enantioselectivity is expected to be sensitive to the steric hindrance of the imine (see Chapter 3).



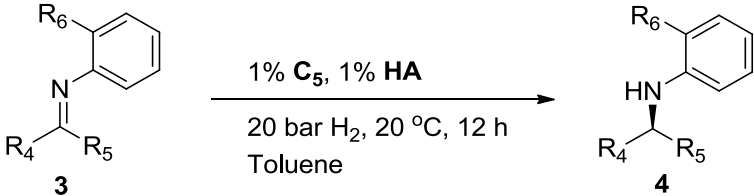
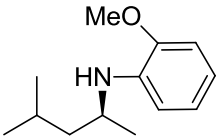
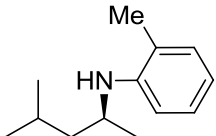
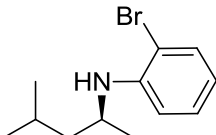
Scheme 2.3: Substrate steric effect on enantioselectivity.

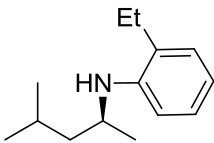
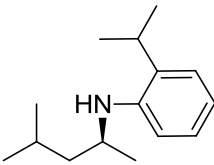
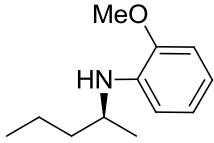
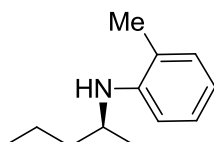
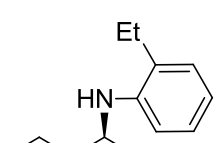
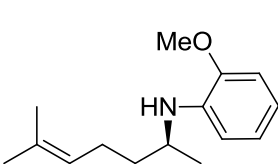
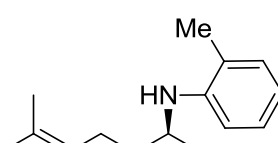
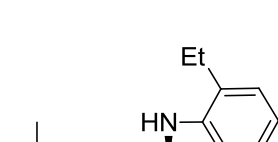
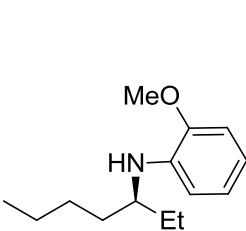
To probe the generality of the **C₅**-**HA** combination for aliphatic ketone-derived imines, a series of *ortho*-substituted *N*-aryl aliphatic imines were subjected to the hydrogenation. As can be seen from Table 2.3, all the substrates examined were hydrogenated with high isolated yields and enantioselectivities. In general, higher enantioselectivities were observed for imines with bulkier *ortho* substituents on the phenyl ring. For instance, the

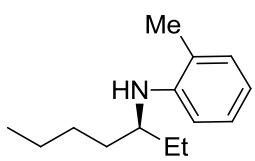
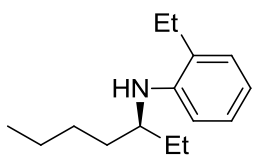
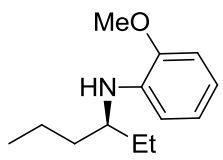
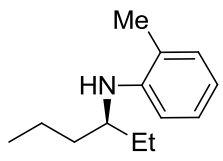
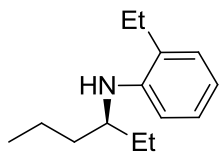
ethyl-substituted imines always afford higher ee's than their methyl analogues (Table 2.3, entries 4, 8, 11, 14 and 17 vs 2, 7, 10, 13, 16.).

Worth noting is that the catalytic system tolerates reducible C=C double bonds, affording excellent enantioselectivities (Table 2.3, entries 9-11). More remarkably, this **C₅-HA** catalyst is capable of discriminating, highly effectively, an *ethyl* from a *butyl* (Table 2.3, entries 12-14) or an *ethyl* from a *propyl* (Table 2.3, entries 15-17) group, giving ee's up to 94%. To the best of our knowledge, these ee values represent some of the highest enantioselectivities ever reported for aliphatic *N*-aryl imines. Only a few scattered examples are known where higher ee's have been observed.^{10,27}

Table 2.3: Asymmetric hydrogenation of aliphatic ketone-derived imines with **C₅-HA**^a

			
Entry	Product	Yield (%)	Ee (%) ^b
1		93	89
2		91	94
3		93	94

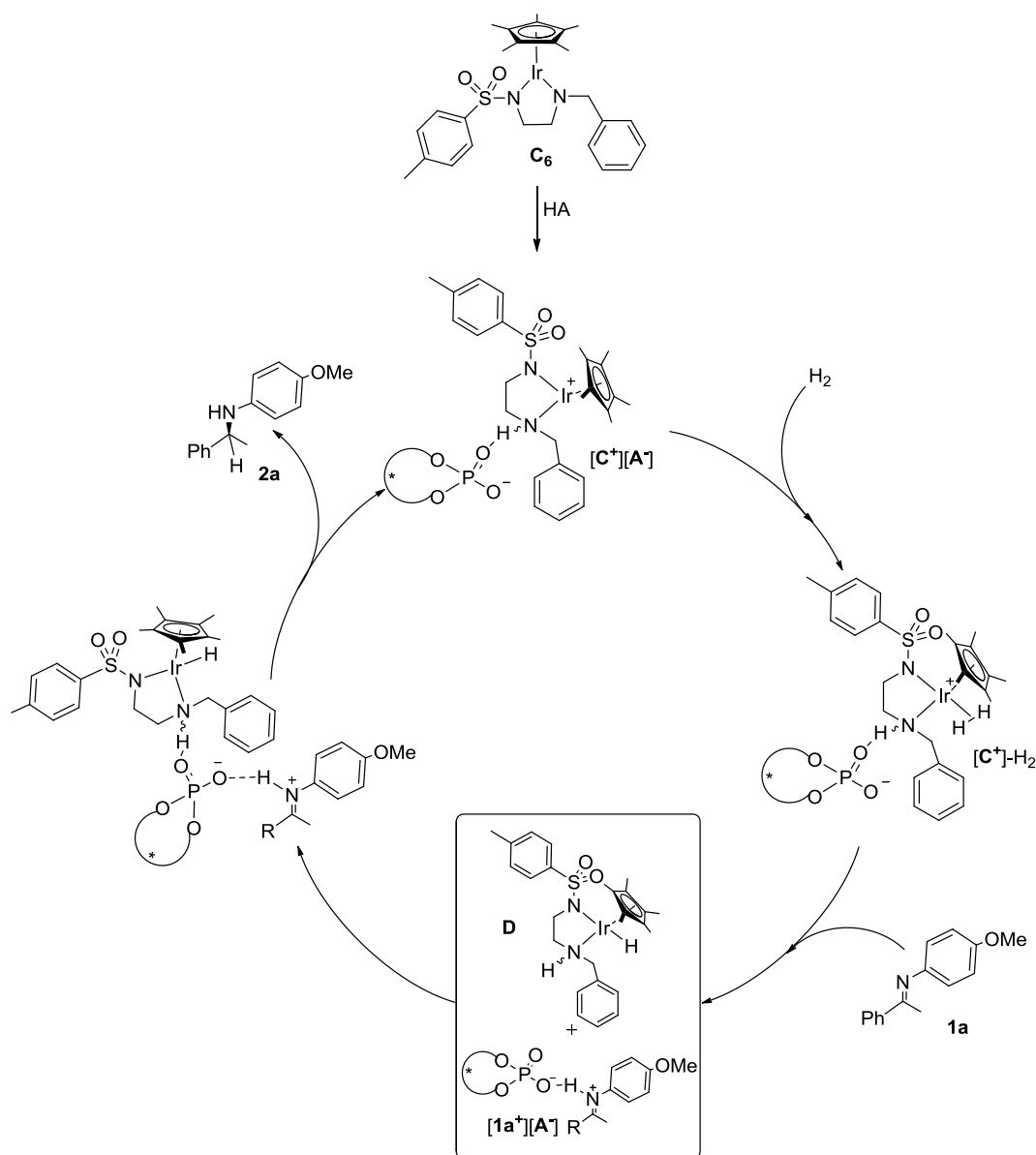
4		96	97
5		96	94
6		94	84
7		93	85
8		95	91
9		96	92
10		95	89
11		95	92
12		94	85

13		95	94
14		95	94
15		93	81
16		94	89
17		90	91

^aConditions were identical to those in Table 2, except with **C**₅ used. ^bIsolated yield.
^cEnantioselectivity determined by HPLC, with configuration assigned by analogy with the literature (See the experimental).

2.2.4 Proposed mechanism

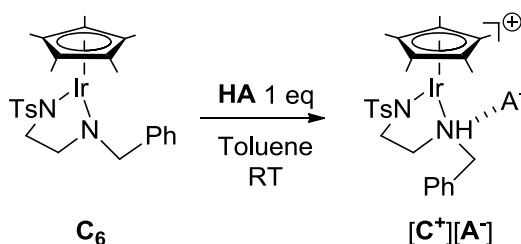
To evaluate the mechanism, a simplified achiral, neutral 16e⁻ complex **C**₆ was used, which leads to [C⁺][A⁻] upon mixing, *in situ* or *ex situ*, with the chiral phosphoric acid **HA** *via* protonation at the amido nitrogen (Scheme 2.4). In the asymmetric hydrogenation of the model ketimine **1a**, [C⁺][A⁻] afforded 95% ee and full conversion. On the basis of related studies,^{39,54,55} the hydrogenation can be broadly explained by the catalytic cycle shown in Scheme 2.4, *i.e.* [C⁺][A⁻] activates H₂ to give the hydride **D** and protonated **1a**, which ion-pairs with the phosphate affording [**1a**⁺][A⁻]; hydride transfer furnishes the amine product **2a** while regenerating [C⁺][A⁻].^{40,56-58} Questions pertinent to possible iridium-phosphate cooperation then arise: “How does the chiral phosphoric acid induce asymmetry in the hydrogenation?” and “Does the enantioselectivity result from **D** being formed *enantioselectively* from [C⁺][A⁻], from the phosphate salt [**1a**⁺][A⁻], or from interactions involving all three components?”



Scheme 2.4: Hydrogenation of imine with achiral **C₆** and chiral acid **HA** (Ar = 2,4,6-triisopropylphenyl, Ts = tosyl, Bn = benzyl).

2.2.5 Protonation of the 16e catalyst and catalyst deactivation

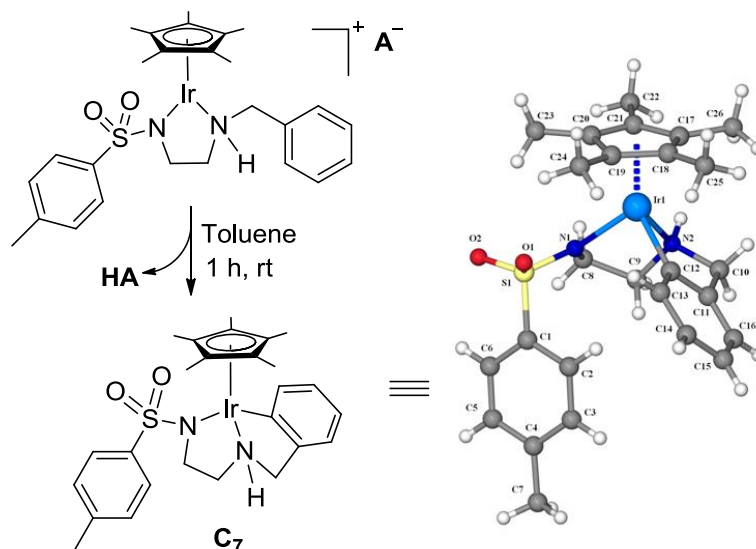
One of the first steps taken during the investigation of the mechanism was to look at the basic stoichiometric reaction of **C**₆ with **HA** (Scheme 2.5). Upon addition of one equivalent of **HA** to **C**₆ (0.05 mmol) in *d*₈-toluene (0.5 ml) immediate changes could be observed in the ¹H NMR. A new species is formed with no peaks remaining from the starting **C**₆. In particular the singlet of the benzyl CH₂ observable in **C**₆ is fully converted into an AB quartet. Further to this, hydrogen bonding can be seen due to protonation at the amido nitrogen by **HA**, with two new resonances appearing at δ 9.85 ppm and δ 10.2 ppm.



Scheme 2.5: Stoichiometric protonation of **C**₆ by **HA**.

We had previously noted that when **C**₄ or **C**₅ was mixed with **HA** in toluene in the absence of **1a** or was not used immediately upon mixing, the resulting species [**C**⁺][**A**⁻] was much less effective in catalysing the hydrogenation. With this in mind the stoichiometric reaction was left for a period of 12 hours (h), resulting in the formation of a yellow precipitate in *d*₈-toluene in the NMR tube. Isolation of this solid and subsequent ¹H NMR in CD₂Cl₂ showed a lack of **HA** resonances and by integration, the loss of an aromatic proton in **C**₆. This indicates that under such conditions, the benzyl group of the cation undergoes cyclometalation with the iridium, forming a

catalytically inactive complex (Scheme 2.6).⁵⁹ This was verified by X-ray diffraction analysis, revealing the formation of a stable cyclometalated complex **C**₇. Indeed, this complex does not catalyse the hydrogenation of **1a**. However, its formation is suppressed in the presence of an imine, presumably due to coordination of the imine to the cationic 16e iridium centre. Thus, in the absence of a coordinating substrate, [**C**⁺][**A**⁻] deactivates via cyclometalation. The above reactions were repeated in CD₂Cl₂ and again showed that the complex [**C**⁺][**A**⁻] is formed completely upon protonation of **C**₆ (0.05 mmol) with 1 eq. **HA** (0.5 mL), but without any observable formation of **C**₇ after 18 h.



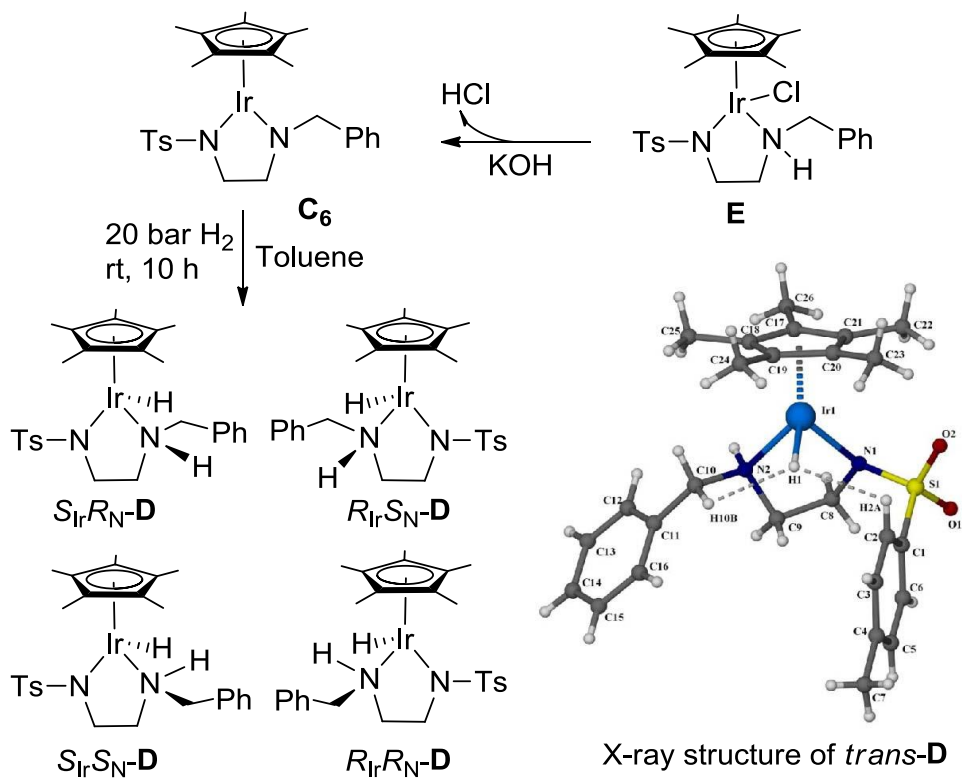
Scheme 2.6: Formation of catalytically-inactive cyclometalated complex **C**₇, from protonated **C**₆.

2.2.6 Hydride formation

We looked next at the formation of hydride **D**. The studies were mainly carried out in CH₂Cl₂ or CD₂Cl₂ due to the low solubility of the various metal complexes used in toluene. The catalytic hydrogenation is feasible in both solvents, giving a 95% ee in toluene and 85% ee in CH₂Cl₂ in the case of **1a** hydrogenation with **C**₆ and **HA** under the standard conditions given in Table

2.2. Under H_2 pressure (>1 bar), proton transfer from a $[C^+]-H_2$ dihydrogen intermediate (not observed) to **1a** converts C^+ into the hydride **D** and affords the salt $[1a^+][A^-]$.⁴⁰ Formation of **D** took place instantly even at $-78\text{ }^\circ\text{C}$, and it is observed during catalytic turnover, indicating that the hydrogenation is rate-limited by the hydride transfer step.

Racemic **D** can be generated as a solid precipitate in toluene by hydrogenation of the neutral **C**₆, and has been characterized by X-ray crystallography, as the *trans* hydride $S_{Ir}R_N$ -**D** and its mirror image $R_{Ir}S_N$ -**D**, in which the Ir-H and N-H protons are *trans* disposed (Scheme 2.7).



Scheme 2.7: Formation of racemic hydrides **D** by hydrogenating **C**₆ generated from **E** and the X-ray structure of *trans*-**D**.

1H NMR spectrum of **D** displays two hydride resonances (δ_H , $20\text{ }^\circ\text{C}$ in CD_2Cl_2 : *trans*-**D** = -10.81 , *cis*-**D** = -11.74 ; in d_8 -toluene: *trans*-**D** = -10.55 , *cis*-

D = -11.37 ppm) in the ratio of 10.5:1. Using ^1H 2D-NOESY measurements in CD_2Cl_2 taken under 20 bar H_2 , we are able to assign these signals to *trans*- $S_{\text{Ir}}R_{\text{N}}$ -**D** and its mirror image, and to the analogous *cis*- $S_{\text{Ir}}S_{\text{N}}$ -**D** and its enantiomer (Figures 2.2 & 2.3), *trans*-**D** being the more abundant. A clear NOE signal was observed between the NH proton (δ 4 ppm) of the minor species and the minor hydride signal (δ -11.71 ppm) (Figure 2.2), confirming the minor species as the *cis* hydride. A 1D ^1H overlay (Figure 2.3) clearly demonstrates the assignment to the minor N-H species rather than the major N-H species. The *trans*-**D** shows no signal between the hydride and N-H with only the benzyl CH_2 and two CH's from the backbone giving NOE signals.

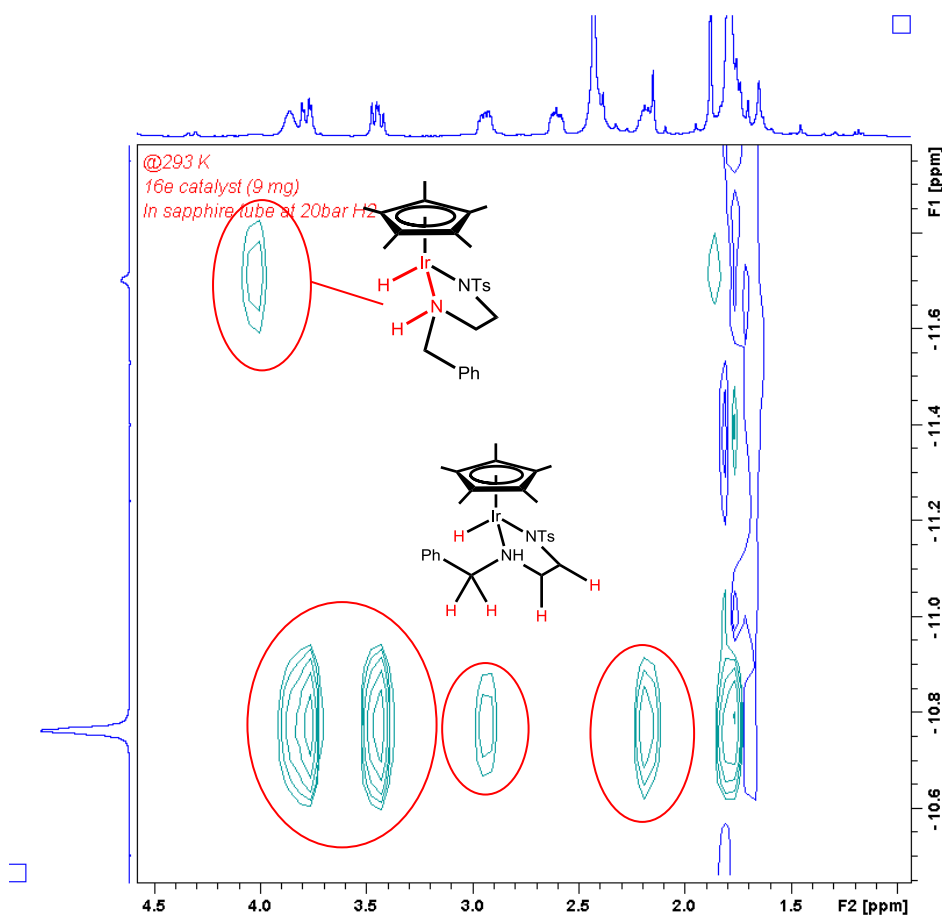


Figure 2.2. ^1H NOESY NMR of **D** showing clear NOE signal between the minor hydride species and minor N-H.

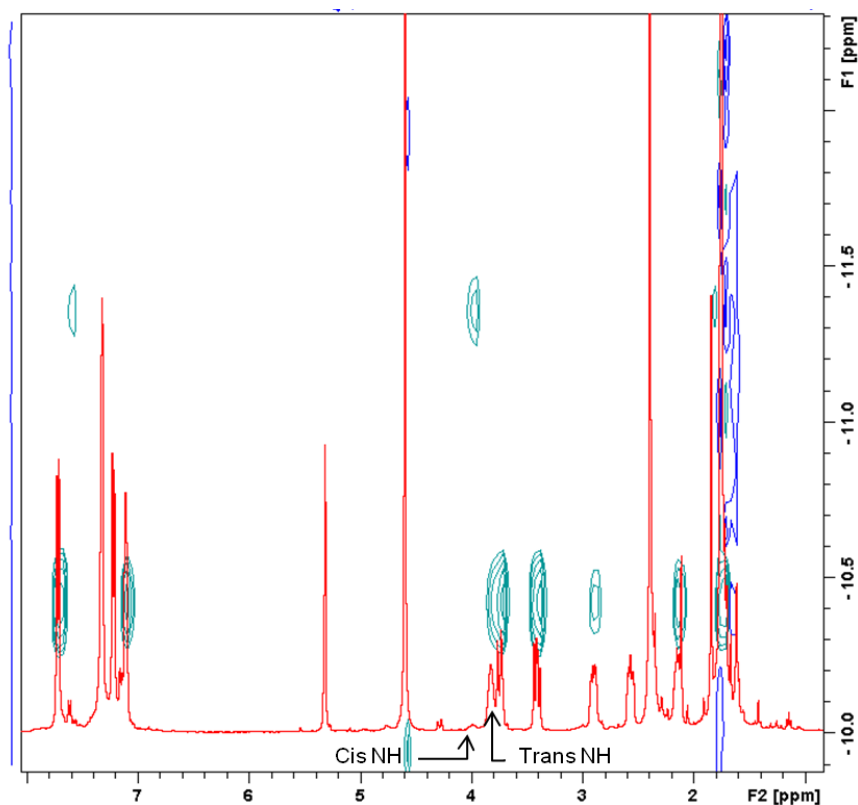


Figure 2.3. ^1H NOESY NMR of **D** with 1D ^1H NMR overlay.

Remarkably, the hydride signals of the enantiomers of *trans*-**D** can be resolved in a d_8 -toluene solution by addition of $[\text{NBu}_4^+][\text{A}^-]$ (Figure 2.4). The enantiomers of the *cis* hydride could not be resolved, however.

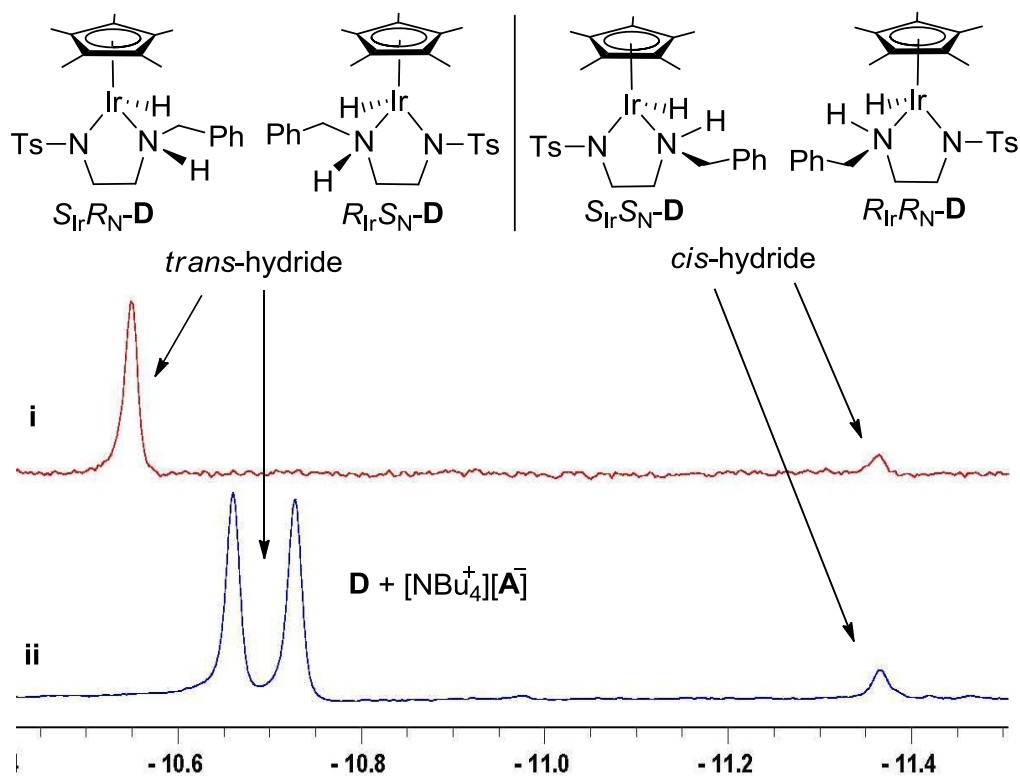


Figure 2.4: ¹H NMR spectra of 0.05 mmol **D** (i) and **D** + 0.1 mmol [NBu₄⁺][A⁻] (ii) in *d*₈-toluene (0.5 mL) at 20 °C.

Further support for the presence of additional isomers of **D** in solution is found in the X-ray crystal structure of the analogous chloride complex **E** (Figure 2.5), in which two *trans* and one *cis* isomers are observed.

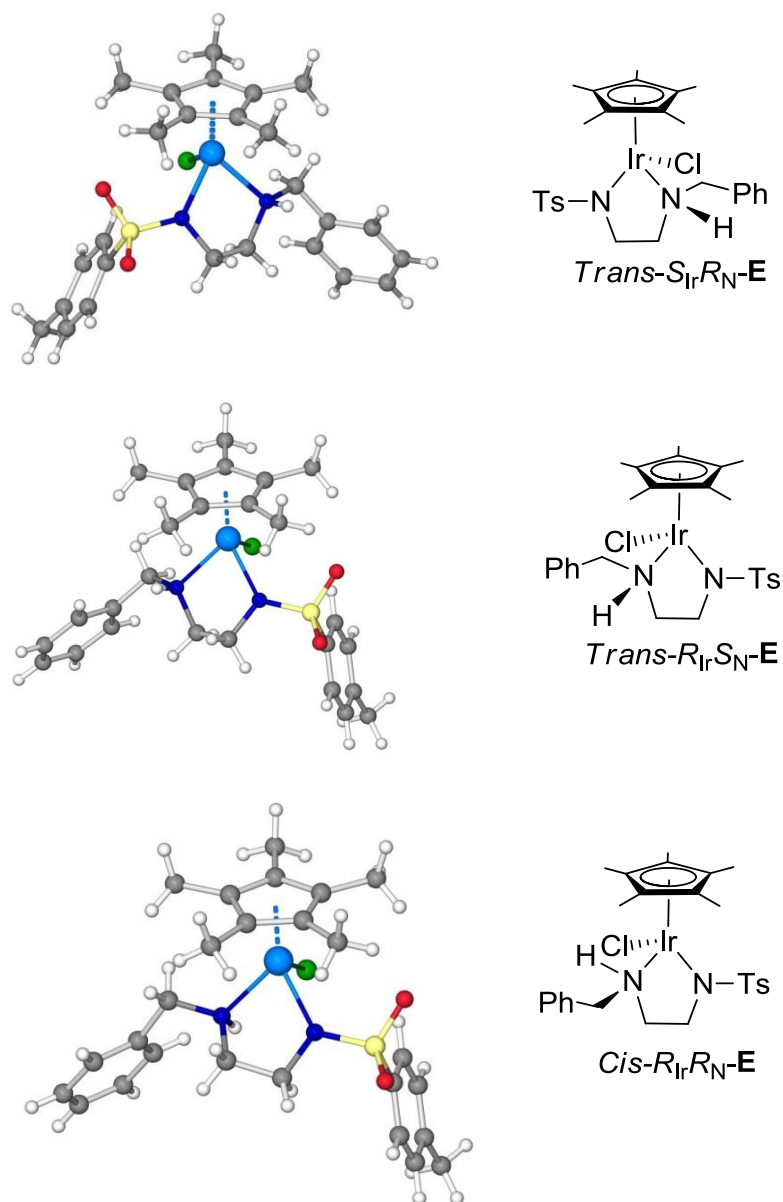
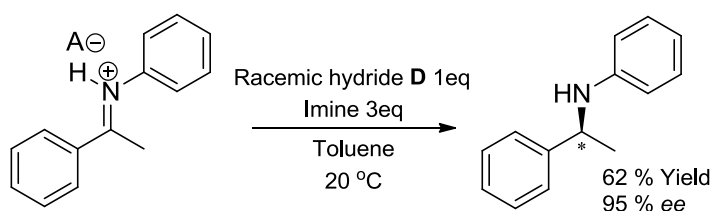


Figure 2.5: X-ray crystal structure of the chloride complex **E** showing the three isomers formed.

Under catalytic conditions, the hydride **D**, produced from hydrogenation of $[\text{C}^+][\text{A}^-]$, is also racemic and can be precipitated and isolated by performing the hydrogenation in the presence of 2,6-lutidine in toluene. This demonstrates that the hydride is not formed selectively and is not the step that accounts for the high enantioselectivities. When **D** was used in the

stoichiometric reduction of $[1a^+][A^-]$ at 20 °C in toluene (Scheme 2.8), **2a** was formed with the same ee (95%) as obtained under catalytic conditions, suggesting that the asymmetric induction of the catalysis arises in the hydride transfer step, rather than from enantioselective generation of **D**. Under the same conditions, the neutral imine **1a** cannot be reduced, however. This observation, which resembles those made in related studies, indicates that it is the iminium cation that participates in the hydride transfer.^{39,54}



Scheme 2.8: Reduction of $[1a^+][A^-]$ by **D** at 20 °C in toluene at 20 °C.

2.2.7 Importance of hydrogen bonding

Monitoring the 1H NMR of stoichiometric reactions of racemic **D** with imine and **HA** in the hydride region reveals *trimolecular interactions*. Thus, addition of **1a** to a solution of **D** at -50 °C does not appear to affect the hydrides (Figure 2.6, compare i and ii), consistent with **1a** not being reduced by **D**. However, on addition of 1 equivalent of **HA** at -50 °C, $[1a^+][A^-]$ is formed instantly, and new resonances are seen in both the hydride region, $\delta_H = -9.25$ and -9.45 ppm (Figure 2.6, iii), and at low-field in the region expected for hydrogen bonded N-H in **D**, $\delta_H = 10.00$ and 10.34 ppm with an intensity ratio similar to that of the two new hydride peaks.

To gain insight into the hydrogen bonding between A^- , the iminium nitrogen and the Ir-hydride, we treated the chloride complex **E** with 20 bar H_2

in CD_2Cl_2 in the presence of NaBARF (sodium tetrakis[3,5-bis(trifluoromethyl)phenyl]borate) and excess **1a**; this afforded only the racemic hydride **D** with no hydrogen-bonded hydrides observed (Figure 2.6, compare v and vi). Unlike the phosphate **A**⁻, the BARF⁻ anion is not expected to act as a hydrogen bond acceptor. Similarly, on hydrogenation of [**F**⁺][**A**⁻] (Figure 2.6, vii), in which the NH hydrogen is replaced with a methyl, only two hydrides, at -11.39 and -11.44 ppm, were observed in the ¹H NMR spectrum, with no observable hydrogen-bonded species. Furthermore, when **D** was mixed with [**NBu**₄⁺][**A**⁻], no new hydride resonances were observed in CD_2Cl_2 , in contrast to the case of **D** being mixed with [**1a**⁺][**A**⁻]. These observations suggest that in the hydrogen bonded network formed by **D**, **1a**⁺ and **A**⁻, the NH hydrogen of the former two hydrogen-bonds to the oxygen atom of the latter.

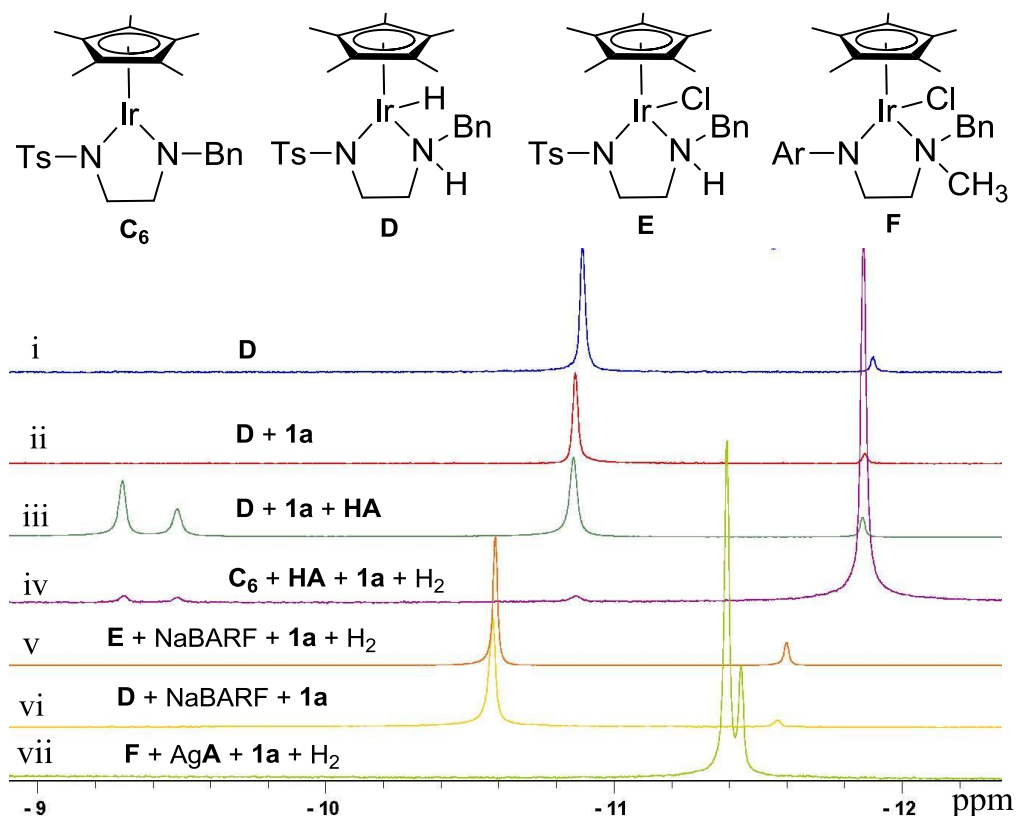


Figure 2.6: ^1H NMR spectra (0.5 mL CD_2Cl_2) of i): hydride **D** (0.05 mmol; $-50\text{ }^\circ\text{C}$); ii): i plus 10 eq. **1a**; iii): ii plus 1 eq. **HA**; iv): mixture of complex **C₆** (0.1 mmol) and 1 eq. **HA**, followed by introduction of 10 eq. **1a** and 20 bar H_2 at $-78\text{ }^\circ\text{C}$; spectrum recorded at $-50\text{ }^\circ\text{C}$; v): complex **E** (0.05 mmol) together with 2 eq. NaBARF and 10 eq. **1a**; 20 bar H_2 gas charged at $-78\text{ }^\circ\text{C}$ and spectrum recorded at $-50\text{ }^\circ\text{C}$; vi): hydride **D** with 2 eq. NaBARF and 10 eq. **1a**; vii): complex **F** (0.1 mmol, Ar = 2,4,6-triisopropylphenylsulfonyl) plus silver phosphate (1 eq. AgA) and 10 eq. **1a**; 20 bar H_2 charged at $-78\text{ }^\circ\text{C}$ and spectrum recorded at $-50\text{ }^\circ\text{C}$.

We then monitored, by *in situ* ^1H HPNMR, the reaction of $[\text{C}^+][\text{A}^-]$ under 20 bar H_2 in the presence of excess of **1a** as the temperature is raised from -78 to $20\text{ }^\circ\text{C}$. At low temperature ($-50\text{ }^\circ\text{C}$), both **D** (*trans* and *cis* isomers) and the hydrogen-bonded hydrides were observed (Figure 2.6, iv). At this temperature no observable hydrogenation took place. However, contrary to the reaction at higher temperature, the *cis* hydride is favored. On raising the

temperature, the *trans* isomer becomes the major species observed and subsequent cooling does not alter the equilibrium, consistent with a kinetic effect in operation. The lower activation energy characterizing formation of the *cis* hydride may be a result of hydrogen bonding-assisted heterolysis of H₂ (Figure 2.7).⁶⁰ Comparing the spectra iv and iii (Figure 2.6) shows that the intensity of the hydrogen-bonded hydrides varies with that of free *trans*-**D**, suggesting that the hydrogen-bonded hydrides arise from the *trans* hydrides.

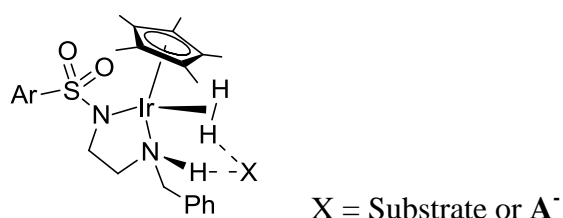


Figure 2.7: A plausible model for the preferential formation of *cis*-hydride at low temperature.

Further ¹H NMR monitoring suggests that it is the minor *cis* hydride that hydrogenates **1a**⁺ (Figure 2.8). We started from the free racemic hydride **D** with a ratio of free *trans* to free *cis* hydride 10.5 : 1 at -50 °C in the presence of 10 equivalents of **1a** (Figure 2.8, i). After addition of 1 equivalent of **HA** at the same temperature, two peaks can be seen between -9.2 and -9.6 ppm. The ratio of these two peaks added together to the free *trans*- and *cis*-hydride is *ca* 7:7:1, indicating again that the new hydrogen-bonding hydrides derive from *trans*-**D** (Figure 2.8, ii). Increasing temperature led to continued decrease in the content of the *cis*-hydride, and this is accompanied with the appearance of amine product at -20 °C. Thus, comparing the conditions i and vii, the ratio of free *trans*- to free *cis*-hydride has changed from approximately 10.5:1 to 22:1.

These observations suggest, surprisingly somehow, that it is the minor *cis*-hydride that hydrogenates **1a**⁺, instead of the major *trans*-hydride which forms observable hydrogen bonding with the organocatalyst, an inference reminiscent of the observations made in the seminal study of asymmetric hydrogenation of dehydroamino acids with Rh-diphosphine catalysts.^{61,62}

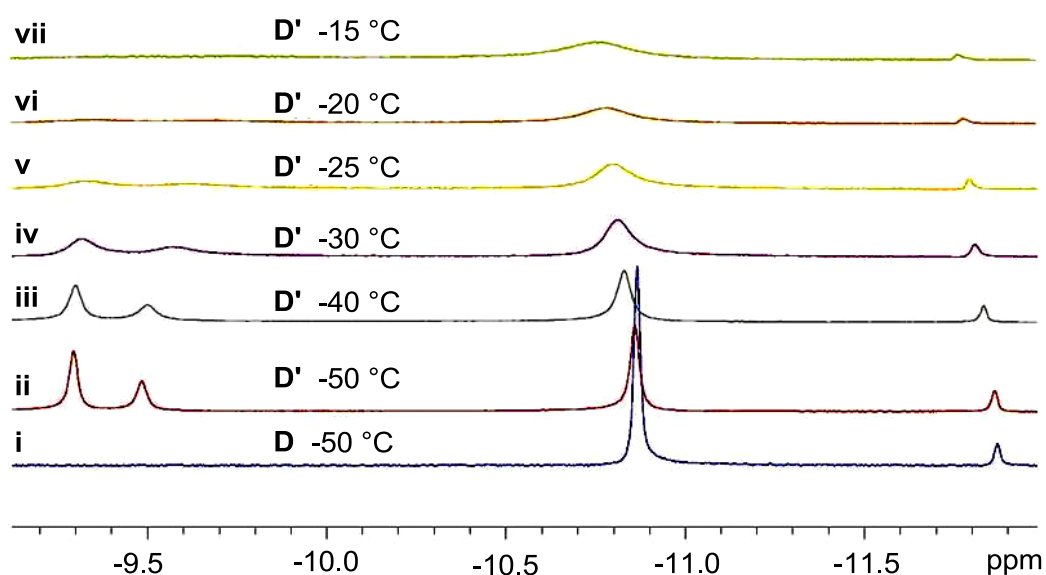
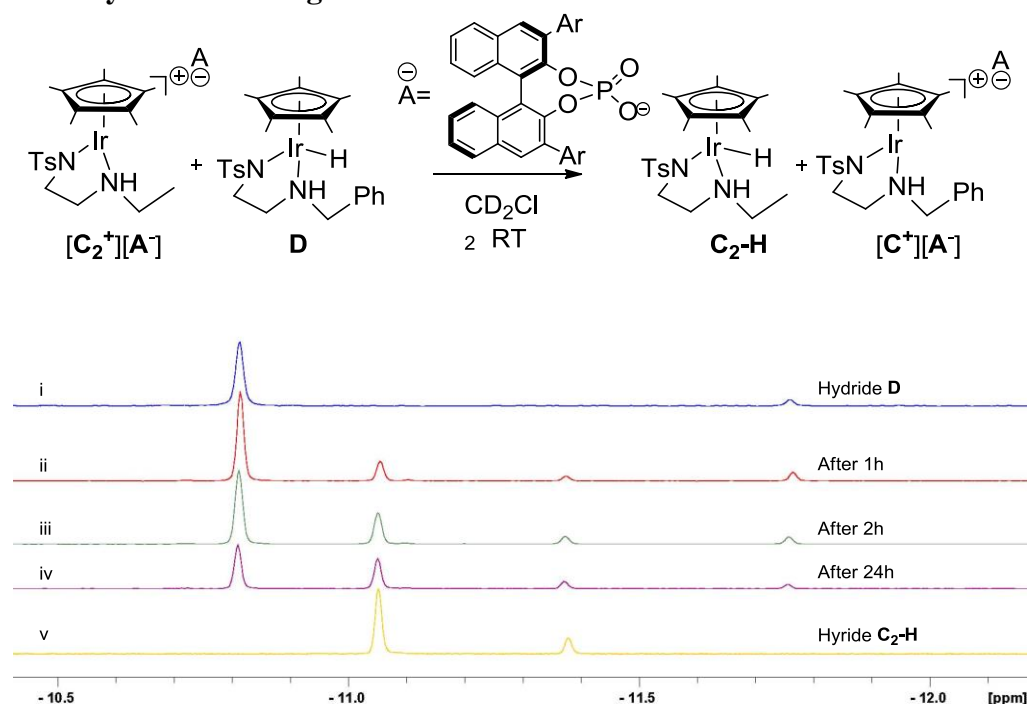


Figure 2.8: ¹H NMR monitoring of hydride transfer from hydride **D** to imine **1a** in CD₂Cl₂

(0.05 mmol **D**; **D'** = **D** + 10 eq. **1a** + 1 eq. **HA**) at various temperatures.

2.2.8 Hydride Exchange



Scheme 2.9: ^1H NMR monitoring of hydride transfer from hydride **D** (0.05 mmol) to complex $[\text{C}_2][\text{A}^-]$ (0.05 mmol) in CD_2Cl_2 (0.5 ml) over 24 h at RT.

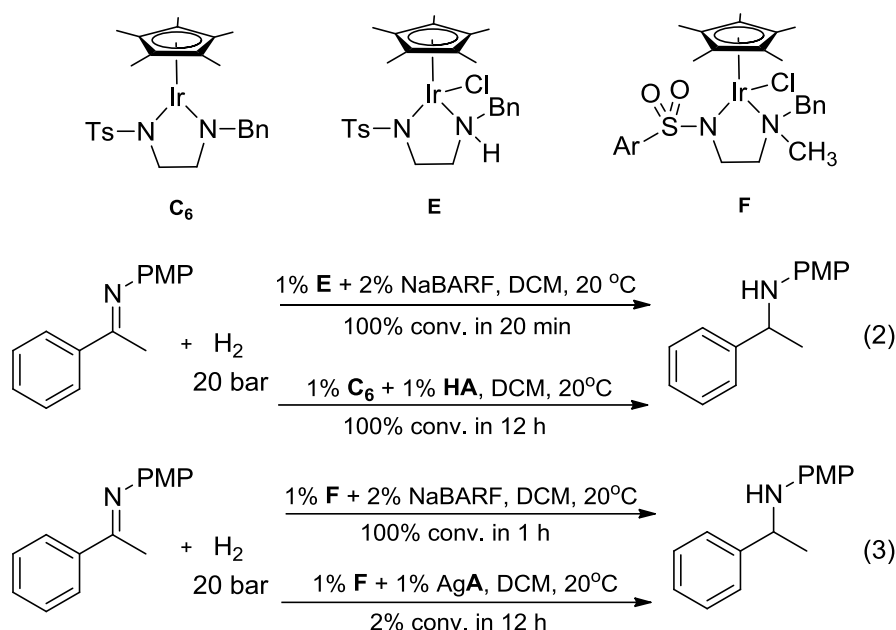
With ^1H NMR monitoring suggesting that it is the minor *cis* hydride that carries out the hydrogenation and Scheme 2.8 showing that the racemic hydride gives 95% ee, the question of hydride exchange then arises. To achieve this high selectivity in the racemic reaction the hydrides would have to exchange from the *trans* hydride to the *cis* hydride. With this in mind, $[\text{C}_2][\text{A}^-]$ was added to an NMR tube along with **D** and 1 equivalent of **HA** and left for 24 h with spectra recorded periodically. The spectra show that after 1 hour there is a small amount of hydride exchange from **D** to $[\text{C}_2][\text{A}^-]$ to form **C₂-H**, with over 50% exchanged after 24 h (Scheme 2.9 ii vs iv). This demonstrates that it is possible for the *trans* and *cis* hydrides to exchange during the course of the hydrogenation although on a slower timescale than would be needed for

the observed rate. Dehydrogenation of the *trans* hydride and hydrogenation to reform more active *cis* hydride is probably helping to achieve the high selectivities.

2.2.9 Importance of hydrogen bonding and the effect of the chiral phosphate on the rate of reaction

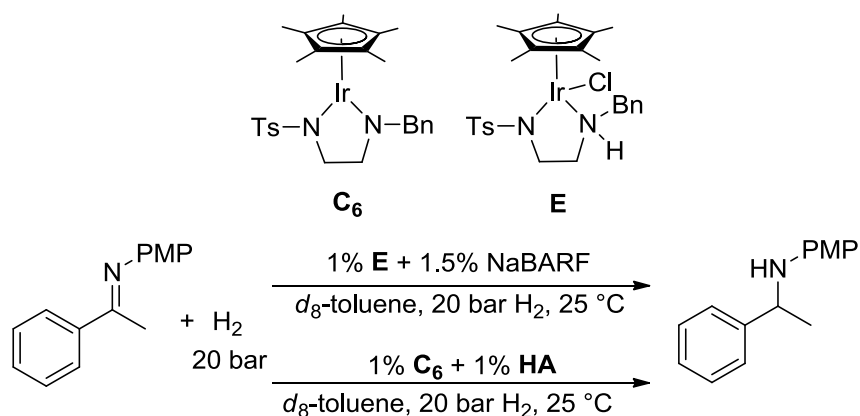
The importance of the intermolecular hydrogen bonding is seen in the hydrogenation of **1a** using $[\mathbf{C}^+][\text{BARF}^-]$ as the catalyst generated by metathesis of **E** with NaBARF, which is much faster (full conversion in 20 min) than using $[\mathbf{C}^+][\mathbf{A}^-]$ (full conversion in 12 h). The non hydrogen-bonding BARF anion means that the hydride transfer from the iridium to the “naked” iminium cation can be much faster, but with no enantioselectivity (Scheme 2.10, Eq 2).

For the same achiral reaction, $[\mathbf{F}^+][\text{BARF}^-]$ afforded full conversion in 1 h; but extremely slow hydrogenation was observed when using $[\mathbf{F}^+][\mathbf{A}^-]$ (<2% conversion in 12 h), emphasising the need for the hydrogen bonding NH functionality in the case of \mathbf{A}^- being the counteranion (Scheme 2.10, Eq 3).



Scheme 2.10: The hydrogenation of **1a** with catalysts derived from **F** or **E** with NaBARF vs **C₆** and **HA**.

Thus, although the organocatalyst renders the hydrogenation enantioselective, the bulkiness of **A⁺** inhibits the reduction of **1a⁺**. And somehow paradoxically, the reduction occurs only as a result of **A⁺** hydrogen bonding with **D**. We then followed these reactions with the use of *in situ* ¹H HP NMR at a constant H₂ pressure of 20 bar at 25 °C. Scheme 2.11 gives the details of the two specific reactions examined and Figures 2.9 & 2.10 give the conversion-time profiles obtained.



Scheme 2.11: Comparison of the hydrogenation of **1a** with catalysts derived from **E** and NaBARF vs **C₆** and **HA**.

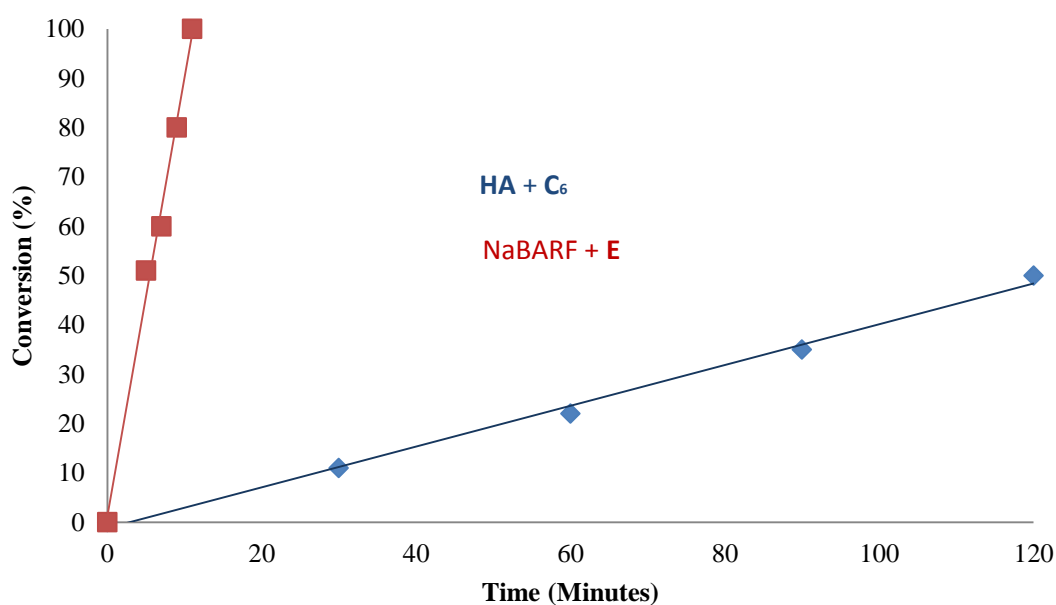


Figure 2.9: Time profiles for the hydrogenation of **1a** with catalysts derived from NaBARF vs **HA** monitored over 120 minutes by *in situ* ¹H HP NMR. Reactions were carried out with 0.09 mmol substrate in 0.5 mL *d*₈-toluene, at 20 bar H₂ and 25 °C.

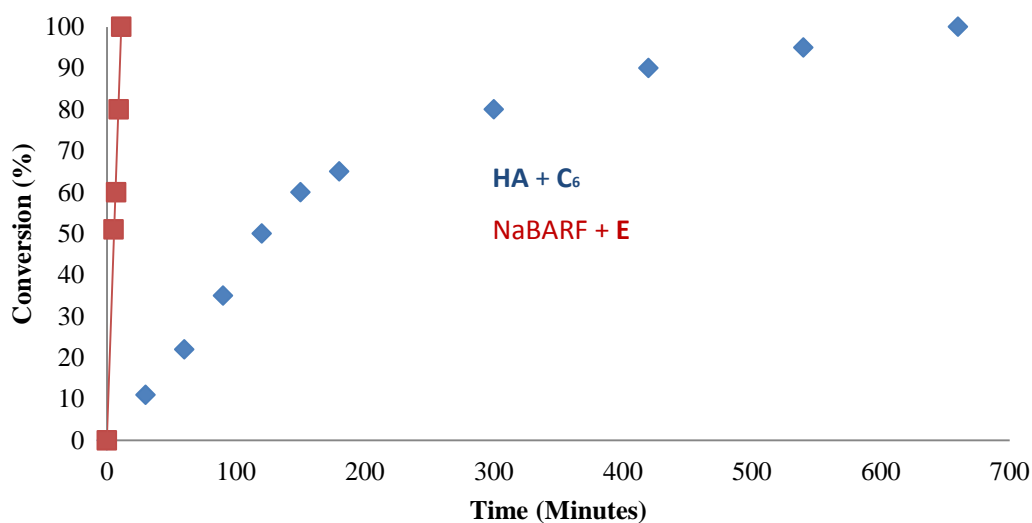


Figure 2.10: Time profiles for the hydrogenation of **1a** with catalysts derived from **E** + NaBARF vs **C₆** + **HA** monitored by *in situ* ¹H HP NMR. Reactions were carried out with 0.09 mmol substrate in 0.5 mL *d*₈-toluene, at 20 bar H₂ and 25 °C.

Examination of the profiles reveals that the initial rate of the hydrogenation with **E**-NaBARF is 22 times faster than that with **C₆**-**HA**. More interestingly, the former proceeds with approximately a constant rate whilst the latter becomes much slower after the first few hours, suggesting that the counteranion alters the reaction mechanism. The linear dependence of the conversion on time in the case of **E**-NaBARF is consistent with fast, non-turnover-limiting hydride transfer to the iminium ion over the entire course of the reaction, whereas with **C₆**-**HA** the catalytic turnover is likely to be controlled by hydride transfer to the iminium ion. These observations, together with those before, add more support to the view that the bulkiness of the chiral acid inhibits the reduction of the imine and yet paradoxically, the reduction occurs enantioselectively only as a result of the phosphate hydrogen-bonding with both the metal catalyst and the substrate.

2.3 Conclusions and future work

We have developed a new metal-organo cooperative catalytic system, in which a chiral Brønsted acid induces chirality in an achiral metal-catalysed hydrogenation. The catalyst is highly efficient, affording excellent enantioselectivities and high isolated yields in hydrogenation of imines derived from either aryl or aliphatic ketones, thus opening up a new avenue for accessing chiral amines. The mechanism proceeds *via* an ionic mechanism with the key hydride transfer step being carried out by the minor *cis* hydride species, mediated by the hydrogen bonding counterion of the Brønsted acid. However, the enantioselectivity is attained at the expense of reaction rate, due to the steric hindrance created by the chiral counteranion.

Further work was directed at gathering structural information of the key hydride delivery step utilising NMR and computational modeling methods. This information would then allow for all factors influencing the high selectivity to be elucidated.

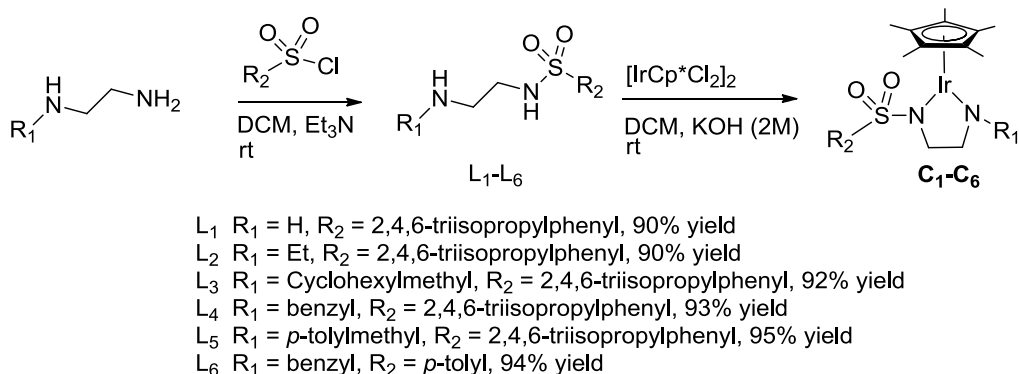
2.4 Experimental

2.4.1 General information

Unless otherwise noted, all experiments were carried out using standard Schlenk techniques. ^1H and ^{13}C NMR spectra were recorded on a Bruker Avance DMX 400 Spectrometer (^1H 400 MHz and ^{13}C 100 MHz, respectively). Chemical shifts are given in ppm and are referenced to residual solvent peaks. Single crystal X-ray data were collected on a Bruker D8 diffractometer with an APEX CCD detector and 1.5 kW graphite monochromated Mo radiation. All

organic solvents were dried using standard published methods and were distilled before use. All other chemicals were used as received from Aldrich, Alfa Aesar or Acros without further purification.

2.4.2 General procedure for the synthesis of achiral 16e Ir complexes



For $\text{L}_2\text{-L}_6$: to a solution of diamine⁶³ (2.0 mmol) and Et_3N (2.2 mmol) in dichloromethane (DCM) (10 mL), sulfonyl chloride was added (2.0 mmol) and the mixture stirred for 2 h at room temperature. Upon completion of the reaction, the solution was transferred to a short silica gel column and eluted with EA/DCM (1:1); white solid was obtained in high yield (90-95%). L_1 was synthesized via sulfonylation of ethylenediamine (20 mmol) with 2,4,6-triisopropylbenzenesulfonyl chloride (2 mmol) in CH_2Cl_2 (10 mL) at 0 °C for 5 h. Subsequent washing with water, drying with MgSO_4 , and removal of the solvent gave a yield of 90%, which was used for the next reaction directly.

Treatment of the white solid (L_{1-6}) (0.11 mmol) in DCM (2.0 ml) with $[\text{IrCp}^*\text{Cl}_2]_2$ (0.05 mmol, L/Ir = 1.1/1) in the presence of 2 M KOH solution (150 μl , 0.3 mmol) at rt for 20 min afforded a deep red solution, which was washed with distilled water three times and dried with MgSO_4 . The DCM was

removed under reduced pressure, affording the achiral Ir complexes as purple red solids, which were used as catalysts directly.

2.4.3 Synthesis of Ir-Cl complex E

The chloride complex was prepared using the same method as for complexes **C** except with 1.1 eq. triethyl amine used, instead of KOH. The resulting light orange solution was washed with water and dried with MgSO₄, and after removal of the solvent under reduced pressure, an orange-red colored solid was formed. The compound was recrystallized from a DCM/hexane solution (86% yield). The crystal was analyzed by X-ray diffraction (Appendix I).

2.4.4 Synthesis of tetra-(*N*-butyl)ammonium phosphate salt [NBu₄⁺][A⁻]

To a solution of silver phosphate salt (0.4 mmol) in DCM (5 mL) was added 1 equivalent of NBu₄Cl in H₂O (1 mL). The mixture was stirred for 1 h and the separated organic solvent extracted with DCM (3 x 5 mL). Following removal of solvent, the combined extracts were dried with 4Å MS, affording a white solid (99% yield).

2.4.5 Synthesis of *N*-methyl-*N*-benzyl substituted Ir-Cl complex F

The compound was synthesized according to the reported literature method.⁵³ A mixture of *N*-(2-(benzyl(methyl)amino)ethyl)-2,4,6-triisopropylbenzenesulfonamide (0.11 mmol),^{64,65} K₂CO₃ (25 mg) and [Cp*IrCl₂]₂ (0.05 mmol) was stirred for 20 h in dried DCM (2.0 mL). The

resulting light orange colored slurry was filtered and the solvent removed, affording an orange solid. The compound was recrystallized from DCM/hexane (80% yield).

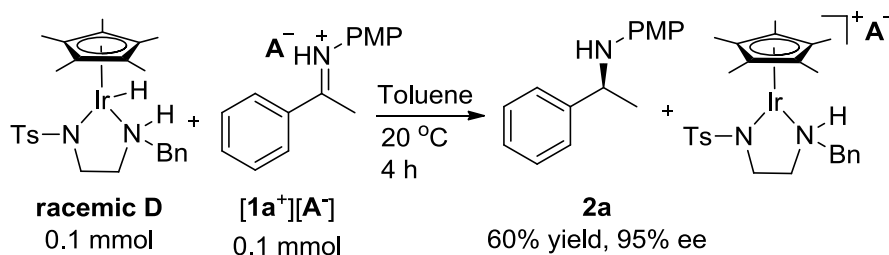
2.4.6 Synthesis of **C**₇

For **C**₇, a solution of **C**₆ (0.05 mmol) and **HA** (0.05 mmol) in toluene was stirred at room temperature for 12 h. Upon completion of the reaction, the yellow solid precipitate was isolated by removing the upper solvent layer, and washing with toluene (4x 4 ml). The yellow solid was then recrystallized in a Hexane/DCM mixture.

2.4.7 Procedure for *in-situ* NMR with high H₂ pressure at low temperature

To a sapphire tube was added complex **C**₆ (3.3 mg, 0.05 mmol), Brønsted acid **HA** (3.8 mg, 0.05 mmol) and imine **1a** (11.2 mg, 0.5 mmol). After being degassed with nitrogen three times, CD₂Cl₂ (0.5 mL) was added, and the mixture was cooled down to -78 °C in a acetone-dry ice bath. After charging with hydrogen (20 bar), the tube was stirred for 1 min in the acetone-dry ice bath. NMR was then recorded at -50 °C.

2.4.8 Stoichiometric reduction with racemic hydrides



An oven-dried glass tube was charged with toluene (0.7 mL), imine **1a** (0.1 mmol) and 4Å MS (100 mg). The mixture was stirred for 10 min, and then **HA** (0.1 mmol) was added. After stirring for another 10 min, the racemic hydride **D** was added in one portion. The mixture was stirred for 5 h and filtered to remove 4Å MS. After removal of the solvent, the product was purified and examined by ¹H NMR and HPLC.

2.4.9 Assignment of hydride D by ¹H NOESY measurements

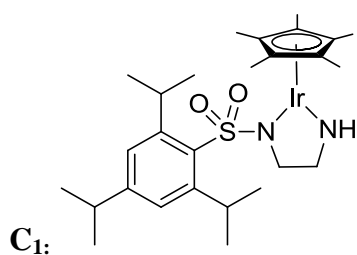
The NMR measurement was carried out on a 400MHz Avance Bruker spectrometer equipped with a TBI 1H/31P/BB HR probe. Spectra were obtained on natural isotope abundance samples at 295 K at 20 bar of H₂. **C₆** (9 mg) was dissolved in CD₂Cl₂ (0.5 mL) and charged with H₂ to 20 bar at room temperature. 2-Dimensional homonuclear ¹H-¹H NOESY were employed utilizing pulse sequences supplied by the manufacturer. Sequences were set up as follows: NOESY data matrix 2048x512, 64 scans 16 dummy scans, 50 ms and 500 ms mixing times.

2.4.10 General procedure for *in situ* ^1H HPNMR monitoring

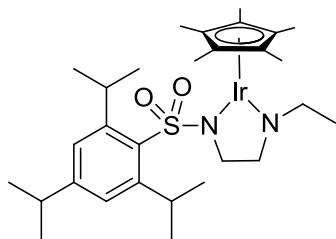
The NMR measurements were carried out on a 400MHz Avance Bruker spectrometer equipped with a TBI 1H/31P/BB HR probe using a 5mm sapphire tube fitted with a constant flow of hydrogen. To the sapphire tube was added complex **C₆** or **E** (0.0009 mmol), Brønsted acid **HA** (0.0009 mmol), or NaBARF (0.0014 mmol), imine **1a** (20 mg, 0.09 mmol) and *d*₈-toluene (0.5 mL). The mixture was cooled to -50 °C in the NMR machine and the tube charged with hydrogen (20 bar). Once the required pressure had been reached the sample was warmed to 25 °C over a five minute period. ^1H NMR spectra were recorded after the five minutes, once a constant temperature had been reached. Spectra were then recorded at regular intervals to track the reaction.

2.5 Analytical data

2.5.1 Analytical data for iridium complexes

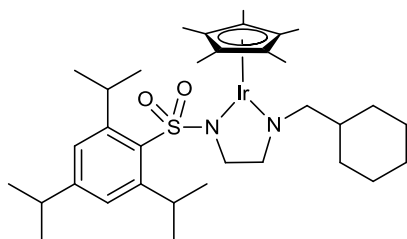


^1H NMR (CD_2Cl_2 , 400 MHz, T = 263K) δ 7.06 (s, 2H), 5.66 (br, 1H), 4.35-4.38 (m, 2H), 2.80-2.86 (m, 3H), 2.53-2.57 (m, 2H), 1.83 (s, 15H), 1.13-1.20 (m, 18H) ppm; ^{13}C NMR (CD_2Cl_2 , 100 MHz, T = 263K) δ 151.23, 150.89, 135.60, 123.58, 85.44, 58.69, 55.15, 34.62, 29.33, 25.49, 24.15, 10.75 ppm; HRMS could not be obtained due to instability.



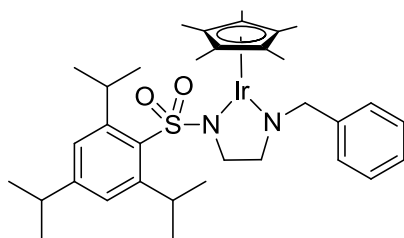
C₂:

¹H NMR (CD₂Cl₂, 400 MHz) δ 7.08 (s, 2H), 4.39-4.46 (m, 2H), 3.62-3.67 (m, 2H), 2.83-2.90 (m, 1H), 2.61-2.65 (m, 2H), 2.49-2.53 (m, 2H), 1.87 (s, 15H), 1.09-1.27 (m, 21H) ppm; ¹³C NMR (CD₂Cl₂, 100 MHz) δ 151.27, 151.22, 135.53, 123.68, 85.76, 64.89, 60.98, 54.31, 34.83, 29.49, 25.50, 24.30, 15.90, 10.99 ppm; HRMS (ES⁺) calcd. for C₂₉H₄₈N₂O₂SIr¹⁹³ [M+H]⁺: 681.3066; found: 681.3069.



C₃:

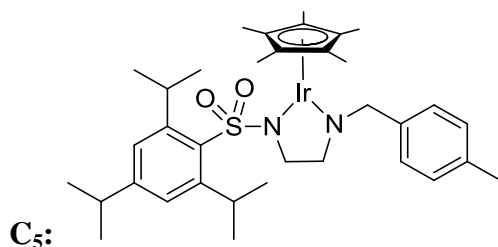
¹H NMR (CD₂Cl₂, 400 MHz) δ 7.08 (s, 2H), 4.40-4.46 (m, 2H), 3.41-3.43 (d, *J* = 6.8 Hz, 2H), 2.85-2.90 (m, 1H), 2.58-2.62 (m, 2H), 2.45-2.52 (m, 2H), 1.84 (s, 15H), 1.59-1.73 (m, 7H), 1.15-1.24 (m, 22H) ppm; ¹³C NMR (CD₂Cl₂, 100 MHz) δ 150.11, 135.30, 122.53, 84.60, 72.36, 64.84, 37.97, 33.69, 30.78, 28.36, 26.60, 25.97, 24.36, 23.15 ppm; HRMS (ES⁺) calcd. for C₃₄H₅₆N₂O₂SIr¹⁹³ [M+H]⁺: 749.3669, found: 749.3687.



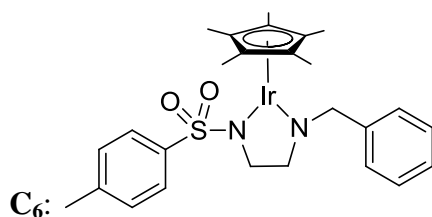
C₄:

¹H NMR (CD₂Cl₂, 400 MHz) δ 7.17-7.23 (m, 4H), 7.10-7.14 (m, 1H), 7.00 (s, 2H), 4.75 (s, 2H), 4.32-4.39 (m, 2H), 2.74-2.81 (m, 1H), 2.57-2.61 (m, 2H), 2.35-2.38 (m, 2H), 1.73 (s, 15H), 1.04-1.18 (m, 18H) ppm; ¹³C NMR (CD₂Cl₂, 100 MHz) δ 151.43, 151.27, 141.09, 136.07, 129.07, 127.37, 127.27, 123.74,

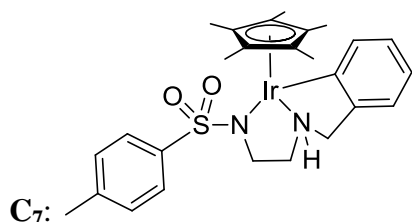
86.14, 68.96, 65.10, 54.84, 34.84, 29.59, 25.54, 25.43, 24.30, 10.86 ppm;
HRMS (ES+) calcd. for $C_{34}H_{50}N_2O_2SiIr^{193}$ $[M+H]^+$: 743.3222; found: 743.3188.



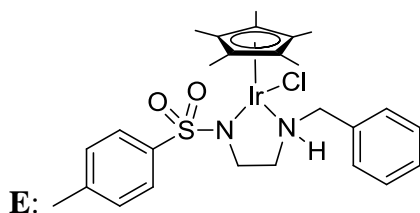
1H NMR (CD_2Cl_2 , 400 MHz) δ 7.09-7.15 (m, 4H), 7.07 (s, 2H), 4.78 (s, 2H), 4.41-4.48 (m, 2H), 2.82-2.89 (m, 1H), 2.64-2.67 (m, 2H), 2.41-2.44 (m, 2H), 2.30 (s, 3H), 1.82 (s, 15H), 1.17-1.23 (m, 18H) ppm; ^{13}C NMR (CD_2Cl_2 , 100 MHz) δ 151.00, 150.88, 137.52, 136.50, 135.75, 129.32, 126.91, 123.32, 85.71, 68.44, 64.65, 54.23, 34.43, 29.17, 25.12, 23.88, 21.14, 10.45 ppm; HRMS (ES+) calcd. for $C_{35}H_{52}N_2O_2SiIr^{193}$ $[M+H]^+$: 757.3379; found: 757.3414.



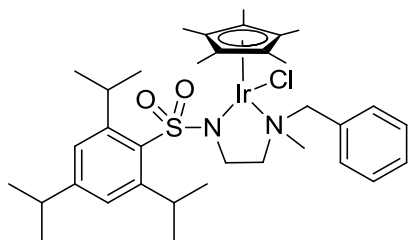
1H NMR (CD_2Cl_2 , 400 MHz) δ 7.69-7.71 (m, 2H), 7.28-7.31 (m, 2H), 7.18-7.23 (m, 5H), 5.77 (s, 2H), 3.00-3.03 (m, 2H), 2.38 (s, 3H), 2.27-2.30 (m, 2H), 1.74 (s, 15H) ppm; ^{13}C NMR (CD_2Cl_2 , 100 MHz) δ 143.71, 141.42, 140.39, 129.64, 129.10, 127.55, 127.44, 127.26, 86.27, 70.08, 64.84, 55.37, 21.89, 10.43 ppm; HRMS (ES+) calcd. for $C_{26}H_{34}N_2O_2SiIr^{193}$ $[M+H]^+$: 631.1970; found: 631.1987.



¹H NMR (CD₂Cl₂, 400 MHz) δ 7.80 (d, *J* = 7.5 Hz, 1H), 7.11 (d, *J* = 8.0 Hz, 2H), 6.97-7.06 (m, 2H), 6.94 (d, *J* = 8.0 Hz, 2H), 6.88 (t, *J* = 7.5 Hz, 1H), 4.73 (s, 1H), 3.95 (dd, *J* = 5.1, 13.8 Hz, 1H), 3.84 (d, *J* = 13.8 Hz, 1H), 2.41-2.66 (m, 3H), 2.39 (s, 3H), 1.83-1.93 (m, 1H), 1.80 (s, 15H) ppm; ¹³C NMR (CD₂Cl₂, 100 MHz) δ 164.34, 141.83, 139.68, 137.80, 128.30, 127.45, 126.61, 121.84, 120.84, 87.05, 63.91, 55.73, 52.42, 20.88, 9.13 ppm; HRMS (ES⁺) calcd. for C₂₆H₃₄N₂O₂SIr¹⁹³ [M+H]⁺: 631.1964; found: 631.1975.



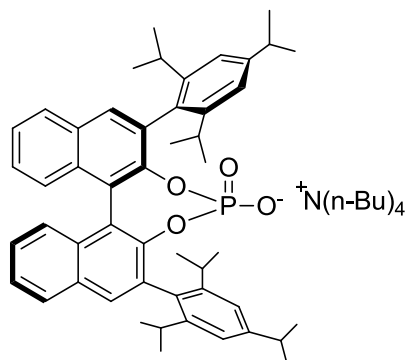
¹H NMR (CD₂Cl₂, 400 MHz, T = 273 K): A mixture of *trans* and *cis* (referring to the relative position of the chloride and NH proton) compounds with a ratio of 2:1; The X-ray diffraction structures are shown in Appendix I; *trans*-**E** δ 7.73-7.75 (d, *J* = 8.08 Hz, 2H), 7.34 (m, 3H), 7.23-7.25 (m, 2H), 7.10-7.12 (d, *J* = 8.00 Hz, 2H), 4.53-4.56 (d, *J* = 12.00 Hz, 1H), 3.93-3.97 (m, 1H), 3.80-3.82 (m, 1H), 2.79-2.83 (dd, *J* = 4.40, *J* = 10.80 Hz, 1H), 2.60-2.63 (d, *J* = 9.20 Hz, 1H), 2.38-2.43 (m, 1H), 2.30 (s, 3H), 2.16-2.20 (m, 1H), 1.73 (s, 15H) ppm; *cis*-**E** δ 7.98-8.00 (d, *J* = 8.00 Hz, 2H), 7.34 (m, 3H), 7.23-7.26 (m, 2H), 7.15-7.17 (d, *J* = 8.00 Hz, 2H), 4.29-4.36 (m, 1H), 4.07-4.09 (d, *J* = 8.00 Hz, 1H), 3.98-4.00 (m, 1H), 2.73-2.74 (m, 1H), 2.43-2.49 (m, 1H), 2.33 (s, 3H), 2.30-2.33 (m, 2H), 1.75 (s, 15H) ppm; ¹³C NMR (CD₂Cl₂, 100 MHz, T = 273 K) of the mixture compounds δ 141.19, 140.40, 140.18, 136.14, 129.57, 129.20, 129.08, 128.72, 128.69, 128.30, 128.22, 128.09, 86.08, 85.40, 59.32, 57.51, 54.48, 51.12, 48.44, 21.18, 9.61, 9.23 ppm; HRMS (ES⁺) calcd. for C₂₆H₃₄N₂O₂SIr¹⁹³ [M-Cl]⁺: 631.1970; found: 631.1990.



F:

^1H NMR (CDCl_3 , 400 MHz) δ 7.32-7.35 (m, 3H), 7.27-7.28 (m, 2H), 7.05 (s, 2H), 4.99-5.02 (m, 1H), 4.46-4.48 (m, 2H), 4.04-4.08 (m, 1H), 2.99 (s, 3H), 2.82-2.99 (m, 3H), 1.71 (s, 15H), 1.19-1.23 (m, 18H) ppm; ^{13}C NMR (CDCl_3 , 100 MHz) δ 151.53, 150.69, 134.93, 132.43, 132.37, 129.11, 128.75, 123.51, 86.63, 66.29, 66.18, 48.79, 34.40, 29.20, 25.92, 25.89, 25.50, 25.47, 24.15, 10.73 ppm; HRMS (ES $^+$) calcd. for $\text{C}_{35}\text{H}_{52}\text{N}_2\text{O}_2\text{S Ir}^{193}$ $[\text{M}-\text{Cl}]^+$ 757.3379; found 757.3371.

2.5.2 Analytical data for tetra-(*N*-butyl)ammonium phosphate salt



[NBu $_4^+$][A $^-$]

^1H NMR (CDCl_3 , 400 MHz) δ 7.80-7.82 (d, J = 8.0 Hz, 2H), 7.71 (s, 2H), 7.32-7.36 (m, 2H), 7.16-7.24 (m, 4H), 7.08 (s, 2H), 7.00 (s, 2H), 2.98-3.21 (m, 10H), 2.88-2.95 (m, 2H), 2.69-2.76 (m, 2H), 1.34-1.42 (m, 8H), 1.27-1.30 (m, 18H), 1.11-1.20 (m, 20H), 0.82-0.92 (m, 18H) ppm; ^{13}C NMR (CDCl_3 , 100 MHz) δ 149.80, 149.70, 148.59, 147.72, 147.18, 134.66, 133.82, 133.79, 133.46, 131.56, 130.39, 128.11, 127.56, 125.42, 123.40, 120.80, 120.16, 58.66, 34.67, 31.31, 30.94, 26.79, 25.27, 24.62, 24.56, 24.35, 24.22, 23.92, 19.85, 14.10 ppm; ^{31}P NMR (CDCl_3 , 162 MHz) δ 3.95 ppm; HRMS (FAB) calcd. for anion $[\text{C}_{50}\text{H}_{56}\text{O}_4\text{P}]^-$ 751.3922; found 751.3915; calcd. for cation $[\text{C}_{16}\text{H}_{36}\text{N}]^+$ 242.2842; found 242.2841.

2.5.3 X-ray diffraction analysis and analytical data for **C₇**, **D** and **E**

The full crystallographic data for both **C₇** (CCDC 915867), **E** (CCDC888491) and **D** (CCDC888492) can be found in the attached electronic information.

2.6 References

- (1) Nugent, T. C.; El-Shazly, M. *Adv. Synth. Catal.* **2010**, 352, 753.
- (2) Xie, J. H.; Zhu, S. F.; Zhou, Q. L. *Chem. Rev.* **2011**, 111, 1713.
- (3) Blaser, H. U. *Adv. Synth. Catal.* **2002**, 344, 17.
- (4) Mrcic, N.; Minnaard, A. J.; Feringa, B. L.; de Vries, J. G. *J. Am. Chem. Soc.* **2009**, 131, 8358.
- (5) Shirai, S.; Nara, H.; Kayaki, Y.; Ikariya, T. *Organometallics* **2009**, 28, 802.
- (6) Zhou, S. L.; Fleischer, S.; Junge, K.; Beller, M. *Angew. Chem., Int. Ed.* **2011**, 50, 5120.
- (7) Chen, F.; Wang, T. L.; He, Y. M.; Ding, Z. Y.; Li, Z. W.; Xu, L. J.; Fan, Q. H. *Chem.-Eur. J* **2011**, 17, 1109.
- (8) Zhou, X. Y.; Bao, M.; Zhou, Y. G. *Adv. Synth. Catal.* **2011**, 353, 84.
- (9) Chen, F.; Ding, Z. Y.; He, Y. M.; Qin, J.; Wang, T. L.; Fan, Q. H. *Tetrahedron* **2012**, 68, 5248.
- (10) Hou, C. J.; Wang, Y. H.; Zheng, Z.; Xu, J.; Hu, X. P. *Org. Lett.* **2012**, 14, 3554.
- (11) Arai, N.; Utsumi, N.; Matsumoto, Y.; Murata, K.; Tsutsumi, K.; Ohkuma, T. *Adv. Synth. Catal.* **2012**, 354, 2089.

- (12) Werkmeister, S.; Fleischer, S.; Junge, K.; Beller, M. *Chem. Asian J.* **2012**, *7*, 2562.
- (13) Gao, K.; Wu, B.; Yu, C. B.; Chen, Q. A.; Ye, Z. S.; Zhou, Y. G. *Org. Lett.* **2012**, *14*, 3890.
- (14) Matsunaga, H.; Nakanishi, K.; Nakajima, M.; Kunieda, T.; Ishizuka, T. *Heterocycles* **2009**, *78*, 617.
- (15) Guijarro, D.; Pablo, O.; Yus, M. *Tetrahedron Lett.* **2009**, *50*, 5386.
- (16) Guijarro, D.; Pablo, O.; Yus, M. *J. Org. Chem.* **2010**, *75*, 5265.
- (17) Kwak, S. H.; Lee, S. A.; Lee, K. I. *Tetrahedron-Asymmetry* **2010**, *21*, 800.
- (18) Mikhailine, A. A.; Maishan, M. I.; Morris, R. H. *Org. Lett.* **2012**, *14*, 4638.
- (19) Sot, P.; Kuzma, M.; Vaclavik, J.; Pechacek, J.; Prech, J.; Januscak, J.; Kacer, P. *Organometallics* **2012**, *31*, 6496.
- (20) Kampen, D.; Reisinger, C.; List, B. In *Asymmetric Organocatalysis*; List, B., Ed.; Springer Berlin Heidelberg: 2009; Vol. 291, p 1.
- (21) Wang, Z. Y.; Jiang, Z. J. *Asian J. Chem.* **2010**, *22*, 4141.
- (22) de Vries, J. G.; Mrcic, N. *Catal. Sci. Tech.* **2011**, *1*, 727.
- (23) Jones, S.; Warner, C. J. A. *Org. Biomol. Chem* **2012**, *10*, 2189.
- (24) Spindler, F.; Blaser, H.-U. In *The Handbook of Homogeneous Hydrogenation*; Wiley-VCH Verlag GmbH: 2008, p 1193.
- (25) Breuer, M.; Ditrich, K.; Habicher, T.; Hauer, B.; Kessler, M.; Sturmer, R.; Zelinski, T. *Angew. Chem., Int. Ed.* **2004**, *43*, 788.

- (26) Jacobsen, E. N.; Pfaltz, A.; Yamamoto, H. *Comprehensive asymmetric catalysis* / Eric N. Jacobsen, Andreas Pfaltz, Hisashi Yamamoto (eds.) ; Berlin ; Springer, 1999.
- (27) Rubio-Perez, L.; Perez-Flores, F. J.; Sharma, P.; Velasco, L.; Cabrera, A. *Org. Lett.* **2009**, *11*, 265.
- (28) Li, C.; Wang, C.; Villa-Marcos, B.; Xiao, J. *J Am Chem Soc* **2008**, *130*, 14450.
- (29) Li, C.; Villa-Marcos, B.; Xiao, J. *J Am Chem Soc* **2009**, *131*, 6967.
- (30) Villa-Marcos, B.; Li, C.; Mulholland, K. R.; Hogan, P. J.; Xiao, J. *Molecules* **2010**, *15*, 2453.
- (31) Shao, Z.; Zhang, H. *Chem. Soc. Rev.* **2009**, *38*, 2745.
- (32) Zhong, C.; Shi, X. *Eur. J. Org. Chem.* **2010**, 2999.
- (33) Rueping, M.; Koenigs, R. M.; Atodiresei, I. *Chem.-Eur. J.* **2010**, *16*, 9350.
- (34) Allen, A. E.; MacMillan, D. W. C. *Chem. Sci.* **2012**, *3*, 633.
- (35) Stegbauer, L.; Sladojevich, F.; Dixon, D. J. *Chem. Sci.* **2012**, *3*, 942.
- (36) Yu, Z.; Jin, W.; Jiang, Q. *Angew. Chem., Int. Ed.* **2012**, *51*, 6060.
- (37) Du, Z.; Shao, Z. *Chem. Soc. Rev.* **2013**, *42*, 1337.
- (38) Bullock, R. M. *Chem.-Eur. J.* **2004**, *10*, 2366.
- (39) Guan, H.; Iimura, M.; Magee, M. P.; Norton, J. R.; Zhu, G. *J Am Chem Soc.* **2005**, *127*, 7805.
- (40) Fleischmann, M.; Drettwan, D.; Sugiono, E.; Rueping, M.; Gschwind, R. M. *Angew. Chem., Int. Ed.* **2011**, *50*, 6364.

- (41) Tang, W.; Johnston, S.; Iggo, J. A.; Berry, N. G.; Phelan, M.; Lian, L.; Bacsa, J.; Xiao, J. *Angew. Chem., Int. Ed.* **2013**, 52, 1668.
- (42) Klussmann, M. *Angew. Chem., Int. Ed.* **2009**, 48, 7124.
- (43) Hoffmann, S.; Seayad, A. M.; List, B. *Angew. Chem., Int. Ed.* **2005**, 44, 7424.
- (44) Storer, R. I.; Carrera, D. E.; Ni, Y.; MacMillan, D. W. *J Am Chem Soc* **2006**, 128, 84.
- (45) Wakchaure, V. N.; Zhou, J.; Hoffmann, S.; List, B. *Angew. Chem., Int. Ed.* **2010**, 49, 4612.
- (46) Wakchaure, V. N.; Nicoletti, M.; Ratjen, L.; List, B. *Synlett* **2010**, 2708.
- (47) Rueping, M.; Koenigs, R. M. *Chem. Commun.* **2011**, 47, 304.
- (48) Tang, W.; Johnston, S.; Li, C.; Iggo, J. A.; Bacsa, J.; Xiao, J. *Chem.-Eur. J.* **2013**, 19, 14187.
- (49) Haack, K.-J.; Hashiguchi, S.; Fujii, A.; Ikariya, T.; Noyori, R. *Angew. Chem., Int.* **1997**, 36, 285.
- (50) Heiden, Z. M.; Rauchfuss, T. B. *J Am Chem Soc* **2006**, 128, 13048.
- (51) Ohkuma, T.; Utsumi, N.; Tsutsumi, K.; Murata, K.; Sandoval, C.; Noyori, R. *J Am Chem Soc* **2006**, 128, 8724.
- (52) Ohkuma, T.; Utsumi, N.; Watanabe, M.; Tsutsumi, K.; Arai, N.; Murata, K. *Org. Lett.* **2007**, 9, 2565.
- (53) Heiden, Z. M.; Rauchfuss, T. B. *J Am Chem Soc* **2009**, 131, 3593.
- (54) Aberg, J. B.; Samec, J. S. M.; Backvall, J. E. *Chem. Commun.* **2006**, 2771.
- (55) Wang, C.; Villa-Marcos, B.; Xiao, J. *Chem. Commun.* **2011**, 47, 9773.

- (56) Macchioni, A. *Chem Rev* **2005**, *105*, 2039.
- (57) Lacour, J.; Moraleda, D. *Chem. Commun.* **2009**, 7073.
- (58) Phipps, R. J.; Hamilton, G. L.; Toste, F. D. *Nature Chemistry* **2012**, *4*, 603.
- (59) Koike, T.; Ikariya, T. *Organometallics* **2005**, *24*, 724.
- (60) Lei, M.; Zhang, W.; Chen, Y.; Tang, Y. *Organometallics* **2010**, *29*, 543.
- (61) Halpern, J. *Science* **1982**, *217*, 401.
- (62) Brown, J. M.; Chaloner, P. A. *J. Am. Chem. Soc.* **1980**, *102*, 3040.
- (63) Kruse, L. I.; Kaiser, C.; Dewolf, W. E.; Finkelstein, J. A.; Frazee, J. S.; Hilbert, E. L.; Ross, S. T.; Flaim, K. E.; Sawyer, J. L. *J. Med. Chem.* **1990**, *33*, 781.
- (64) Benarab, A.; Boye, S.; Savelon, L.; Guillaumet, G. *Tetrahedron Lett.* **1993**, *34*, 7567.
- (65) Guilford, W. J.; Dallas, J.; Arnaiz, D. *J. Labelled Comp. Radiopharm.* **2001**, *44*, 247.

Chapter 3

Cooperative Catalysis: Made Possible by Noncovalent Interactions

3.1 Introduction

Chapter 2 showed the development of an excellent system for the asymmetric reduction of imines utilising a chiral phosphoric acid and an achiral iridium catalyst. The mechanism was investigated and was determined to proceed via an ionic mechanism with a key hydride transfer step mediated by hydrogen bonding. During this key step, four chiral hydrides are formed and through *in situ* NMR studies it was determined that the *cis* orientated hydride was the active species responsible for the reduction.

The questions then arise: “How does the chiral phosphoric acid induce asymmetry in the hydrogenation?” and “Does the enantioselectivity result from both *cis* hydrides or is there only one active species?” To determine this, the nature of the noncovalent interactions between the three components needed to be established.

Non-covalent interactions, such as hydrogen bonding, electrostatic, π - π , CH- π and hydrophobic forces, play an essential role in the action of nature’s catalysts, enzymes. In the last decade these interactions have been successfully exploited in organocatalysis with small organic molecules.¹ In contrast, such interactions have seldom featured in the well established area of homogeneous organometallic catalysis, where electronic interactions via covalent bonding

and steric effects imposed by bound ligands dictate the activity and selectivity of a metal catalyst. An interesting question is: “What happens when an organocatalyst meets an organometallic catalyst?” This unification has already created an exciting new space for both fields – cooperative catalysis – in which reactants are activated simultaneously by both types of catalyst, enabling reactivity and selectivity patterns inaccessible within each field alone.²⁻⁷

To gain insight into these interactions in this metal-organo cooperative catalysis, we studied the key hydride transfer step using a range of techniques, including diffusion measurements, nuclear Overhauser effect (NOE) measurements and NOE-constrained computational modeling.

The NOE involves the transfer of spin polarisation from one nuclear spin to another via cross relaxation. This allows for the determination of NMR active nuclei in close proximity through space ($< 5 \text{ \AA}$).⁸ 2D NOE spectroscopy (NOESY) then lets these signals be correlated throughout a full system. The existence of an NOE signal between protons in the potential tertiary complex could then be used as a constraint in computational modelling.

A range of structures could then be generated to satisfy these constraints and then optimised.⁹⁻¹² The initial constrained structure optimisations could be carried out at a density functional theory (DFT) level in the gas phase using the B3LYP functional and 6-31G** basis set was used for all atoms except Ir.¹³ Relativistic effects for Ir were addressed by using LANL2DZ effective core potential (ECP) together with the LANL2DZ basis set.¹³

However, due to the need to model the full complexity of the system while taking into consideration the length of time this would require using a DFT

level of theory, full calculation of the Hessian for each system was carried out in Gaussian09 at a semi-empirical level of theory using the PM6 Hamiltonian.^{14,15}

Another part of the experimental work was the use of diffusion ordered spectroscopy (DOSY). This is a 2D NMR technique where one dimension represents the regular chemical shift information, while the other is representative of the molecular size by use of the diffusion constant. If an interaction was present between two molecules, a slower diffusion constant D would reflect this when compared to the diffusion constant D of the free molecule.

Using the pulsed field gradient spin-echo (PFGSE) developed by Stejskal and Tanner¹⁶ a spin echo sequence is implemented containing two pulsed field gradients separated by a waiting time. The effect of this is to initially defocus and then refocus the magnetisation. If the molecules diffuse after the first pulsed gradient the effective magnetisation the spins feel will be decreased by the second pulse. The result of this is that the recorded signals decrease in intensity; if the experiment is repeated with increasing gradient strength a set of signals is generated from which the diffusion constant D can be calculated.^{17,18}

This technique has been previously applied to organometallic compounds, most notably by Pregosin who has shown a range of examples including the effect of hydrogen bonding on the diffusion constant of an anion.¹⁹ The diffusion constant of an anion when interacting with an organometallic compound has a much slower diffusion constant than when the anion is measured separately. If the diffusion constant changes at a similar rate to that

of the organometallic compound, it is indicative of an interaction likely to be hydrogen bonding between the two.

The combinations of these techniques were used to probe the existence of a key tertiary structure and the results are described herein.

3.2 Results and discussion

3.2.1 NMR structural characterisation

The results reported in Chapter 2 suggest that the enantioselective hydrogenation is likely to proceed via a hydrogen bonded supramolecular complex^{20,21} involving all three of **B**, **1a**⁺ and **A**⁻ (Figure 3.1). To shed light on the structure of the predicted ternary complex, we performed ¹H PFGSE, ¹H-¹³C heteronuclear single quantum coherence spectroscopy (HSQC), ¹H NOESY NMR and DFT/semi-empirical computational studies of the model complex **C**, **HA**, and **1a** or **1b**. **1b** is more stable than **1a** and hence was used for experiments requiring relatively long time. The hydride **B** could not be used due to its reaction with **1a**⁺ or **1b**⁺ under the conditions used so complex **C** acts as a mimic.

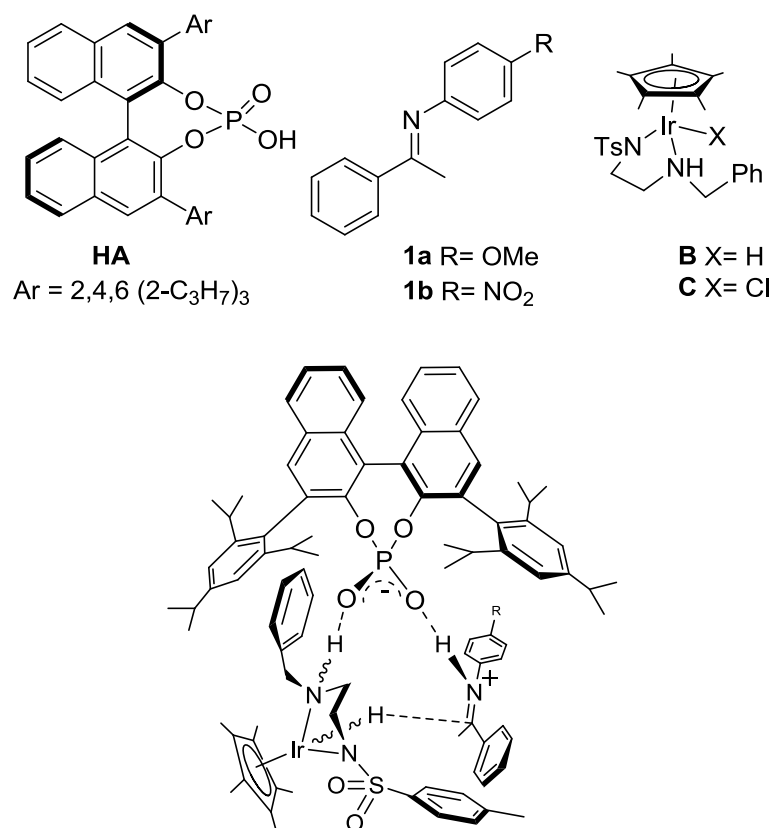


Figure 3.1: The three components used for the structural characterisation and the predicted supramolecular structure.

Each component was firstly fully characterised in CD₂Cl₂ at 293 K, so that a library of signatures could be built up to be used when analysing more complex spectra. Among the data collected was the internal NOEs present in each of the components (Figure 3.2). The identification of an NOE depends on the rate of molecular tumbling which is influenced by the molecular size. A positive NOE cross peak is observed for smaller molecules of less than 600 Da, goes through zero for MW range 600 – 1500 Da, and becomes negative for larger molecules (> 1500 Da).⁸ Apart from the low weight isolated imine, all other NOESY spectra had the existence of an NOE confirmed by observation of negative cross peaks.

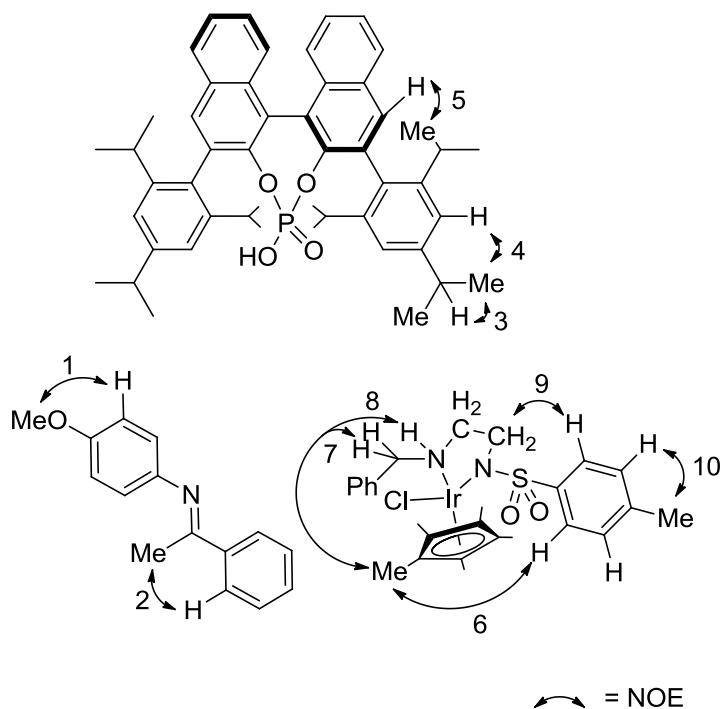


Figure 3.2: Schematic illustration of internal ^1H NOE signals between each of the three components. All NMR acquired in CD_2Cl_2 at 293 K.

In the case of **1a** these show the expected NOEs between the *para* methoxy group with the *meta* aromatic protons (Figure 3.2, 1) and the methyl group with the *ortho* aromatic protons of the non-substituted ring (Figure 3.2, 2). The rigid structure of **HA** gives rise to NOEs between each of the methyl groups to the central proton of the isopropyl groups and the aromatic protons from the substituted rings (Figure 3.2, 3&4). An additional NOE is seen from an aromatic proton on the biphenyl ring to the methyls of the isopropyl groups at the 2 and 6 positions of the substituted ring (Figure 3.2, 5). Complex **C** shows NOEs from the Cp^* ring to the *ortho* aromatic protons of the Ts ring, NH and benzyl CH_2 group (Figure 3.2, 6-8). The *ortho* aromatic protons of the Ts ring also show a signal to a CH_2 on the backbone (Figure 3.2, 9) along with

the *meta* aromatic protons showing an NOE to the tosyl methyl group (Figure 3.2, 10).

3.2.2 Structural characterisation of **HA** and **1a**

The spectra for the mixture of 1 eq **HA** with 1 eq **1a** in CD_2Cl_2 shows one new set of peaks in the ^1H NMR and one new peak formed in the ^{31}P NMR shifted 1.5 ppm upfield from free **HA**, corresponding to a newly formed complex. Assignment of the NOE signals show that apart from the internal NOEs previously calculated there is a new signal between **HA** and **1a**. This signal arises between the *ortho* aromatic protons of the substituted ring of **1a** and the methyl groups from the 2 and 6 positioned isopropyl groups of **HA** (Figure 3.3, 11).

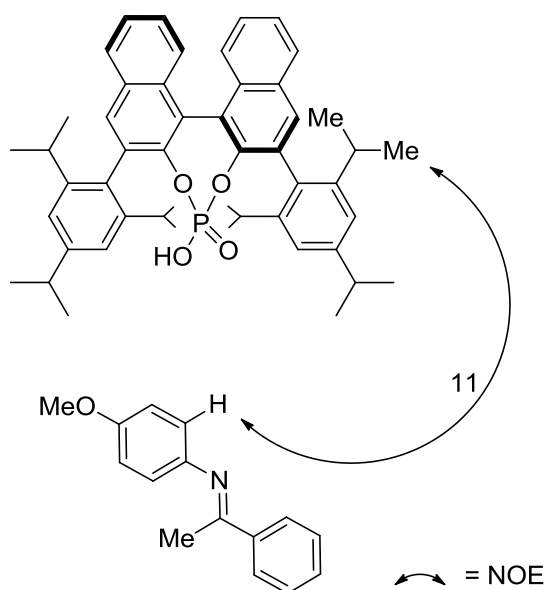


Figure 3.3: Schematic illustration of the intramolecular ^1H NOE signal for **HA** and **1a**.

NMR acquired in CD_2Cl_2 at 293 K.

These NOE signals were then taken as constraints in structural calculation and optimizations at DFT level of theory. A range of initial structures were built which met the required NOE constraints with no distances exceeding 5 Å, which were then optimised. Once an optimised structure had been found, the restraints were removed and the structure reoptimised locating the local energy minima. The resulting lowest energy structure that is consistent with the observed NOEs is shown below (Figure 3.4) in which **1a** is protonated and hydrogen bonding to **HA** (NH--O=P distance = 1.44 Å).

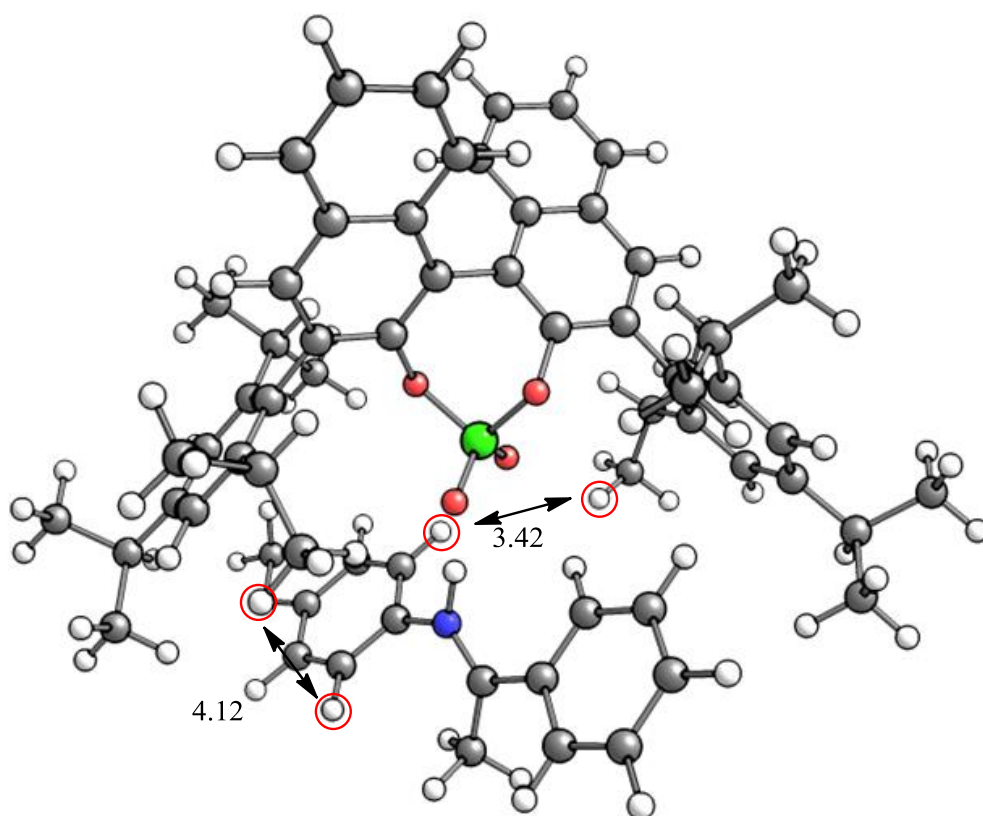


Figure 3.4: Fully optimised structure based on NOE constraints of **HA** and **1a**. Structures optimised at B3LYP/6-31G**/LANL2DZ. Grey = C, white= H, red = O, green = P, blue = N.

Distance in Å.

3.2.3 Structural characterisation of **HA** + **C**

Upon mixing of 1 eq **HA** and 1 eq **C** in CD_2Cl_2 the ^1H NMR shows a new sets of peaks formed in comparison to the free molecules, with two peaks observable at δ 9.42 and δ 11.45 ppm consistent with the region associated with hydrogen bonds. Complex **C** has both *trans* and *cis* orientations in a 2:1 ratio and the hydrogen bonding signals maintain this ratio. From the ^1H 2D-NOESY a range of intramolecular NOE signals were determined (Figure 3.5, 11-16). These further confirm the interaction between **HA** and **C** and could be used in the more complex NMR to discount any of this population.

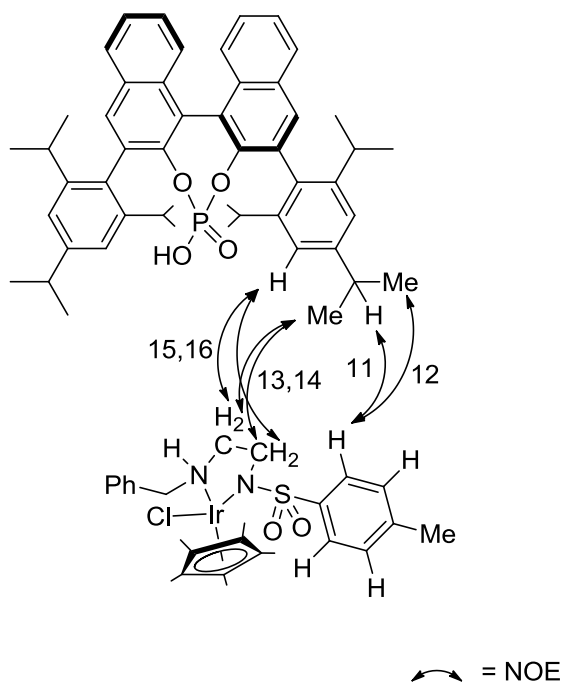


Figure 3.5: Schematic illustration of ^1H NOE signals for **HA** and **C**.

NMR acquired in CD_2Cl_2 at 293 K.

3.2.4 Structural characterisation of tertiary structure via NMR

The ^1H - ^{13}C HSQC and ^1H NOESY NMR spectra of a mixture of **HA** (0.1 mmol), 1 equivalent (eq.) **C** and 1 eq. **1a** at 800 MHz in CD_2Cl_2 (0.5 mL) allowed for the identification of a range of NOE signals. In the multiple-component spectra several sets of resonances could be observed arising from the mixture of the molecular combinations (single component vs. multiple components). Resonances belonging to either the isolated or multiple-molecular forms previously determined could be distinguished by comparison to the spectra of the individual and hetero-dimer components.

In the **HA-C-1a** sample no evidence of free acid or catalyst was observable although resonances deriving from **HA-C** were discernible. NOEs assigned in the **HA-C-1a** were compared to those observed in the **HA-C** and **HA-1a** samples to differentiate between NOEs from **HA-C** or **HA-C-1a**. Although the majority of NOEs could not be unambiguously assigned to **HA-C**, **HA-1a** or **HA-C-1a**, two NOEs were identified as deriving from the ternary complex and used to aid selection of the appropriate models (Figures 3.6-3.9).

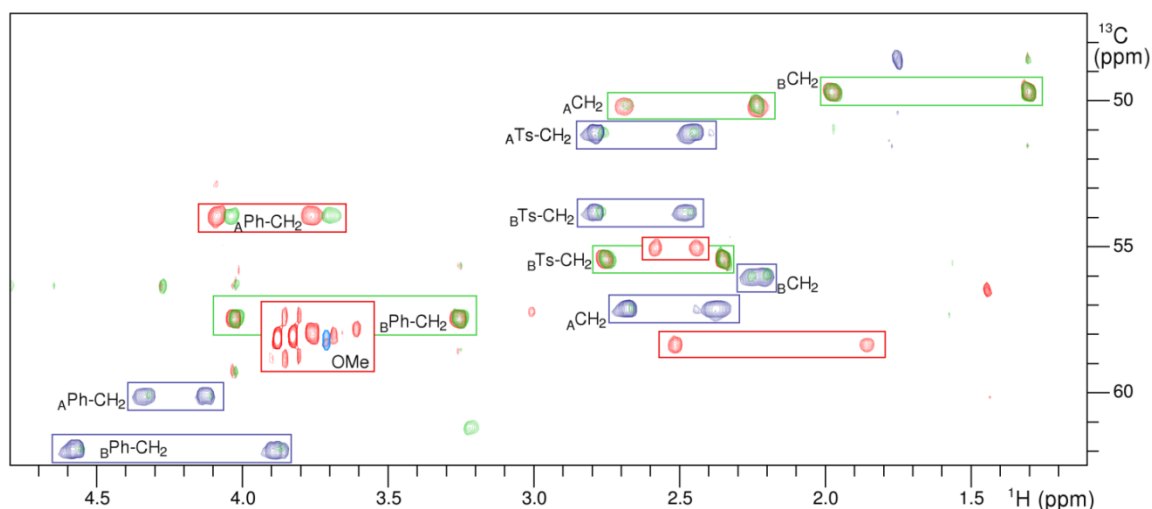


Figure 3.6: ^1H - ^{13}C HSQC spectra of **C** (dark blue), **C-HA** (green), **1a** (light blue) and **C-HA-1a** (red). Peaks attributed to unbound **C** are indicated by blue boxes, peaks attributed to the **C-HA** complex are indicated by green boxes, peaks attributed to the triple **C-HA-1a** complex are indicated by red boxes. Assigned peaks marked A or B indicate they derive from different, yet unidentified, isoforms of the catalyst. All NMR acquired in CD_2Cl_2 at 293 K.

The two NOE signals were identified as being unambiguously derived from the ternary complex (Figure 3.7, 17 & 18). They arise from the methoxy group of **1a**⁺ and the isopropyl-substituted aryl ring of **A**⁺, and the methyl group of **1a**⁺ and the tosyl ring of **C**, supporting the hypothesized supramolecular complex (Figure 3.8 & 3.9).

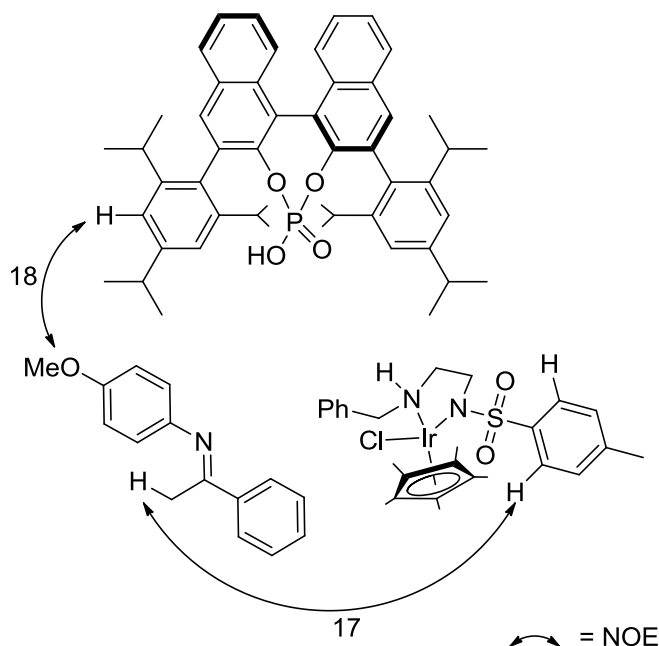


Figure 3.7: Schematic illustration of ^1H NOE signals between the three components.

NMR acquired in CD_2Cl_2 at 293 K.

These NOE signals were then taken as constraints in structural calculation and optimisation. A range of structures were generated for each of the four configurations of **C** via conformational searching using molecular mechanics with the force field MMFF94. The most popular structures, which satisfied the key NOE signals, were further optimised (Figure 3.10). Structure optimisations were carried out at density functional theory (DFT) level in the gas phase using the B3LYP functional. For all the optimisations the 6-31G** basis set was used for all atoms except Ir.¹³ Relativistic effects for Ir were addressed by using LANL2DZ effective core potential (ECP) together with the LANL2DZ basis set.¹³

Due to the need to model the full complexity of the system while taking into consideration of the length of time this would require using a DFT level of theory, subsequent calculations were carried out in Gaussian09 at a semi-

empirical level of theory using the PM6 Hamiltonian.^{14,15} A further optimisation followed by vibrational frequency calculations were carried out to confirm the nature of the stationary point on the potential energy surface. The resulting structures were then analysed to see if the minima satisfied the key NOEs.²²

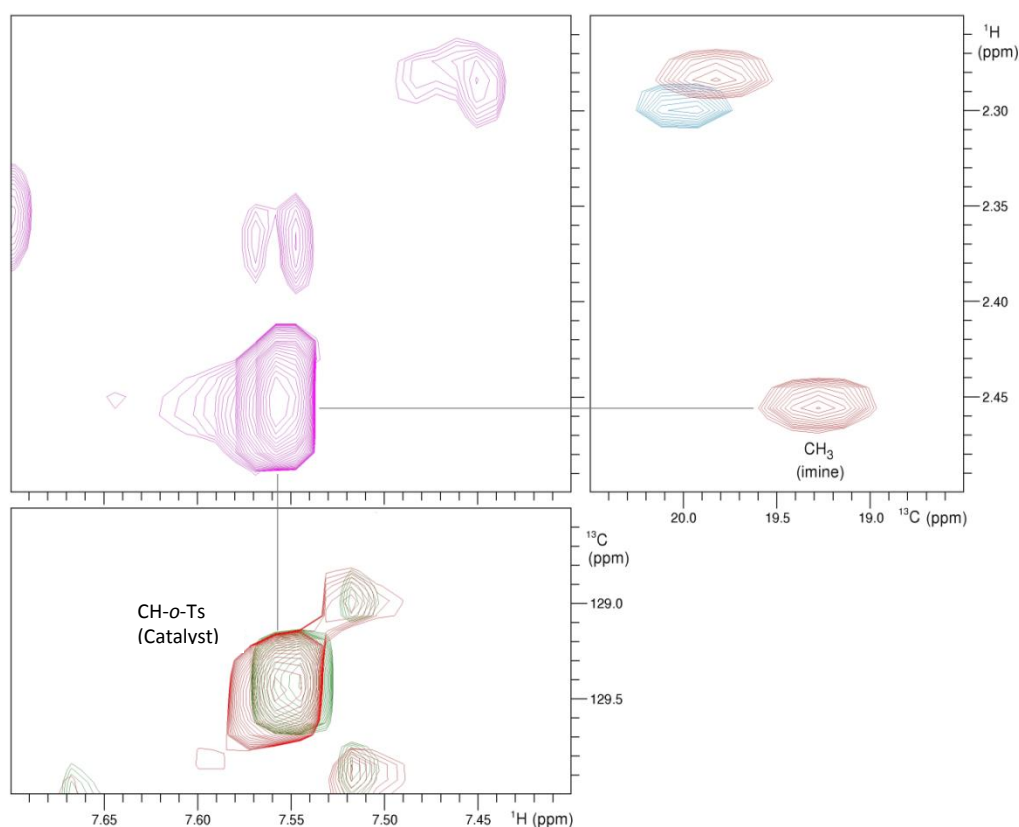


Figure 3.8: ^1H - ^{13}C HSQC (bottom and right panels) spectra of **C** (dark blue), **C-HA** (green), **1a** (light blue) and **C-HA-1a** (red). The corresponding **C-HA-1a** ^1H - ^1H NOESY is shown in magenta (top-left panel). The NOESY peak indicated by grey lines corresponds to an intermolecular NOE between a CH on the tosyl group of **C** and the methyl group of **1a** and derives from resonances only observable in the triple precatalyst-acid-imine complex. NMR acquired in CD_2Cl_2 at 293 K.

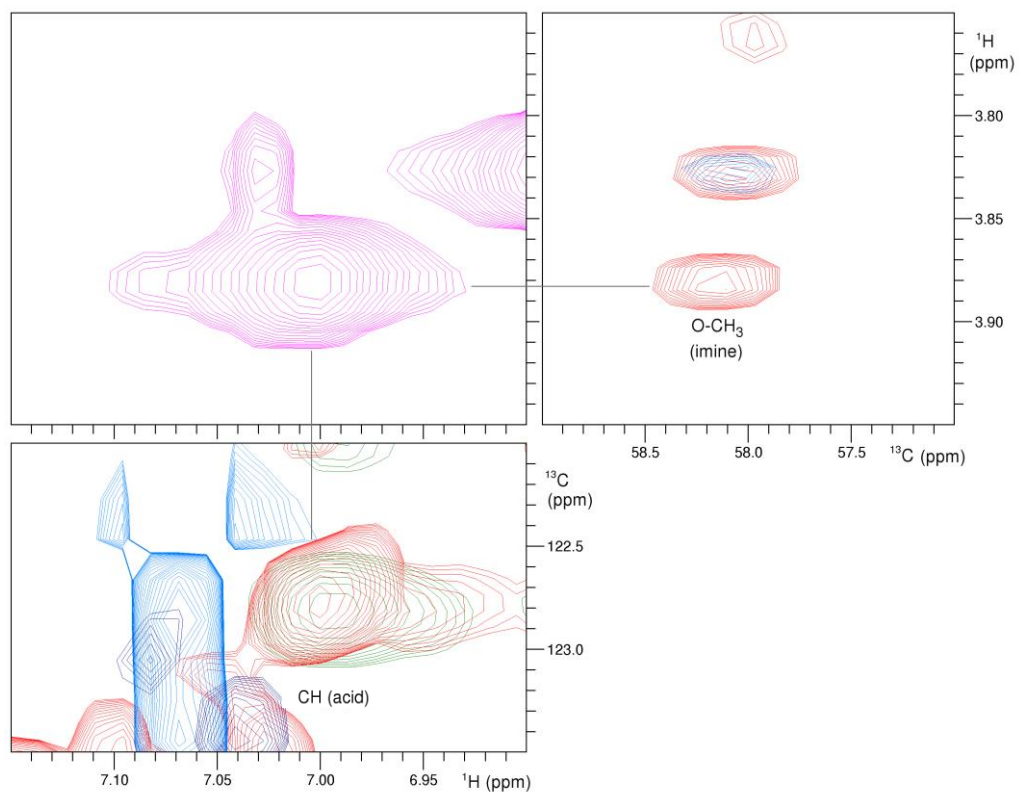


Figure 3.9: ^1H - ^{13}C HSQC (bottom and right panels) spectra of **C-HA** (green), **1a** (light blue) and **C-HA-1a** (red). The corresponding **C-HA-1a** ^1H - ^1H NOESY is shown in magenta (top-left panel). The NOESY peak indicated by grey lines corresponds to an intermolecular NOE between the aromatic CH of **HA** and the methoxy group of **1a** and derives from resonances only observable in the triple catalyst-acid-imine complex. NMR acquired in CD_2Cl_2 at 293 K.

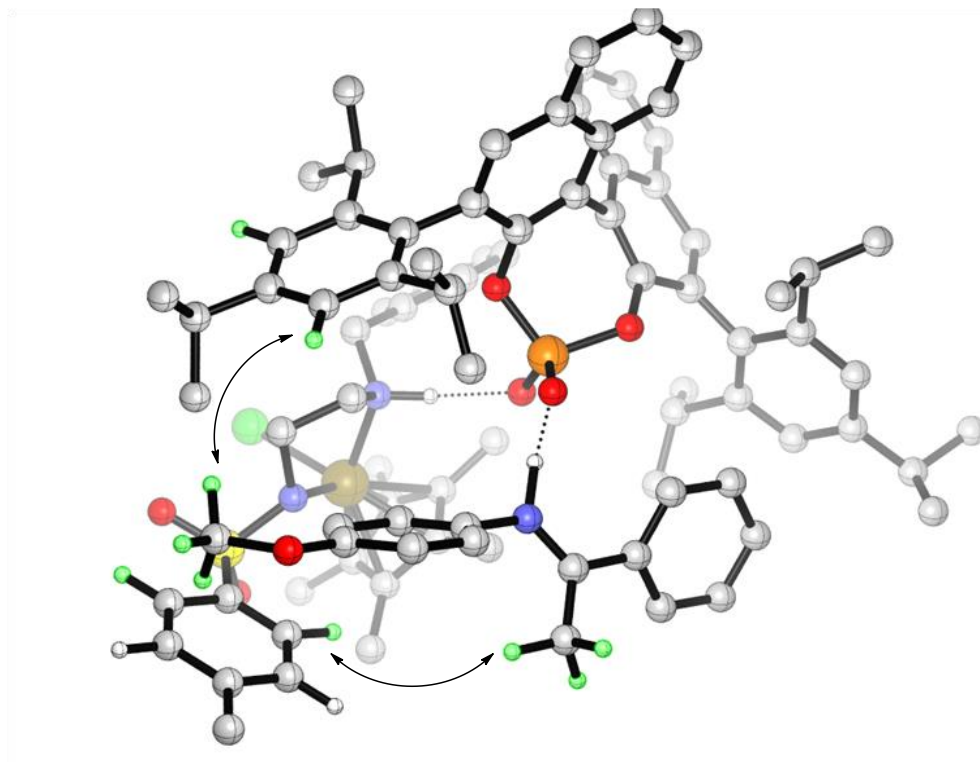


Figure 3.10: DFT/PM6-modeled structure formed by *trans*- $R_{Ir}S_N-C$, $1a^+$ and A^- , showing intramolecular NOEs used to constrain the modelling and indicated by arrows between highlighted hydrogens (light green). Grey = C, red = O, blue = N, green = Cl, yellow = S, gold = Ir, white = H.

The optimisation led to four minimised structures for each of the four configurations of **C**. From these four structures two ternary structures were consistent with the NOE data (Figure 3.11), the complex $[R_{Ir}S_N-C][1a^+][A^-]$ (-2.7 kcal/mol, all energies relative to $[S_{Ir}R_N-C][1a^+][A^-]$) incorporating *trans*- $R_{Ir}S_N-C$ (Figure 3.11 a,b), and a lower energy *cis* analogue $[S_{Ir}S_N-C][1a^+][A^-]$ (-5.7 kcal/mol) (Figure 3.11 d,e). In both structures, a hydrogen bond exists between the NH proton of $1a^+$ and an oxygen atom of the phosphate, the O---H distances being similar at 1.41 Å and 1.48 Å, respectively. The other phosphate oxygen hydrogen-bonds with the NH proton of **C**; however, the O---H distance

is significantly shorter in the *trans* complex, 2.03 Å vs. 2.45 Å, indicating a weaker hydrogen bond in the *cis* analogue and thus explaining why hydrogen bonding with the *cis* hydride **B** was not observed.

Significantly, in the *trans*-**C** derived complex $[R_{Ir}S_N\text{-}\mathbf{C}][\mathbf{1a}^+][\mathbf{A}^-]$, the chloride faces away from the hydrogen bonded $\mathbf{1a}^+$ (Figure 3.11 a,b), whereas in the *cis* analogue the chlorine atom faces the *re*-face of $\mathbf{1a}^+$ with a Cl and C (C=N) separation of 4.36 Å (Figure 3.11 d,e), which would afford the observed *S* configured amine if the chloride of **C** was replaced with a hydride, lending support to the NMR study in the previous chapter using the hydride **B**.

In addition to the hydrogen bonding, a range of CH- π interactions are evident in both complexes.²³ The main difference between the two ternary complexes is seen in the *cis*-**C**-derived $[S_{Ir}S_N\text{-}\mathbf{C}][\mathbf{1a}^+][\mathbf{A}^-]$, which exhibits favorable CH- π interactions, ranging 2.8-3.2 Å, between the CH₂ groups on the backbone of **C** and the benzyl phenyl ring of **C**, and between the former and the phenyl group of $\mathbf{1a}^+$ (Figure 3.11 f); these interactions are absent in the *trans* analogue, accounting for the higher stability of the complex derived from *cis*- $S_{Ir}S_N\text{-}\mathbf{C}$ (Figure 3.11 c vs f).

The results obtained with the model chloride complex **C** supports the notion that a ternary complex is formed in the catalysis and is responsible for enantioselective hydride transfer, and further suggest that out of the four isomeric hydrides **D**, it is the minor *cis*- $S_{Ir}S_N\text{-}\mathbf{B}$ isomer that forms the productive ternary complex with the phosphate and an iminium ion, through which the imino bond is reduced. The phosphate binds to both *cis*- $S_{Ir}S_N\text{-}\mathbf{B}$ and $\mathbf{1a}^+$ through hydrogen bonding and CH- π interactions, allowing the hydride to

add only to the *re*-face of the imino bond. These interactions and the resulting ternary complex are proposed to be the key feature of the transition state of hydride transfer in the catalysis (Figure 3.11 g), which permits highly effective chirality transfer, but at a much slower rate of hydride transfer than in hydrogenation using non-hydrogen-bonding counteranions.

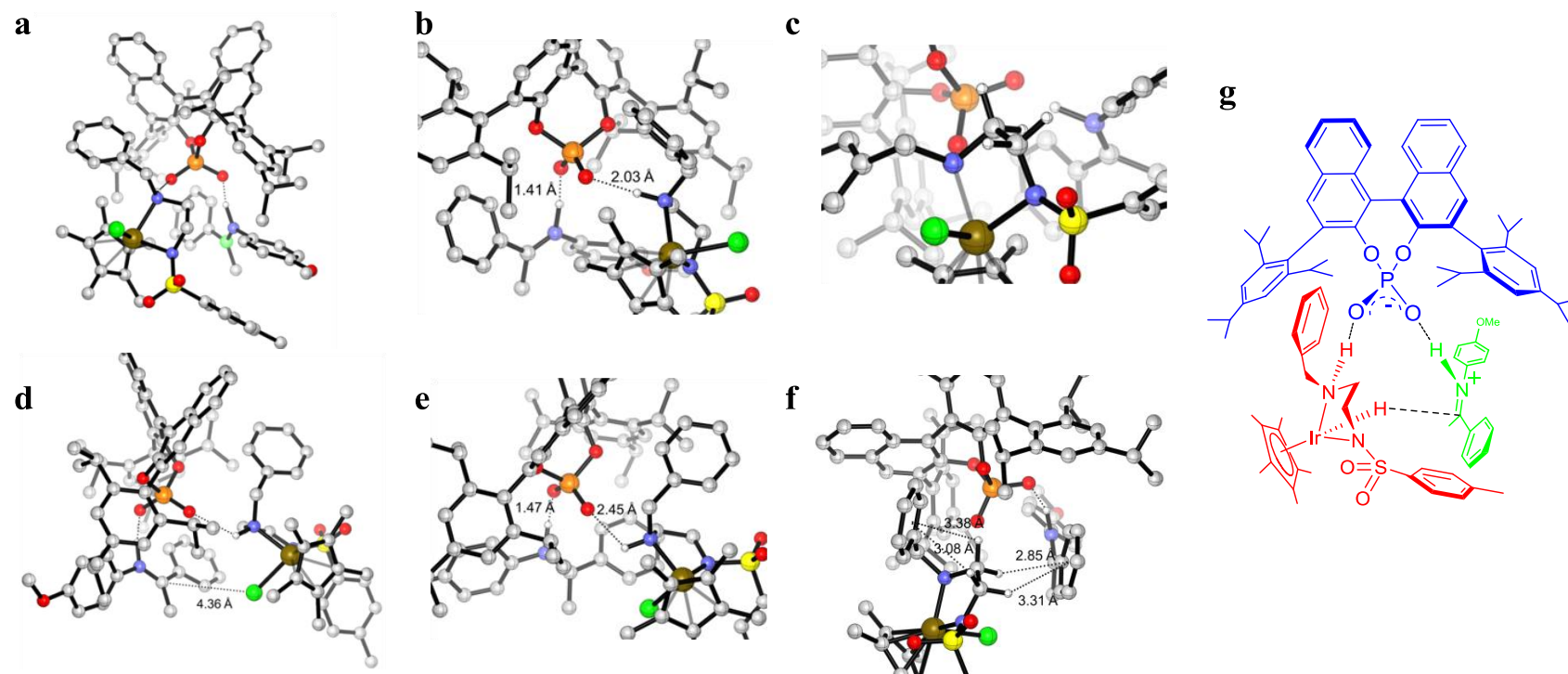


Figure 3.11: Modeled structures of ternary complexes. a and b: $[R_{Ir}S_N-C][1a^+][A^-]$ (-2.7 kcal/mol), arising from *trans*- $R_{Ir}S_N-C$, $1a^+$ and A^- , which fits NOE data; c: expansion of $[R_{Ir}S_N-C][1a^+][A^-]$ showing lack of CH- π interactions; d and e: $[S_{Ir}S_N-C][1a^+][A^-]$ (-5.7 kcal/mol), arising from *cis*- $S_{Ir}S_N-C$, $1a^+$ and A^- , which fits NOE data; f: expansion of *cis*- $[S_{Ir}S_N-C][1a^+][A^-]$ to show CH- π interactions; g: Schematic representation of the presumed transition state of hydride transfer in asymmetric imine hydrogenation with the achiral-chiral catalysts **C** and **HA**. Grey = C, red = O, blue = N, green = Cl, yellow = S, gold = Ir, white = H.

3.2.5 Diffusion ordered spectroscopy (DOSY) of the tertiary structure

PFGSE measurements were used to further probe interactions between the components. The diffusion constants calculated from the resulting ^1H DOSY NMR spectra could be related to the hydrodynamic radii, r_{H} , of a molecule by use of the Stokes-Einstein equation (Eq 1), where η is the solution viscosity and r_{H} equals the hydrodynamic radius of the diffusing particles assuming a spherical shape. This gives another method to help prove the existence of the interactions and the previously calculated structures could be compared directly with the r_{H} .

$$D = (kT)/(6\pi\eta r_{\text{H}}) \quad (1)$$

^1H DOSY spectra of the individual components showed in CD_2Cl_2 the expected difference in mobility, with **HA** having the slower diffusion constant (Figure 3.12 & Table 3.1). The calculated r_{H} show in general good agreement with the computational calculated radii, with a small difference noted for **HA**. This difference is above the uncertainty of the measurement ($\pm 9\%$, based on the reproducibility of dichloromethane) and can be attributed to possible self-aggregation and the assumption of a spherical shape in **HA**. From modelling studies **HA** can be seen to possess a large free cavity with a non-spherical shape. **HA** also possesses the ability to aggregate through hydrogen bonding and the larger hydrodynamic radii may be a product of this interaction.

Table 3.1: Diffusion constants and hydrodynamic radii for **HA**, **C** and **1b**^a

Entry	Diffusion Constant (m ² /s)	Hydrodynamic Radius (Å)	Computational Calculated Radius (Å)
CH ₂ Cl ₂	2.94 x 10 ⁻⁹	1.71	1.80
1b	1.46 x 10 ⁻⁹	3.44	4.04
HA	6.51 x 10 ⁻¹⁰	7.71	5.80
C	1.01 x 10 ⁻⁹	5.00	4.90

^aThe NMR were carried out in 0.7 mL of CD₂Cl₂, with a concentration of 20 mM for each compound. Computational calculated radius determined from the total volume of the optimised structure at a DFT level of theory.

Upon mixing of equimolar amounts of **1b** and **HA**, it can be seen that **1b** is more mobile than the **1b** in the presence of **HA**, indicating an interaction (Figure 3.13, b.).²⁴ The resonances of the imine are also changed with respect to the free imine (**1b**) indicating a new imine environment.

Free acid **HA** is also more mobile than **HA** in the presence of **1b**, but there is no change greater than the uncertainty of the measurement seen in the acid (**HA**) diffusion (Figure 3.13, c. and Table 3.2). However, from the computational model it is predicted that the imine sits in a cavity within the acid; therefore a large change in the diffusion constant and hydrodynamic radius is expected for the imine but not for the acid.

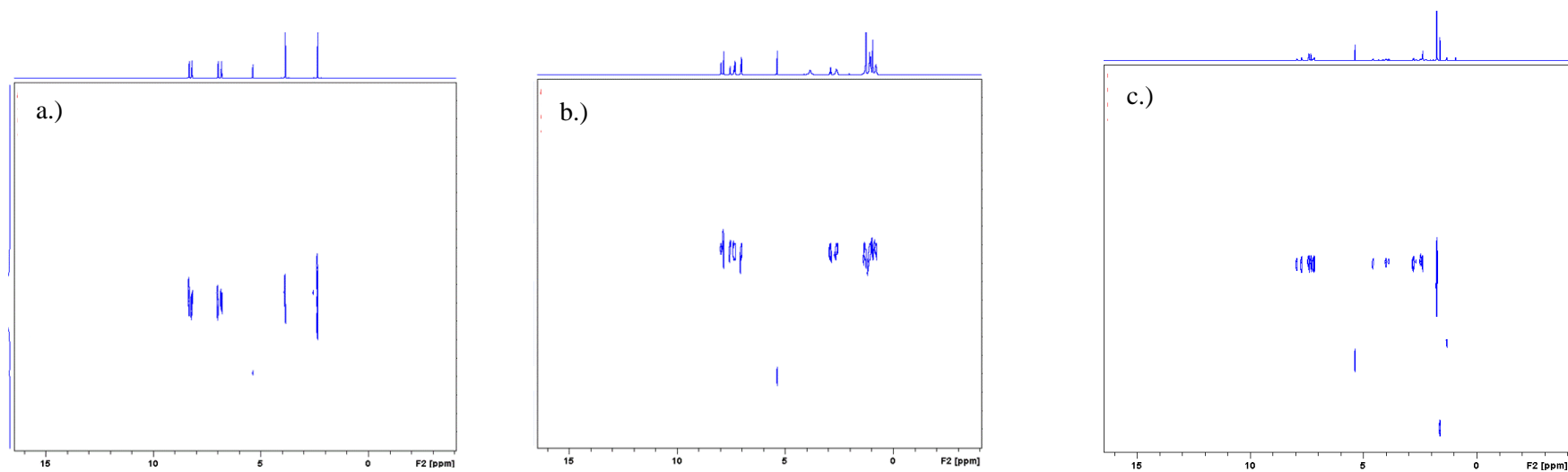


Figure 3.12: a.) ^1H DOSY spectra of **1b**; b.) ^1H DOSY spectra of **HA**; c.) ^1H DOSY spectra of **C**.

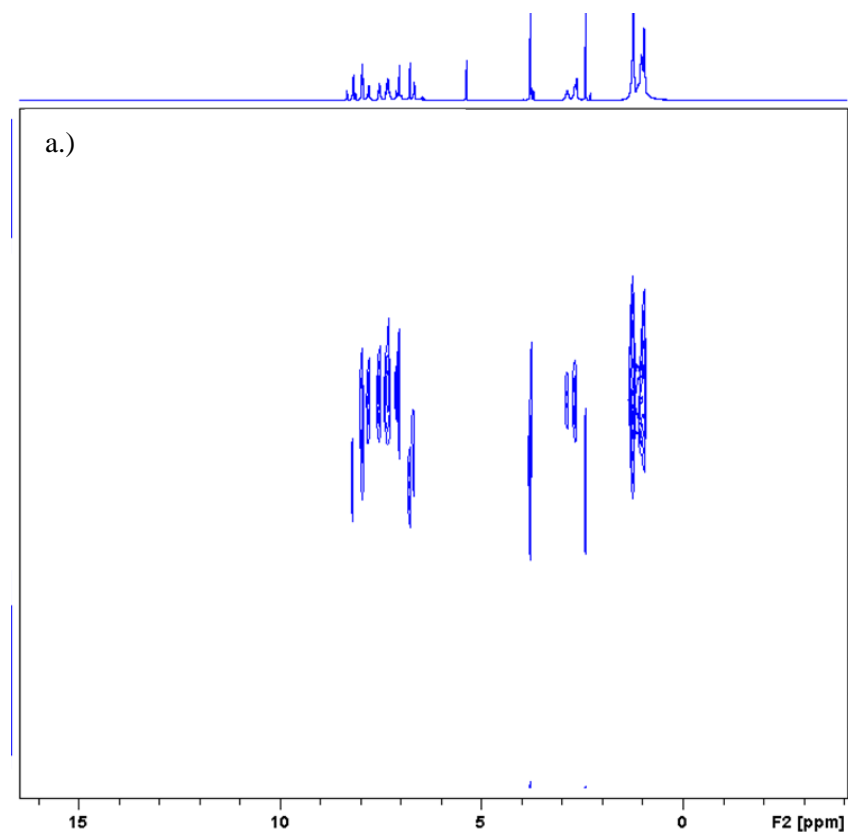
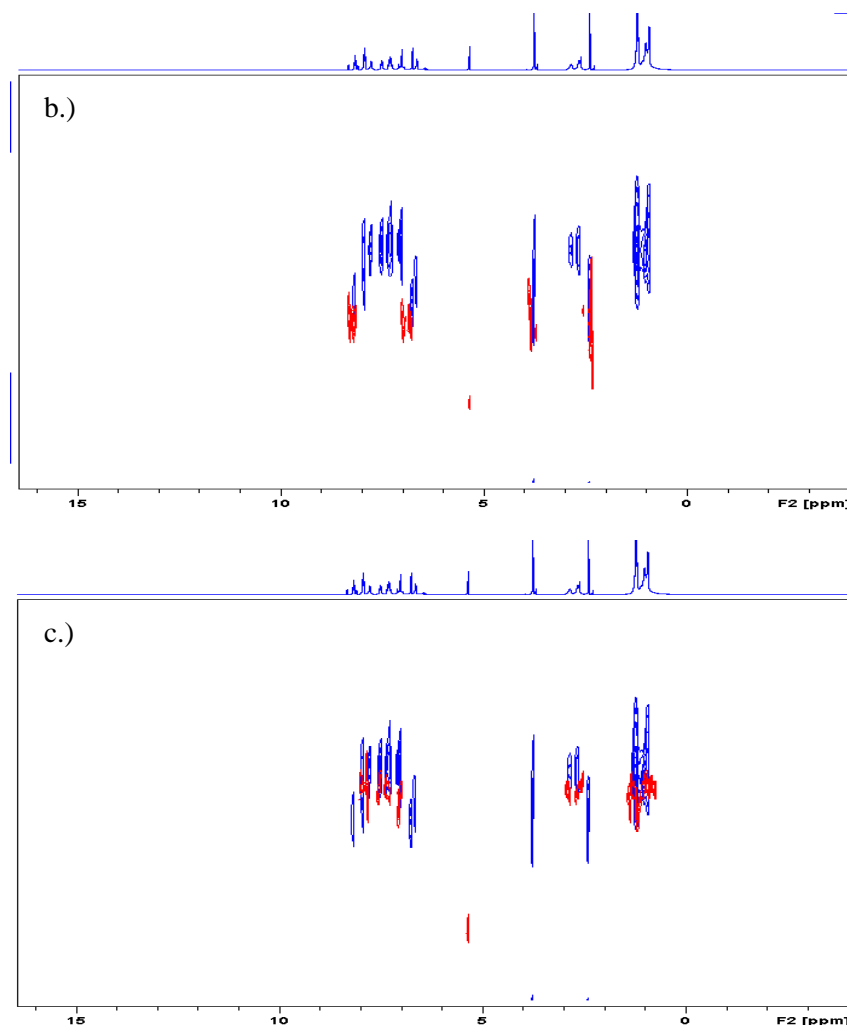


Figure 3.13: a.) ^1H DOSY spectra of **1b** + **HA** (1:1 molar ratio); b.) ^1H DOSY spectra of **1b** + **HA** (blue) compared to free **1b** (red); c.) ^1H DOSY spectra of **1b** + **HA** (blue) compared to free **HA** (red).



Examination of the hydrodynamic radii shows a good agreement between the calculated radii for the free and bound imine but larger radii for the free and bound acid. This again can be explained by the assumption of a spherical shape and possible aggregation discussed earlier.

Table 3.2: Diffusion constants and hydrodynamic radii for **1b** and **HA**^a

Entry	Diffusion Constant (m ² /s)	Hydrodynamic Radius (Å)	Computational Calculated Radius (Å)
1b	1.46 x 10 ⁻⁹	3.44	4.04
HA	6.51 x 10 ⁻¹⁰	7.71	5.80
1b (HA present)	8.34 x 10 ⁻¹⁰	6.03	6.36
HA (1b present)	6.55 x 10 ⁻¹⁰	7.67	6.36

^aThe NMR were carried out in 0.7 mL of CD₂Cl₂, with a concentration of 20 mM for each compound. Computational calculated radius determined from the total volume of the optimised structure at a DFT level of theory.

The previous chapter demonstrated that the combination of **1b** and **B** was unreactive in the absence of **HA**. The ¹H DOSY for this combination reaffirms this lack of interaction between metal complex and substrate (Figure 3.14). There is no change in either the chemical shift or diffusion constant for **1b** or **C**. With the peaks showing no change in chemical shift compared to the free components in the spectra, no interaction is suggested.

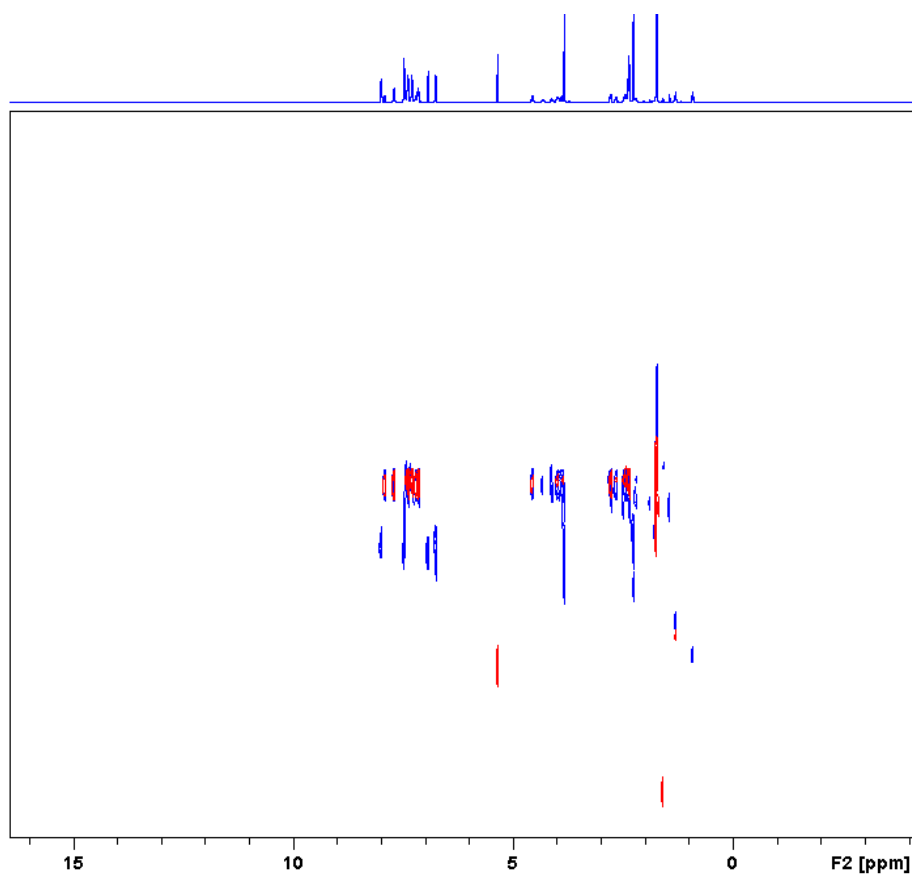


Figure 3.14: DOSY spectra of **1b** + **C** (blue)(1:1 molar ratio) compared to free **C** (red).

Work earlier in the chapter showed hydrogen bonding and NOE signals between **C** and **HA** and this is further confirmed when the diffusion is examined. There is a definite slowing of **C** and for **HA** a change no greater than the uncertainty of the measurement is observed (Figure 3.15 b-c.).

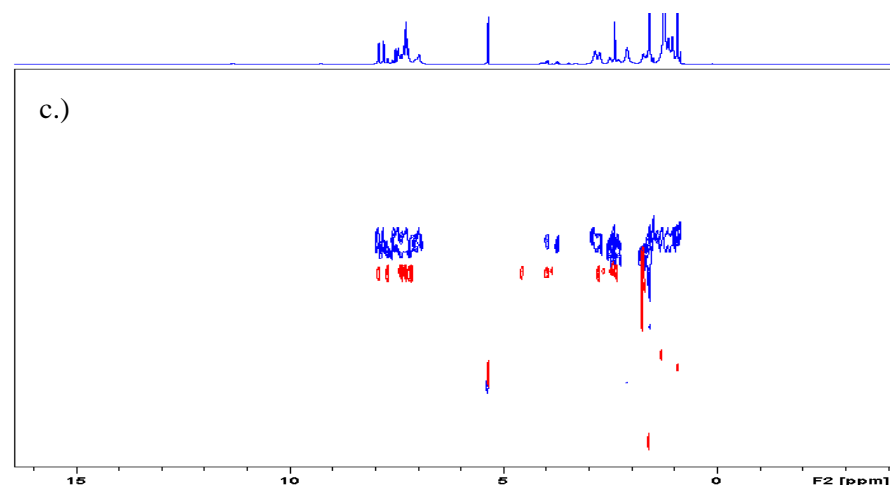
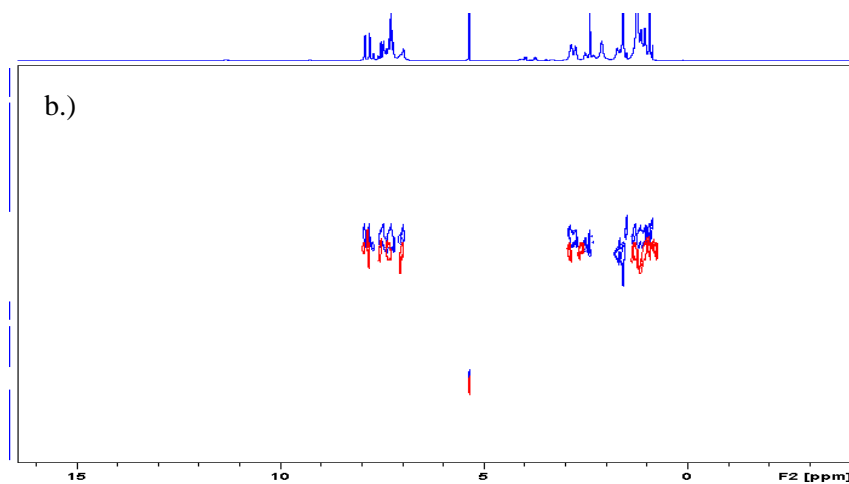
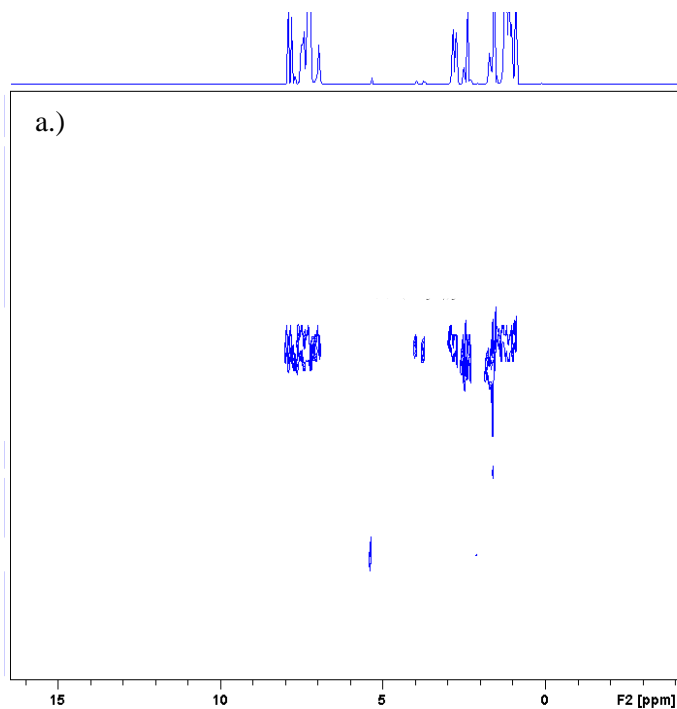


Figure 3.15: a.) DOSY spectra of **HA** + **C** (1:1 molar ratio); b.) DOSY spectra of **HA** + **C** (blue) compared to free **C** (red); c.) DOSY spectra of **HA** + **C** (1:1 molar ratio)(blue) compared to free **HA** (red).

A good agreement between the calculated and observed hydrodynamic radii is again observed (Table 3.3). As discussed previously the larger observed **HA** hydrodynamic radii compared to the computational calculated is likely due to the non-spherical shape of **HA** or aggregation. The presence of hydrogen bonding in the 1D ^1H NMR coupled with the observed slowing of **C** indicates an interaction between the two components.

Table 3.3: Diffusion constants and hydrodynamic radii for **HA** and **C**^a

Entry	Diffusion Constant (m ² /s)	Hydrodynamic Radius (Å)	Computational Calculated Radius (Å)
HA	6.51 x 10 ⁻¹⁰	7.71	5.80
HA (C present)	6.91 x 10 ⁻¹⁰	7.27	6.81
C	1.01 x 10 ⁻⁹	5.00	4.90
C (HA present)	7.17 x 10 ⁻¹⁰	7.01	6.81

^aThe reaction was carried out in 0.7 mL of CD₂Cl₂, with a concentration of 20 mM for each compound. Computational calculated radius determined from the total volume of the optimised structure at a DFT level of theory.

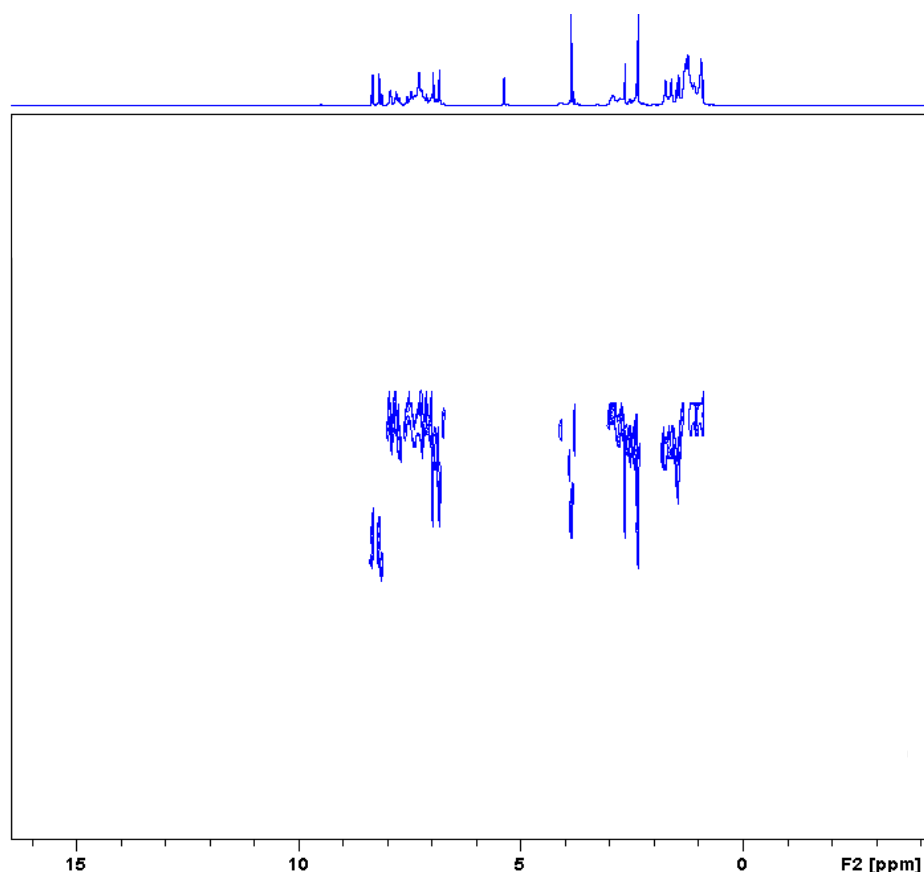


Figure 3.16: DOSY spectra of **HA** + **C** + **1b** (1:1 molar ratio).

Detecting the presence of all three components interacting together is challenging due to the number of peaks in the spectrum, which causes streaking in the ¹H DOSY NMR (Figure 3.16). The diffusion constants are calculated using either the peak intensity, or area underneath the peak, and so require a well resolved signal to achieve this.

Analysis of the ¹H DOSY NMR of **HA** + **C** + **1b** in CD₂Cl₂ allows the identification of a number of species in the sample, free **1b** (Figure 3.17, a), **C**-**HA** (Figure 3.18), and a small amount of **1b**-**HA** (Figure 3.19); but there is no free **C** (Figure 3.17, c), or free acid **HA** present (Figure 3.17, b).

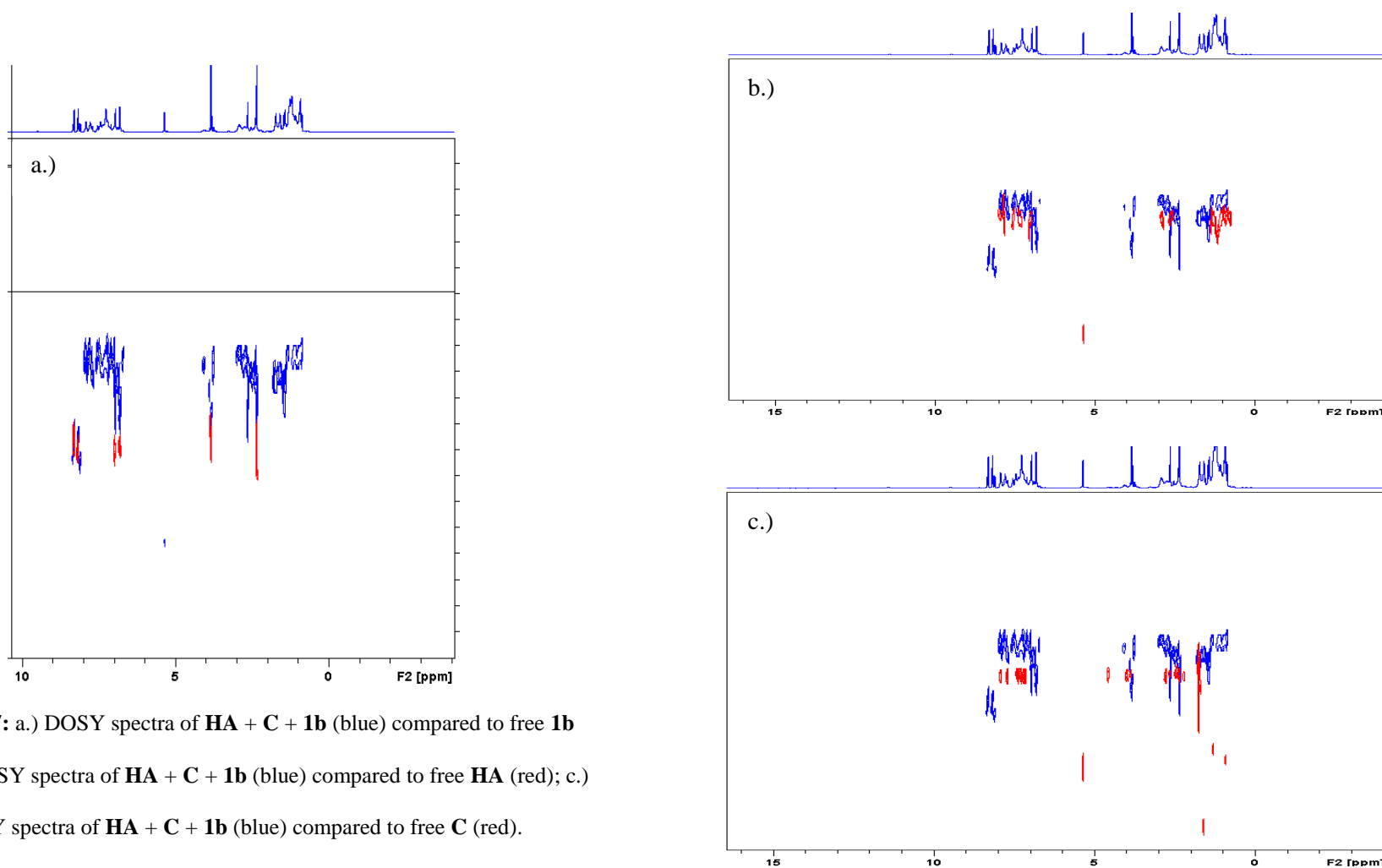


Figure 3.17: a.) DOSY spectra of **HA** + **C** + **1b** (blue) compared to free **1b** (red); b.) DOSY spectra of **HA** + **C** + **1b** (blue) compared to free **HA** (red); c.) DOSY spectra of **HA** + **C** + **1b** (blue) compared to free **C** (red).

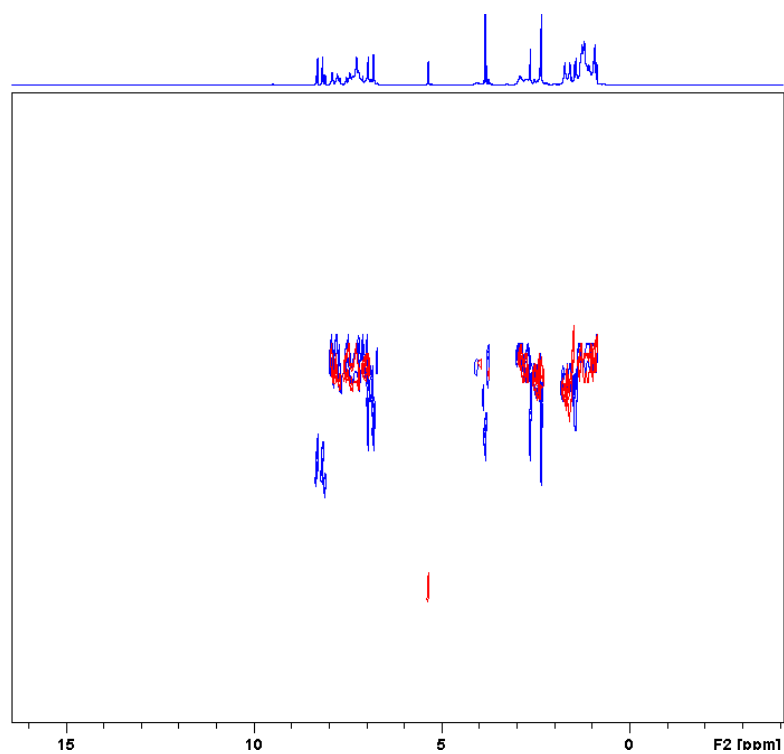


Figure 3.18: DOSY spectra of **HA** + **C** + **1b** (blue) (1:1 molar ratio) compared to **C** + **HA** (red).

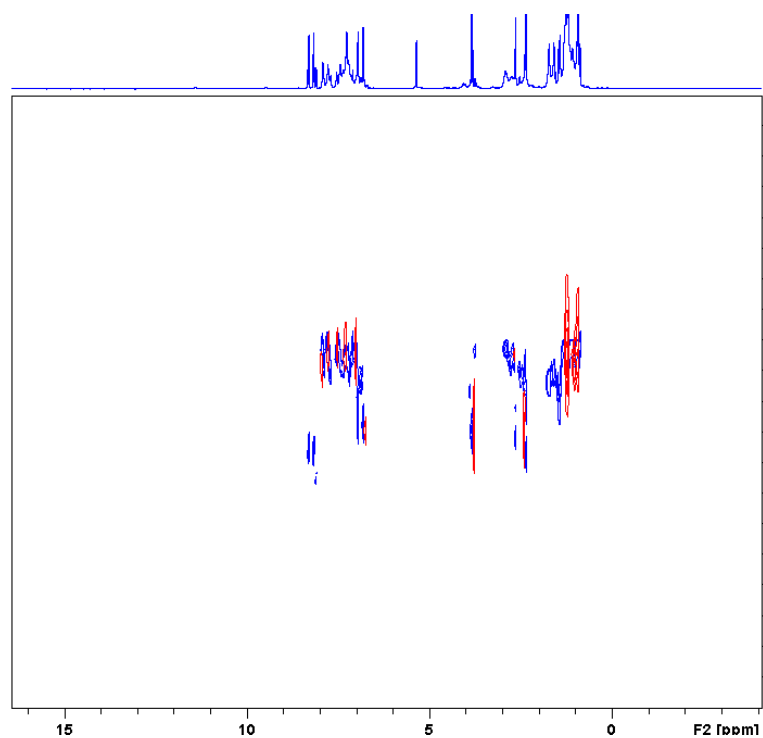


Figure 3.19: DOSY spectra of **HA** + **C** + **1b** (blue) (1:1 molar ratio) compared to **1b** + **HA** (red).

Table 3.4: Diffusion constants and hydrodynamic radii for **HA**, **C** and **1b**^a

Entry	Diffusion Constant (m ² /s)	Hydrodynamic Radius (Å)	Computational Calculated Radius (Å)
CH ₂ Cl ₂	2.94 x 10 ⁻⁹	1.71	1.80
1b	1.46 x 10 ⁻⁹	3.44	4.04
1b (HA present)	8.34 x 10 ⁻¹⁰	6.03	6.36
HA	6.51 x 10 ⁻¹⁰	7.71	5.80
HA (1b present)	6.55 x 10 ⁻¹⁰	7.67	6.36
HA (C present)	6.91 x 10 ⁻¹⁰	7.27	6.81
C	1.01 x 10 ⁻⁹	5.00	4.90
C (HA present)	7.17 x 10 ⁻¹⁰	7.01	6.81
1b , HA and C	6.37 x 10 ⁻¹⁰	7.89	7.20
Tertiary average			

^aThe NMR were carried out in 0.7 mL of CD₂Cl₂, with a concentration of 20 mM for each compound. Computational calculated radius determined from the total volume of the optimised structure at a DFT level of theory.

Calculating the diffusion constant for a range of peaks (δ 8.01-7.07 ppm 1.85-0.81 ppm) without the interference of the free **1b** gives a diffusion constant of $6.371 \times 10^{-10} \text{ m}^2/\text{s}$ (Table 3.4). The associated hydrodynamic radius (7.89 Å) compares well with the calculated computational hydrodynamic radius of **HA** + **C** + **1b** (7.20 Å), giving evidence for a tertiary structure and further confidence in the calculated structures.

Extracting a range of the 32 recorded 1D ¹H NMR spectra from the ¹H DOSY NMR shows the decay of the signals as a function of the diffusion. The

free **1b** aromatic peaks (δ 8.15-8.3 ppm and 6.8-6.95 ppm) can be seen to decay more rapidly than the other aromatic peaks. The remaining peaks decay at very similar rate in all regions of the spectrum (Figure 3.20). This coupled with the good agreement between the observed and calculated hydrodynamic radii give evidence of a tertiary structure. When the NOE signals between all three components are also taken into consideration there is solid evidence for the existence of a tertiary structure.

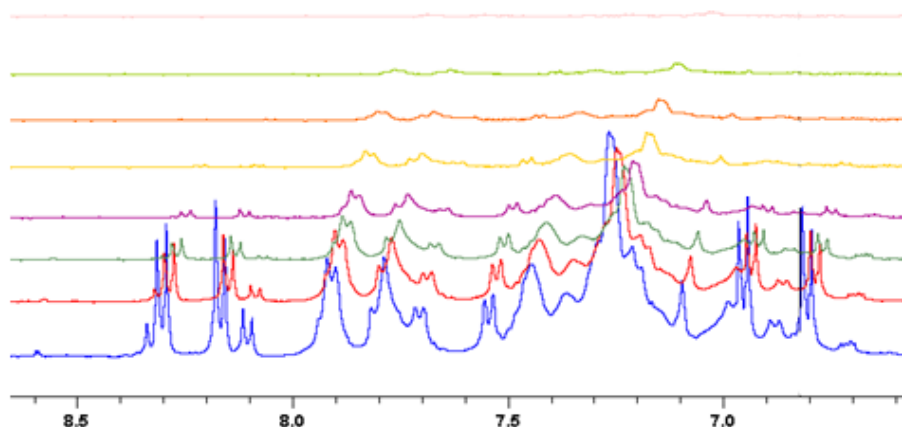


Figure 3.20: Aromatic region of **1b** + **HA** + **C** showing decay of signal as a function of the diffusion.

3.3 Conclusions and future work

This study has revealed that when an organometallic catalyst is combined with an organocatalyst to effect a reaction, it is non-covalent interactions that are likely to dictate the catalytic activity and selectivity, resembling enzymatic catalysis. The combination of hydrogen bonding and CH- π interactions allow *cis*- $S_{Ir}S_N$ -**B** to carry out the enantioselective hydride transfer. 1H DOSY NMR studies added further evidence for the supramolecular

ternary structure and showed good agreement between the predicted size of the calculated and observed radii.

Future work should concentrate on using the knowledge gained to allow for the design of future metal-organo cooperative catalysts. The key features that determine selectivity are now known and computational modelling could help locate alternative catalysts. It could be envisaged that a strategy similar to pharmacophore searching in drug design could, with the right database, allow for the location of new catalysts.

3.4 Experimental

3.4.1 Structural characterisation of tertiary structure via NMR

¹H-¹³C HSQC and ^{1b} NOESY NMR spectra of mixtures of HA, C, and 1a

NMR spectroscopy was carried out on 800MHz Bruker spectrometer equipped with a triple resonance TXI cryo probe. Spectra were obtained on natural isotope abundance samples at 293 K with a relaxation delay of 2 sec, 90° (¹H) of 10 μs. Samples used for NMR assignment were as follows; acid (**HA**) in isolation, chloride complex (**C**) in isolation, **HA-C** 1:1 mixture, **HA-1a** 1:1 mixture, **HA-C-1a** 1:1:1 mixture; all samples were prepared at a concentration of 0.1 mmol in 500 μL in deuterated DCM. 2-Dimensional homonuclear ¹H-¹H, TOCSY, COSY, NOESY and heteronuclear ¹H-¹³C HSQC, HMBC spectra were employed utilizing pulse sequences supplied by the manufacturer. Sequences were set up as follows: COSY data matrix 2048x512, 8 scans, 128 dummy scans; TOCSY data matrix 2048x512, 8 scans 128 dummy scans, 45 ms mixing time; NOESY data matrix 2048x512, 16

scans 128 dummy scans, 50 ms and 500 ms mixing times. HSQC (aliphatics) data matrix 1200x350, 48 scans, 128 dummy scans, 70 ppm ^{13}C spectral width, 35 ppm ^{13}C offset; HSQC (aromatics) data matrix 1200x192, 48 scans, 128 dummy scans, 40 ppm ^{13}C spectral width, 125 ppm ^{13}C offset; HMBC data matrix 4096x512, 48 scans, 128 dummy scans, 145 ppm ^{13}C spectral width, 72.5 ppm ^{13}C offset.

Assignment was carried out using well documented methods. Briefly, assignment of isolated acid and complex **C** was carried out using COSY, TOCSY and NOESY experiments prior to assignment of acid-catalyst, acid-imine and acid-**C**-imine samples. Heteronuclear experiments were essential in order to reduce complexity and differentiate from overlapping ^1H resonances. In instances where no COSY and TOCSY resonances were observable use of ^1H and ^{13}C chemical shift enabled prediction of assignments to be made with high-confidence (eg. Cp* and OMe assignment).

3.4.2 Pulsed field gradient spin-echo (PFGSE) measurements

The ^1H pulsed field gradient spin-echo measurements were carried out without spinning and with a steady airflow of 670 l/h to prevent convection currents from the heating coil at 295 K (± 0.1 K). The samples were dissolved in 0.7 mL of CD_2Cl_2 , with a concentration of 20 mM.

All the PGSE diffusion measurements were performed using the stimulated echo pulse sequence *dstebpgp3s* on a 400 MHz Bruker Avance spectrometer equipped with a TBI 1H/31P/BB HR probe. The pulse sequence was convection compensated and used bipolar pulses. A quadrangular gradient

pulse was used with a duration δ of 1.25 μ s, and its strength varied automatically in the course of the experiments. The gradient system was calibrated using doped water as described in the Bruker diffusion user manual. The data obtained were used to calculate the D values of the samples, according to the literature. In the ^1H -PGSE experiments, the diffusion delay, Δ , was set to 100 μ s, respectively. The number of scans was 8 per increment with a recovery delay of 2s. Typical experimental times were 30 minutes. All the spectra were acquired using 32 K points and processed with a line broadening of 1 Hz (1H).

Echo intensities and integrals were fit by non-linear regression to using the T1 processing package in TopSpin, to obtain the observed diffusion coefficients. Normally, 15-20 points were used for regression analysis, and all of the data leading to the reported D -values afforded lines whose correlation coefficients were >0.999 . The gradient strength was incremented in 3-4% steps from 1 to 99%. The hydrodynamic radii, R_{H} , were estimated using the Stokes-Einstein equation, $D = (kT)/(6\pi\eta r_{\text{H}})$, where η is the solution viscosity and r_{H} equals the hydrodynamic radius of the diffusing particles assuming a spherical shape.

The uncertainty of measurements can be judged from the reproducibility of the diffusion coefficient of dichloromethane, giving an uncertainty of $\pm 9\%$ for the diffusion coefficients.

3.4.3 Computational details

Methodology for structure optimisation utilising NOE

Initial structures were generated by use of a conformation distribution search carried out in Spartan '08 using molecular mechanics and a MMFF94 force field with default parameters.²⁵ The most popular structures which satisfied the key NOE signals previously identified were optimised using PC GAMESS.²⁶ Structure optimisations were carried out at density functional theory (DFT) level in the gas phase using the B3LYP functional.²⁷⁻³⁰ For all the optimisations the 6-31G** basis set was used for all atoms except Ir.¹³ Relativistic effects for Ir were addressed by using LANL2DZ effective core potential (ECP) together with the LANL2DZ basis set.¹³

Due to the need to model the full complexity of the system while taking into consideration of the length of time this would require using a DFT level of theory, subsequent calculations were carried out in Gaussian09 at a semi-empirical level of theory using the PM6 Hamiltonian.^{14,15} A further optimisation followed by vibrational frequency calculations were carried out to confirm the nature of the stationary point on the potential energy surface. It was necessary to insert a dummy atom placed into the middle of the Cp* ring so that the coordination remained η^5 . The Ir to dummy atom distance was constrained to a value of 1.83 Å based on the crystal structure of **C**. Energy minima were confirmed with no imaginary frequencies less than -50 cm^{-1} . All calculations were performed on the University of Liverpool linux clusters, and graphical representations were generated using chemcraft³¹ and CYLview.³²

3.5 Analytical data

All NMR data can be found attached in the supporting electronic information. All XYZ coordinates can also be found attached in the supporting electronic information.

3.6 References

- (1) Knowles, R. R.; Jacobsen, E. N. *Proc. Natl. Acad. Sci. U. S. A.* **2010**, *107*, 20678.
- (2) Shao, Z.; Zhang, H. *Chem. Soc. Rev.* **2009**, *38*, 2745.
- (3) Zhong, C.; Shi, X. *Eur. J. Org. Chem.* **2010**, 2999.
- (4) Rueping, M.; Koenigs, R. M.; Atodiressei, I. *Chem.-Eur. J.* **2010**, *16*, 9350.
- (5) Allen, A. E.; MacMillan, D. W. C. *Chem. Sci.* **2012**, *3*, 633.
- (6) Stegbauer, L.; Sladojevich, F.; Dixon, D. J. *Chem. Sci.* **2012**, *3*, 942.
- (7) Yu, Z.; Jin, W.; Jiang, Q. *Angew. Chem., Int. Ed.* **2012**, *51*, 6060.
- (8) Keeler, J. *Understanding NMR spectroscopy*; Wiley: Chichester, England ; Hoboken, NJ, 2005.
- (9) Orglmeister, E.; Burgi, T.; Mallat, T.; Baiker, A. *J. Catal.* **2005**, *232*, 137.
- (10) Jiang, Q. Z.; Ruegger, H.; Venanzi, L. M. *J. Organomet. Chem.* **1995**, *488*, 233.
- (11) Holyoak, T.; Nowak, T. *Biochemistry* **2001**, *40*, 11037.
- (12) Turner, D. L. *J. Magn. Reson., Ser B* **1995**, *108*, 137.
- (13) <https://bse.pnl.gov/bse/portal>.

- (14) Frisch, M. J.; Trucks, G. W.; Schlegel, H. B.; Scuseria, G. E.; Robb, M. A.; Cheeseman, J. R.; Scalmani, G.; Barone, V.; Mennucci, B.; Petersson, G. A.; Nakatsuji, H.; Caricato, M.; Li, X.; Hratchian, H. P.; Izmaylov, A. F.; Bloino, J.; Zheng, G.; Sonnenberg, J. L.; Hada, M.; Ehara, M.; Toyota, K.; Fukuda, R.; Hasegawa, J.; Ishida, M.; Nakajima, T.; Honda, Y.; Kitao, O.; Nakai, H.; Vreven, T.; Montgomery, J. A.; Peralta, J. E.; Ogliaro, F.; Bearpark, M.; Heyd, J. J.; Brothers, E.; Kudin, K. N.; Staroverov, V. N.; Kobayashi, R.; Normand, J.; Raghavachari, K.; Rendell, A.; Burant, J. C.; Iyengar, S. S.; Tomasi, J.; Cossi, M.; Rega, N.; Millam, J. M.; Klene, M.; Knox, J. E.; Cross, J. B.; Bakken, V.; Adamo, C.; Jaramillo, J.; Gomperts, R.; Stratmann, R. E.; Yazyev, O.; Austin, A. J.; Cammi, R.; Pomelli, C.; Ochterski, J. W.; Martin, R. L.; Morokuma, K.; Zakrzewski, V. G.; Voth, G. A.; Salvador, P.; Dannenberg, J. J.; Dapprich, S.; Daniels, A. D.; Farkas, Foresman, J. B.; Ortiz, J. V.; Cioslowski, J.; Fox, D. J. Wallingford CT, 2009.
- (15) Stewart, J. J. P. *J. Mol. Model.* **2007**, *13*, 1173.
- (16) Stejskal, E. O.; Tanner, J. E. *J. Chem. Phys.* **1965**, *42*, 288.
- (17) Pregosin, P. S.; Kumar, P. G.; Fernandez, I. *Chem. Rev.* **2005**, *105*, 2977.
- (18) Cohen, Y.; Avram, L.; Frish, L. *Angew. Chem., Int. Ed.* **2005**, *44*, 520.
- (19) Kumar, P. G. A.; Pregosin, P. S.; Goicoechea, J. M.; Whittlesey, M. K. *Organometallics* **2003**, *22*, 2956.
- (20) Uruguchi, D.; Ueki, Y.; Ooi, T. *Science* **2009**, *326*, 120.

- (21) Dydio, P.; Rubay, C.; Gadzikwa, T.; Lutz, M.; Reek, J. N. H. *J. Am. Chem. Soc.* **2011**, *133*, 17176.
- (22) Ciardi, M.; Tancini, F.; Gil-Ramirez, G.; Escudero-Adan, E. C.; Massera, C.; Dalcanale, E.; Ballester, P. *J. Am. Chem. Soc.* **2012**, *134*, 13121.
- (23) Nishio, M. *Tetrahedron* **2005**, *61*, 6923.
- (24) Storer, R. I.; Carrera, D. E.; Ni, Y.; MacMillan, D. W. *J. Am. Chem. Soc.* **2006**, *128*, 84.
- (25) <http://wavefun.com/products/spartan.html>.
- (26) <http://classic.chem.msu.su/gran/gamess/index.html> A. A. Granovsky *Firefly v7.1.G*
- (27) Becke, A. D. *J. Chem. Phys.* **1993**, *98*, 5648.
- (28) Lee, C. T.; Yang, W. T.; Parr, R. G. *Phys. Rev. B* **1988**, *37*, 785.
- (29) Vosko, S. H.; Wilk, L.; Nusair, M. *Can. J. Phys.* **1980**, *58*, 1200.
- (30) Stephens, P. J.; Devlin, F. J.; Chabalowski, C. F.; Frisch, M. J. *J. Phys. Chem.* **1994**, *98*, 11623.
- (31) <http://www.chemcraftprog.com>.
- (32) <http://www.cylview.org> CYLview *1.0b*; C. Y. Legault, **2009**.

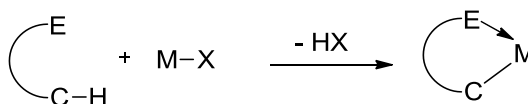
Chapter 4

Computational Studies of the effect of ligand conjugation on the activity of cyclometallated iridium (III) complexes

4.1 Introduction

Work in the previous chapters has focused on mechanistic studies of cooperative catalytic systems. This chapter centres on a range of iridium (III) cyclometallated catalysts and how the nature of conjugation present in the ligand affects the reactivity in a variety of hydrogen transfer reactions.

Cyclometallation was a term introduced in 1973 by Trofimenko¹ and can be defined as “an organic ligand undergoing intramolecular metallation to form a metal-carbon σ bond”.² Classically in a cyclometallation, coordination of the ligand to the metal forms a dative bond involving a heteroatom such as nitrogen. C-H activation then follows giving rise to the covalent metal-carbon bond with elimination of a basic leaving group as HX (Scheme 4.1). The metallacycles are usually regioselectively formed and are five-membered as opposed to the less stable four or six membered rings.



Scheme 4.1: General scheme for cyclometallation, E= Heteroatom, M= Metal.

Some of the first examples of cyclometallated complexes were reported by Cope and Siekman in 1965. They reacted azobenzene with K_2PtCl_2 and PdCl_2 to form cyclometallated Pt and Pd dimers **1**.³ Further early examples were reported including rhodium phenyl-phosphane **2** and ruthenium phenyl-phosphite **3** complexes (Figure 4.1).^{4,5,6-8}

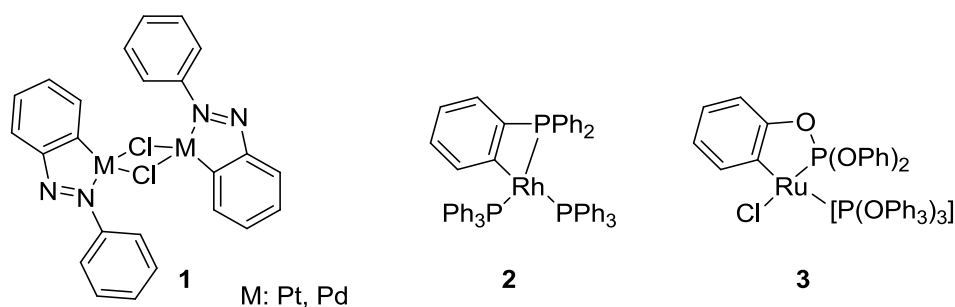
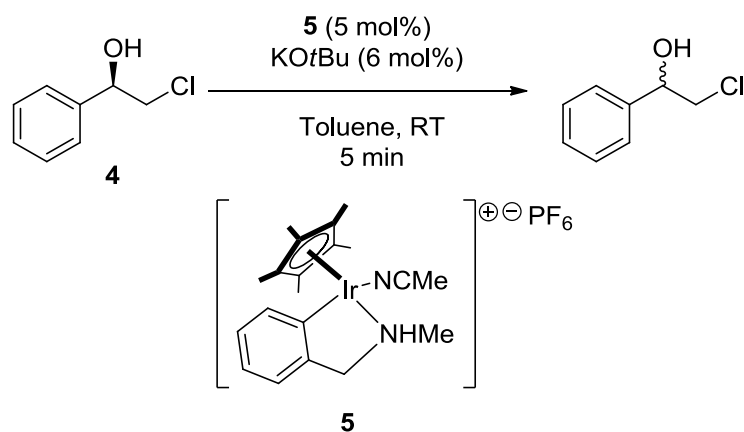


Figure 4.1: Early reported examples of cyclometallated complexes.

Since these early examples the field has seen major advancements, with cyclometallated complexes being utilised as highly active catalysts for a range of reactions. Specifically among these reactions, cyclometallated complexes have been shown to catalyse a range of novel hydrogen transfer processes, including the racemisation of amines and alcohols,⁹⁻¹¹ hydrogenations¹²⁻¹⁴ and dehydrogenation reactions.¹⁵⁻²³

Racemisation of amines and alcohols utilising cyclometallated complexes was demonstrated by de Vries.⁹ This was achieved with electron-rich iridacycles, with complex **5** containing a benzylamine ligand showing high activities for alcohols, upon activation with base (Scheme 4.2). Full racemisation could be achieved at room temperature with alcohol **4** fully

consumed in 5 minutes. The amine racemisation necessitated a change to a phenylimidazoline ligand but without the need for activation.



Scheme 4.2: Racemisation of alcohols using a cyclometallated iridium catalyst.

The first example of transfer hydrogenation using a cyclometallated metal catalyst was reported by Baratta *et al.*¹² They reduced a range of simple ketones using complex **6**, containing a P[^]C ligand and a 2-(aminomethyl)pyridine ligand (Figure 4.2). The reaction was carried out in *i*PrOH at 82 °C and gave a very high TOF up to 63,000 h⁻¹.

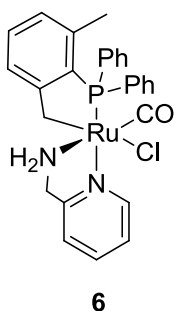


Figure 4.2: Cyclometallated ruthenium(II) complex used for transfer hydrogenation.

Sortais *et al* investigated the asymmetric transfer hydrogenation of acetophenone using ruthenacycles obtained by cyclometalation of enantiopure aromatic primary or secondary amines.¹³ The ability to prepare the cyclometallated catalyst *in situ* allowed for the use of high throughput techniques. Of the ligands tested using this method, **7** gave the best results with 99% yield and 80% ee in *i*PrOH at room temperature (Figure 4.3).

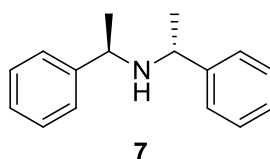
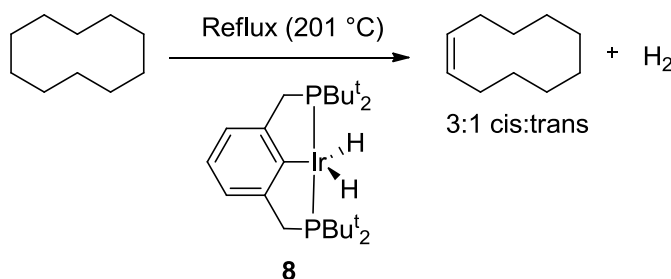


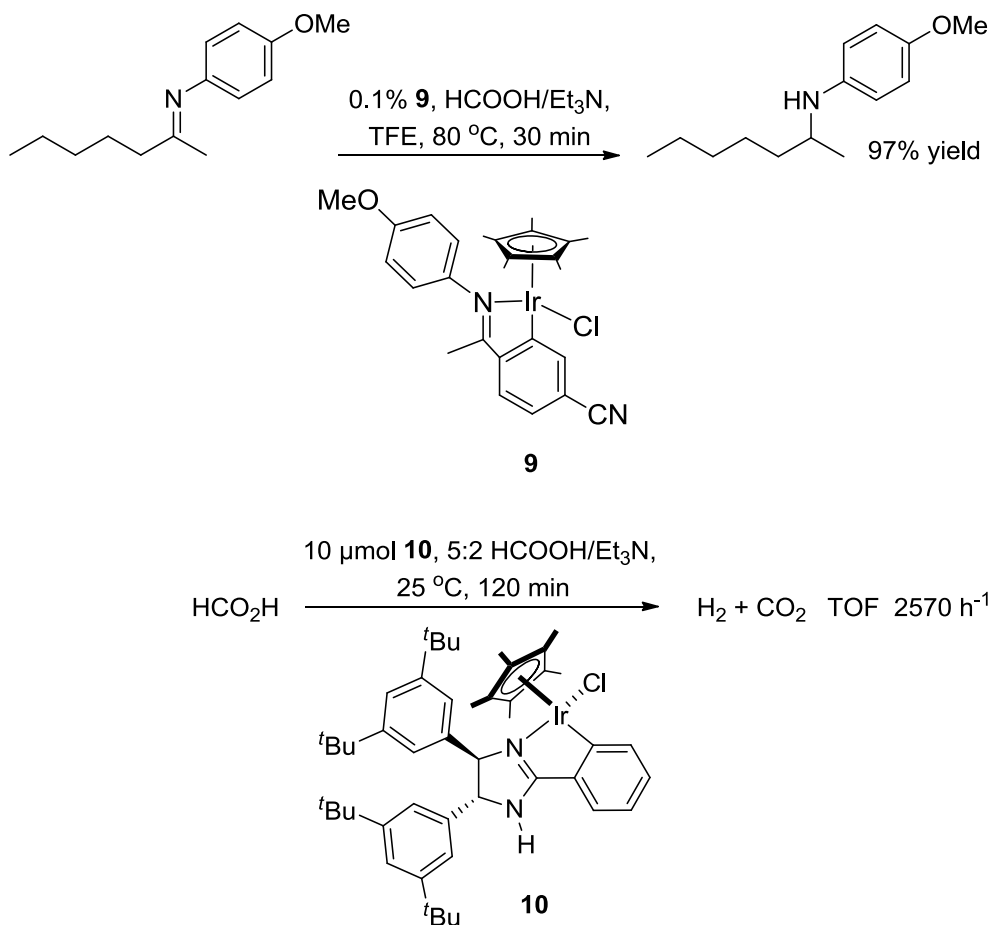
Figure 4.3: (*R*)-bis((*R*)-1-phenylethyl)amine ligand.

Dehydrogenations catalysed by cyclometallated complexes have also been demonstrated. Gupta and co-workers showed that the iridium P-C-P pincer complex could catalyse the dehydrogenation of a range of cycloalkanes to alkenes and arenes.^{17,18} Dehydrogenation of cyclodecane at 201 °C yields 170 and 360 turnovers after 4 and 24 h, respectively (Scheme 4.3).²⁰ The reaction was also successfully extended to alkylbenzenes and cyclic ethers but required the presence of the hydrogen acceptor, tertbutylethylene.¹⁹



Scheme 4.3: Dehydrogenation of cyclodecane with an iridium P^CP pincer complex.

Recent work in our group has shown that cyclometallated $\text{Cp}^*\text{Ir}(\text{N}^{\wedge}\text{C})\text{Cl}$ complexes are highly active catalysts for a range of hydrogen transfer reactions, including transfer hydrogenation of imines and carbonyls, mild hydrogenations of *N*-heterocycles and acceptorless dehydrogenation reactions (Scheme 4.4).²⁴⁻³⁰



Scheme 4.4: Cyclometallated complexes for the TH of imines and the dehydrogenation of formic acid.

These studies appear to suggest that conjugation in the ligand and between the ligand and metal affects the catalytic activity. Conjugation can be viewed as the delocalisation of π electrons through bonds with a π system.³¹

Conjugated systems require there to be an unbroken arrangement of p-orbitals that align to produce a π bonding overlap along the whole system. A break in this chain or an atom that does not provide a p-orbital causes the conjugations to be broken. Thus, conjugated systems fall into two basic groups:

- An "isolated" π system existing between only a single pair of adjacent atoms (e.g. $C=C$).
- An "extended" π system existing over a longer series of atoms allowing for extended stability and reactivity (e.g. $C=C-C=C$ or $C=C-C=O$).

This overlapping of the p-orbitals in an extended system allows for the delocalisation of the electrons throughout a molecule and can be observed in many linear and cyclic molecules, for example benzene. The presence of conjugation gives rise to stronger sigma bonds due to the sp^2-sp^2 overlap giving single bonds more "double bond" character and conversely to longer double bonds than non-conjugated double bonds analogues. The more conjugation there is in analogous system, the closer together the highest occupied molecular orbital (HOMO) and lowest unoccupied molecular orbital (LUMO) become, therefore giving a smaller energy gap between the reactant frontier orbitals and hence an increase in reactivity. The presence of conjugation allows for extended stability and different reactivity in molecules not observable in its absence. With transition metal atoms possessing the required orbitals of appropriate energy and symmetry, conjugated systems can be present within metal complexes and this study will focus on those present in a range of cyclometalated iridium (III) complexes. A detailed understanding of how

conjugation affects the hydrogen transfer steps in the reactions is of critical importance to the development of highly active catalysts for these processes.

4.2 Results and discussion

In the course of work undertaken in the Xiao group (Tables 4.1-4) developing catalysts for the dehydrogenation of formic acid, it was noted that the activity was strongly dependent on the position of cyclometallation of the arylimidazoline ligand, with C₂ cyclometallation giving highly active catalysts and C₄ giving inactive complexes (Figure 4.4).²⁷

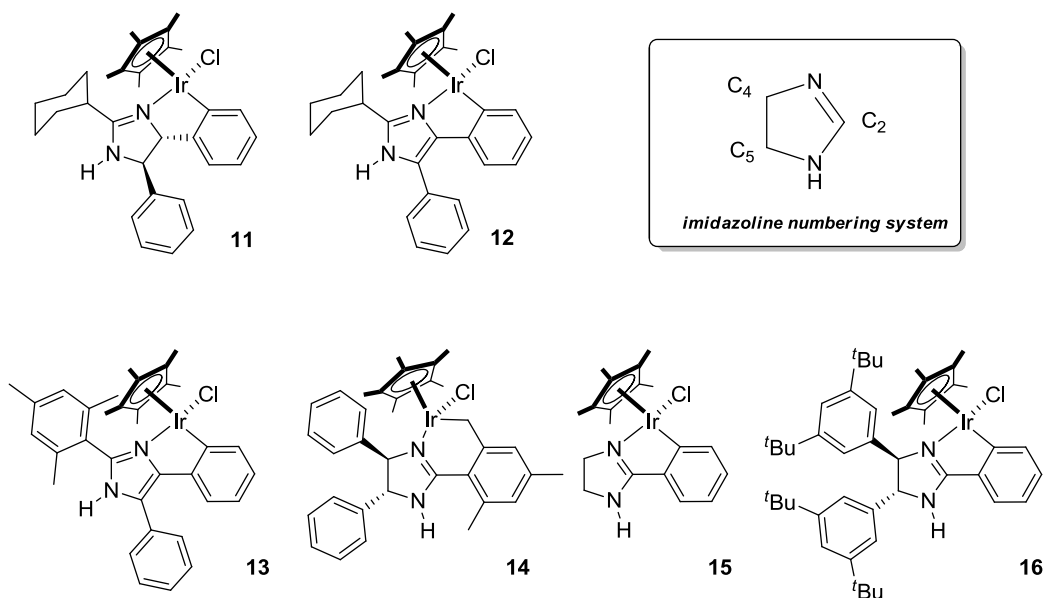


Figure 4.4: Complexes examined to investigate the level of conjugation influencing reactivity.

To investigate the factors behind the dramatic differences in activity of an array of catalysts a range of related complexes were synthesised within the Xiao group using the acetate assisted cyclometallation protocol reported by Davies and co-workers (Figure 4.4).³²⁻³⁴ Complex **11** and **12** differ in the added conjugation from an imidazoline ring in **11** to a more conjugated imidazole

ring in **12**. Complex **13** has added steric bulk with a mesityl ring in the C₂ position while the related complex **14** has the cyclometallation occurring on a methyl group on the mesityl ring as opposed to the phenyl ring. Complex **15** is fully conjugated but without the added rings of the previous complexes in contrast to the sterically congested **16** which possesses 2,5 *tert*-butyl substituted phenyl rings.

Complexes **11** and **14** lack a system capable of conjugating to the metal centre and can be described as non-conjugated but complexes **12** and **13** can be thought of as possessing a cross conjugated system. This is where there are three unsaturated groups present, two of which, although conjugated to a third unsaturated centre, are not conjugated to each other.³⁵ Complexes **15** and **16** possess the correct arrangement of bonds to allow for full conjugation to the metal centre.

Each of these complexes was tested in a range of hydrogen transfer reactions and formic acid decomposition by Dr Jonathan Barnard to assess their catalytic activity for the computational study (Tables 4.1-4.4).

Table 4.1 Hydrogenation of 1-methyl-3,4-dihydroisoquinoline^a

Entry	Complex	Solvent	Conversion (%) ^b
1	11	MeOH	N.R.
2	12	MeOH	14
3	13	MeOH	22
4	14	MeOH	N.R.
5	15	MeOH	44
6	16	MeOH	38

^aConditions: 1-methyl-3,4-dihydroisoquinoline (0.5 mmol), catalyst (1 mol%), MeOH (3 mL).

^bConversion determined by ¹H NMR of the crude reaction mixture and normalising the sum of the product and starting material integrals to 100%. N.R. = no reaction

Table 4.2 Hydrogenation of 2-methylquinoline^a

18 18a

Entry	Complex	Solvent	Conversion (%) ^b
1	11	TFE	N.R.
2	12	TFE	10
3	13	TFE	50
4	14	TFE	N.R.
5	15	TFE	50
6	16	TFE	44

^aConditions: 1-methyl-3,4-dihydroisoquinoline (0.5 mmol), catalyst (1 mol%), TFE (3 mL).

^bConversion determined by ¹H NMR of the crude reaction mixture and normalising the sum of the product and starting material integrals to 100%. N.R. = no reaction

Table 4.3 Hydrogenation of an acyclic imine^a

19 19a

Entry	Complex	Solvent	Conversion (%) ^b
1	11	MeOH	N.R.
2	12	MeOH	3
3	13	MeOH	62
4	14	MeOH	N.R.
5	15	MeOH	97
6	16	MeOH	80

^aConditions: Imine (0.5 mmol), catalyst (1 mol%), TFE (3 mL), ^bConversion determined by ¹H NMR of the crude reaction mixture and normalising the sum of the product and starting material integrals to 100%. N.R. = no reaction

Table 4.4 Decomposition of formic acid^a

$\text{H}-\text{C}(=\text{O})-\text{OH} \xrightarrow[2\text{ h, rt}]{10\ \mu\text{mol catalyst, 1.5 mL 5:2 F/T}} \text{CO}_2 + \text{H}_2$

Entry	Complex	Initial TOF h ⁻¹	Vol H ₂ (2 h) / mL	TON (2 h)
1	11	0	0	0
2	12	490	8	33
3	13	1142	40	163
4	14	0	0	0
5	15	1090	49	200
6	16	980	76.5	312

^aReactions were performed under an N₂ atmosphere with 10 μmol of catalyst precursor and 1.5 mL of 5:2 formic acid/triethylamine mixtures (F/T). Initial TOF values calculated from the volume of gas collected in the first 3 min (see the experimental section for further details).

A clear trend in reactivity can be observed for the complexes with the non-conjugated systems, **11** and **14** having no reactivity for any of the reactions tested, the cross conjugated **12** and **13** showing low to mid-range reactivity and the fully-conjugated **15** and **16** having the highest activity (Figure 4.5). This leads to clear trend in reactivity that can be thought of as: conjugated > cross-conjugated > non-conjugated complexes.

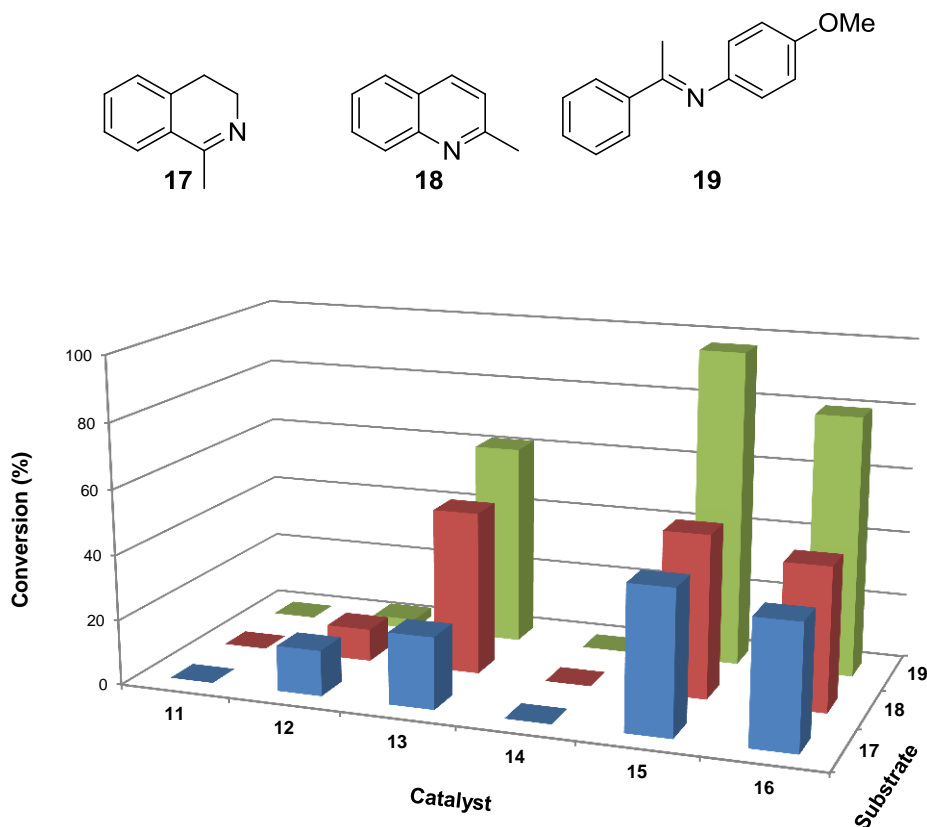
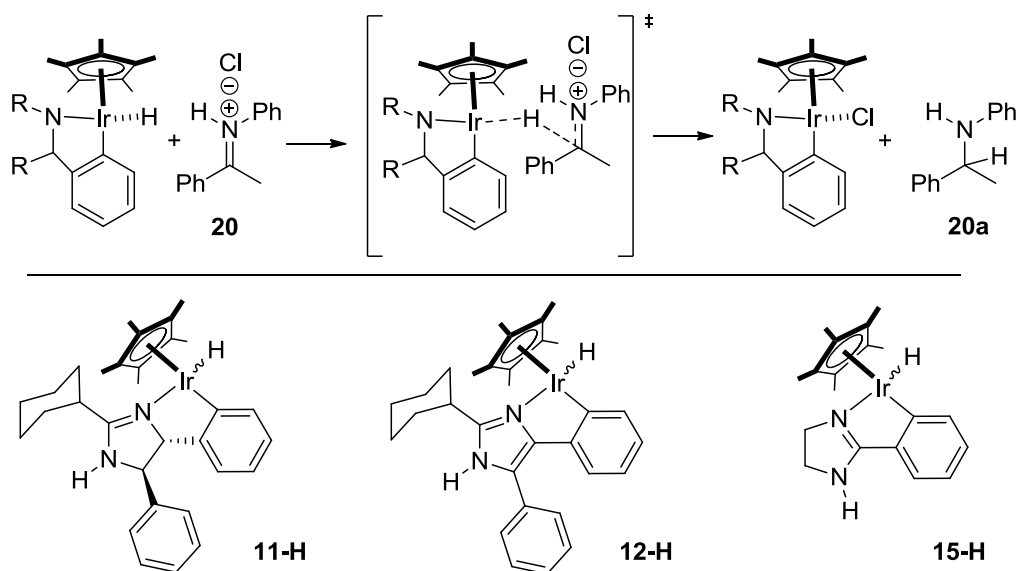


Figure 4.5: Table summarising the reactivity of complexes **11-16** for hydrogenation of substrates **17-19**.

This clear link observed in the results between the degree of conjugation and the activity of the complex was explored in much greater detail by the use of computational studies to identify the key factors that account for the changes in reactivity.

For the computational study, complexes **11-H**, **12-H**, and **15-H** were selected to be examined for the hydride transfer step of the reduction of **20**, due to the ease of formation of the hydrides in the hydrogenation reaction (Scheme 4.5). Complexes **11-H** and **12-H** have differing degrees of conjugation while having a very similar structure allowing for direct comparison of the conjugation. In contrast complex **15-H** has a fully conjugated system but without the outer rings of the other complexes. While a direct comparison to the other complexes has to take into consideration steric effects, the comparable reactivity of the fully conjugated complex **16** show that it is not a merely steric effect and there must be other underlying factors. Complex **15-H** also has much lower computational demands due to the lower number of electrons than the much larger complex **16**.



Scheme 4.5: The hydride transfer step studied and the cyclometallated Ir(III) hydride complexes investigated in this study.

Previous stoichiometric studies have shown that the reduction of imines occurs by an ionic mechanism in which a protonated imine reacts with the iridium monohydride, with no reaction occurring between the hydrides and neutral imines.²⁹ The modelling therefore looked at each of the hydride complexes delivering to a protonated imine **20** with a simple chloride counter-anion, resulting in the amine product **20a** and the corresponding chloride complex.

4.2.1 Ground state structures and energies

For each of the complexes **11-H**, **12-H** and **15-H** the ground state structures and energies were attained. Due to the rigid nature of the ligand there are a small number of rotatable bonds in the complexes (< 3). Both **12-H** and **15-H** possess one stereogenic centre at the iridium and as expected each set of enantiomers are extremely close in energy, 0.28 and 0.06 kcal/mol apart respectively (Figures 4.6-4.8). The small difference is likely due to the error associated with the calculations.

However, complex **11-H** presents a different case, as there is an in built fixed chirality present in the ligand as well as the chirality at the iridium. This leads to two diastereoisomers with differing energies of 7.03 kcal/mol. A closer examination of the structures allows for a clear indication of where this large difference arises, **11-H**-(R) and **11-H**-(S) show a change in structure from the piano stool geometry in **11-H**-(S) to a more distorted, flatter structure (lower Cp*-Ir-N-C dihedral angle 16.9° (R) vs. 83.59° (S)) in **11-H**-(R) (Figure 4.6). In **11-H**-(R) the C-H at C₄ of the imidazoline ring is in close proximity (2.56 Å (R) vs. 4.27 (S) Å) to the hydride, leading to a distortion in structure in order to

alleviate the steric hindrance. This large difference in energy leads to **11-H**-(R) being inaccessible at room temperature removing this diastereoisomer from being involved in the hydride transfer step. The transition state search can therefore discount results from this diastereoisomer.

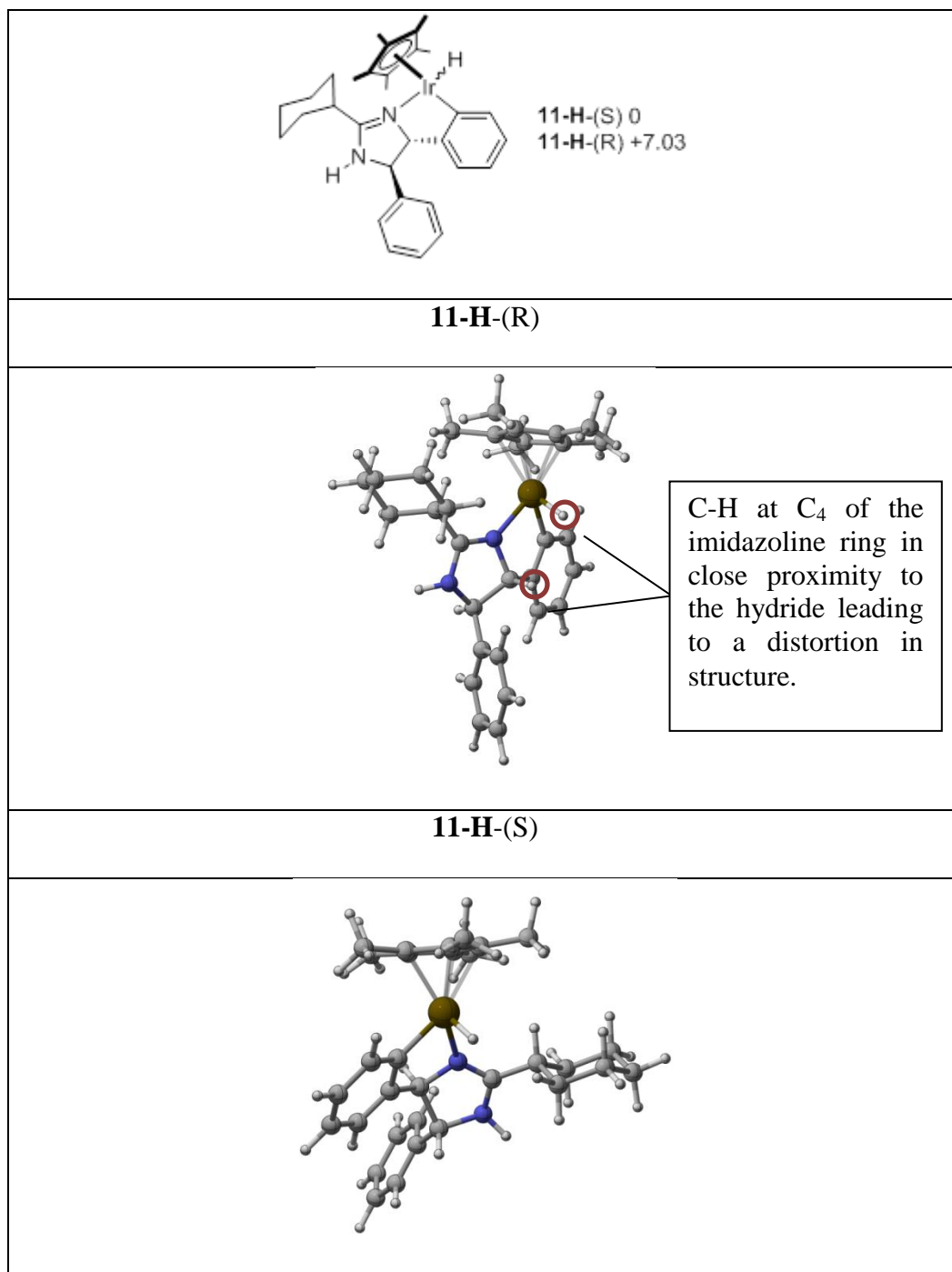


Fig. 4.6: Ground state energy's and structures for **11-H**, gold = Ir, blue = N grey = C, H= white. Ball and stick model.

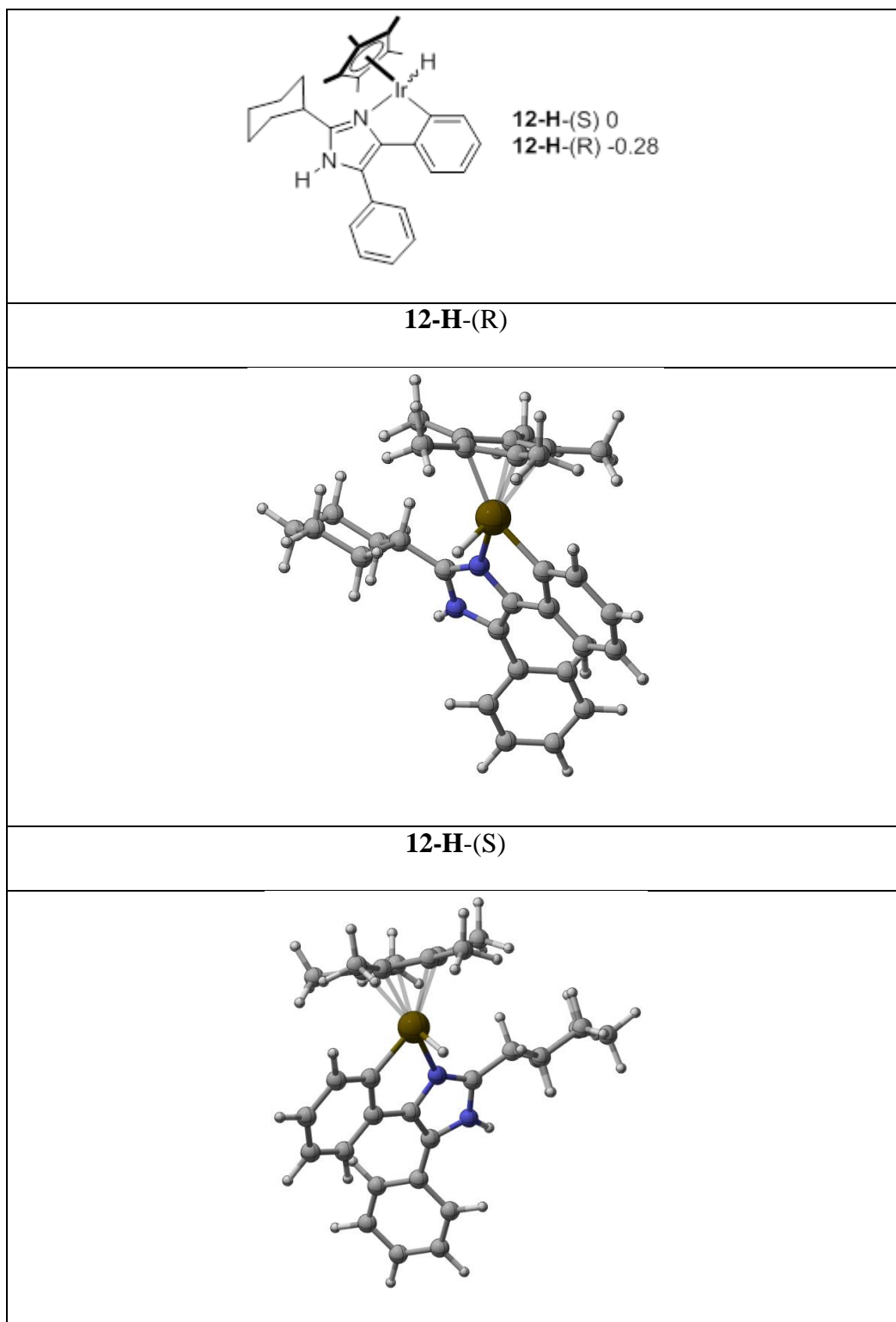


Fig. 4.7: Ground state energy's and structures for **12-H**, gold = Ir, blue = N grey = C, H= white. Ball and stick model.

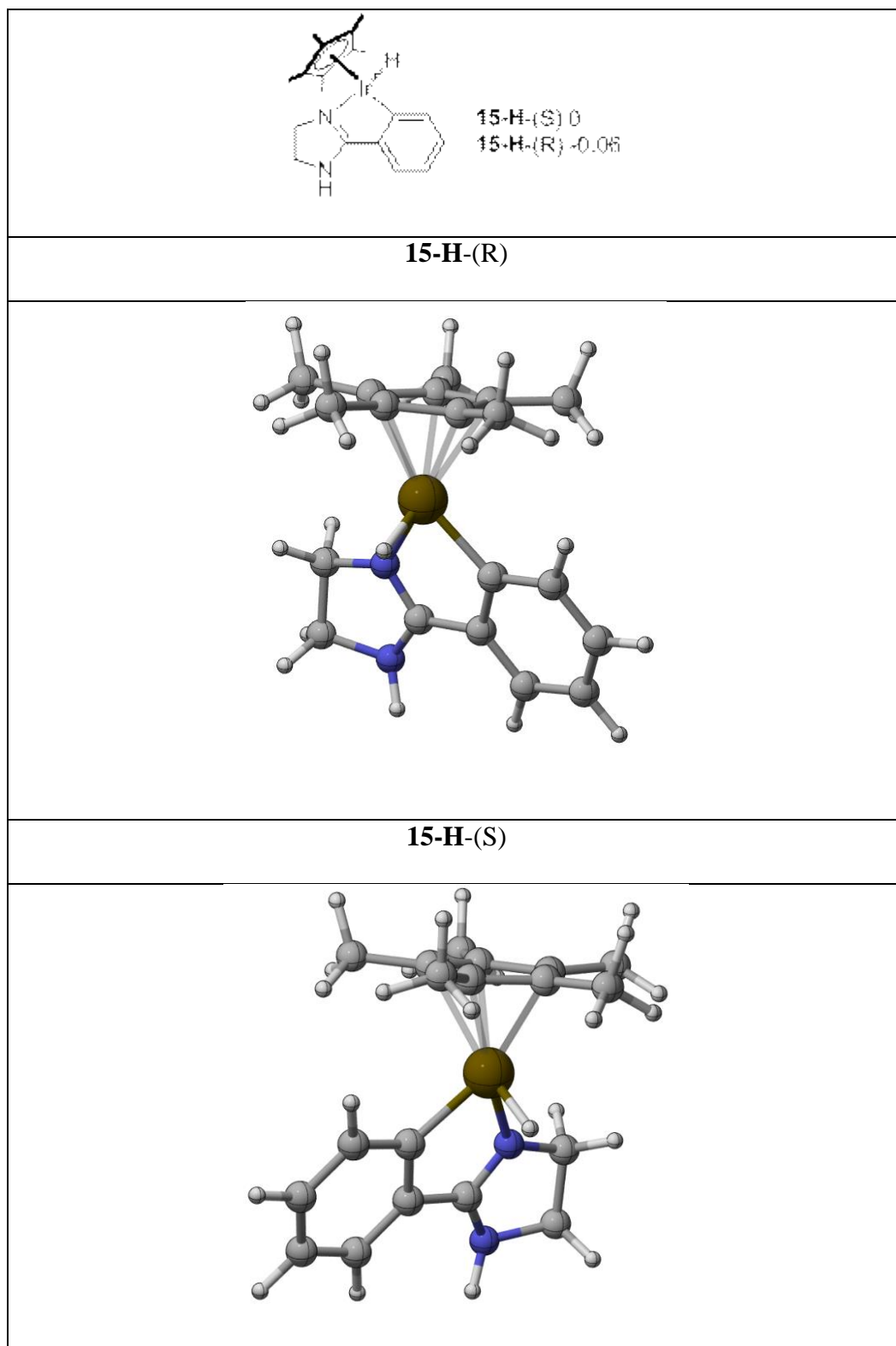


Fig. 4.8: Ground state energy's and structures for **15-H**, gold = Ir, blue = N grey = C, H= white. Ball and stick model.

4.2.2. HOMO of ground state complexes

Examination of the HOMO of each of the complexes at the ground state allowed for a qualitative indication of the degree of conjugation each possesses (Figures 4.9-4.10). A close examination of the HOMO of **11-H**-(S) shows the majority of the orbital located around the central iridium, cyclopentadienyl ring and the cyclometallated phenyl ring with a smaller amount located on the imidazoline ring at the C₂, C₄ positions and the cyclometallated N. The lack of conjugation through-out the molecule is demonstrated by the absence of the orbital being spread across the ligand with only a presence in individual locations.

The HOMO of **12-H**-(S) has much the same characteristics of **11-H**-(S) but possesses a conjugated imidazole ring and the HOMO diagram demonstrates this. There is a larger HOMO presence on this ring at the C₂ and C₅ positions and extend into the remote phenyl ring. Crucially, however, the orbital on the imidazole does not extend into the central iridium or the cyclometallated phenyl ring, showing a lack of complete conjugation through the ligand system. This helps to illustrate the cross conjugated system that is present in this complex.

In contrast to the previous two complexes, **15-H**-(S) has a HOMO that is located across the entire complex with the orbital situated over both the ligand and the iridium confirming a fully conjugated system. This information confirmed the nature of the conjugation in each complex and led onto the location of the transition states for the hydride transfer step.

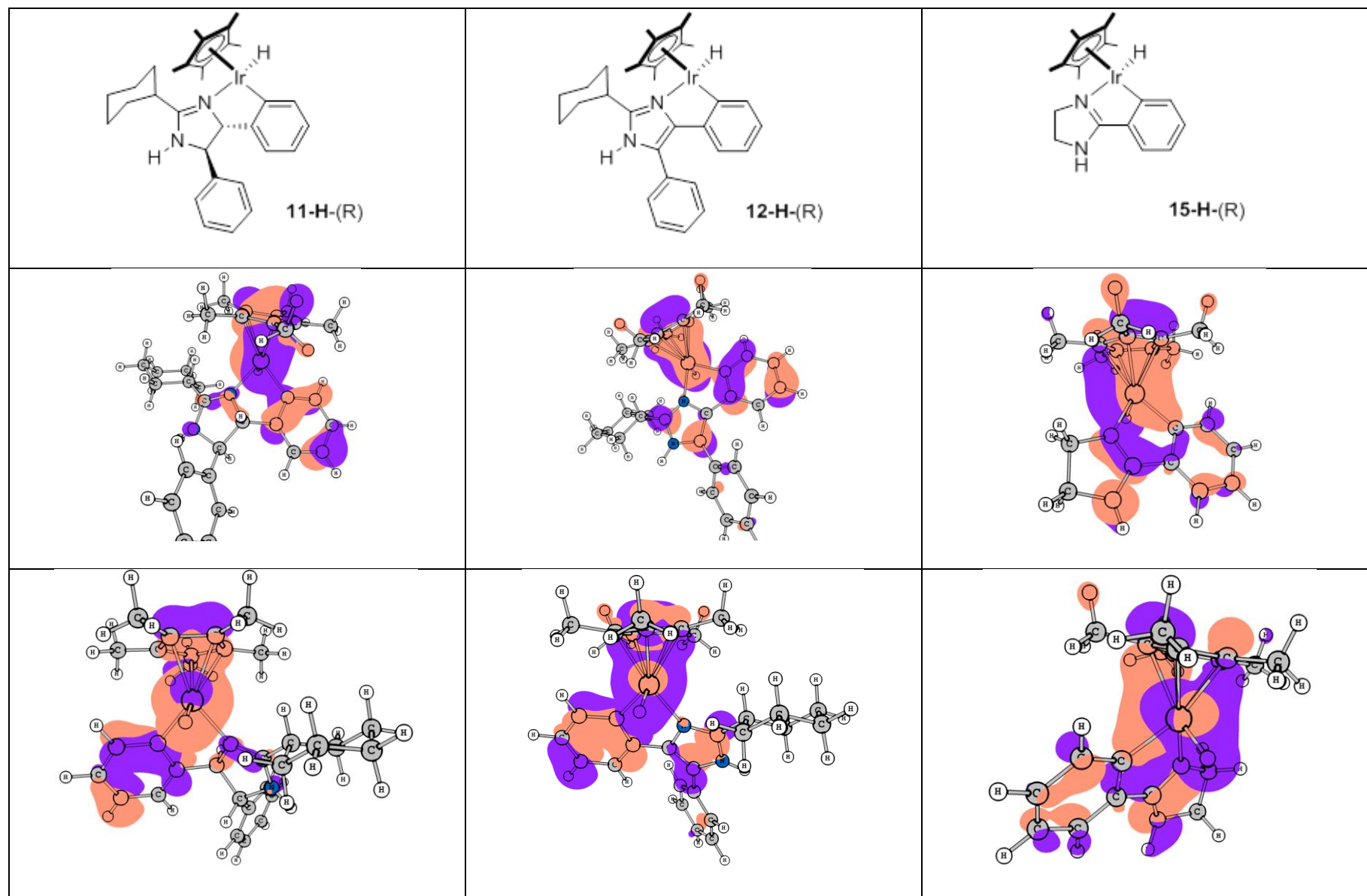


Figure 4.9: HOMO diagrams showing two orientations for the Ir-(S) configuration of each complex. The orange colour reflects a positive phase, whereas the purple colour refers to a negative phase, iso value range -0.02 – 0.02.

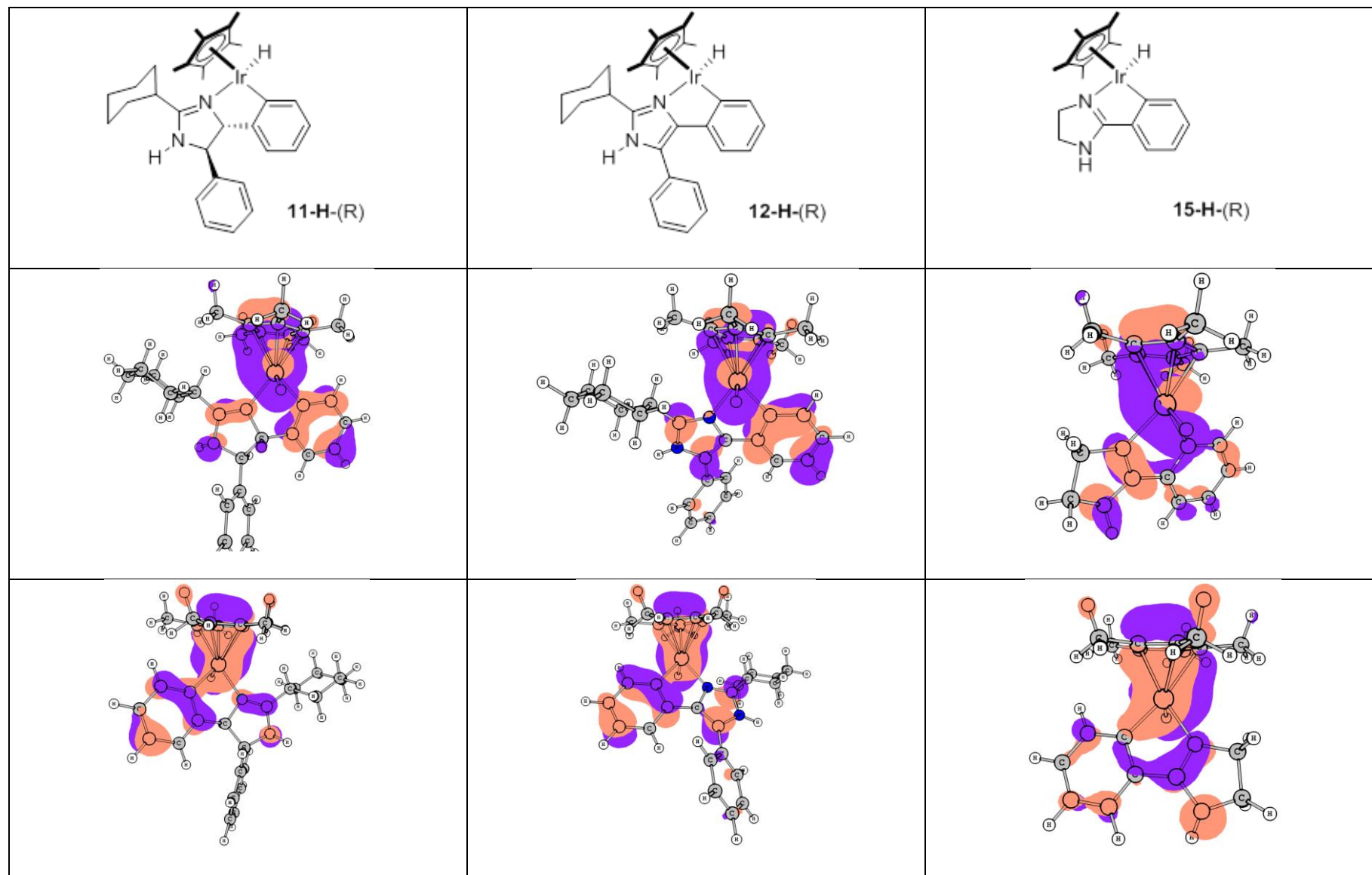


Figure 4.10: HOMO diagrams showing two orientations for the Ir-(R) configuration of each complex. The orange colour reflects a positive phase, whereas the purple colour refers to a negative phase, iso value range -0.02 – 0.02.

4.2.3 Location of transition states for the hydride transfer step

For each complex there are four possible transition states due to the stereogenic iridium (R and S) and there being two faces of the iminium for hydride delivery (*Re* and *Si*). Due to the inaccessibility of the ground state **11-H**(R), two transition states can be discounted. Below is summarised the transition states that were located (Figure 4.11).

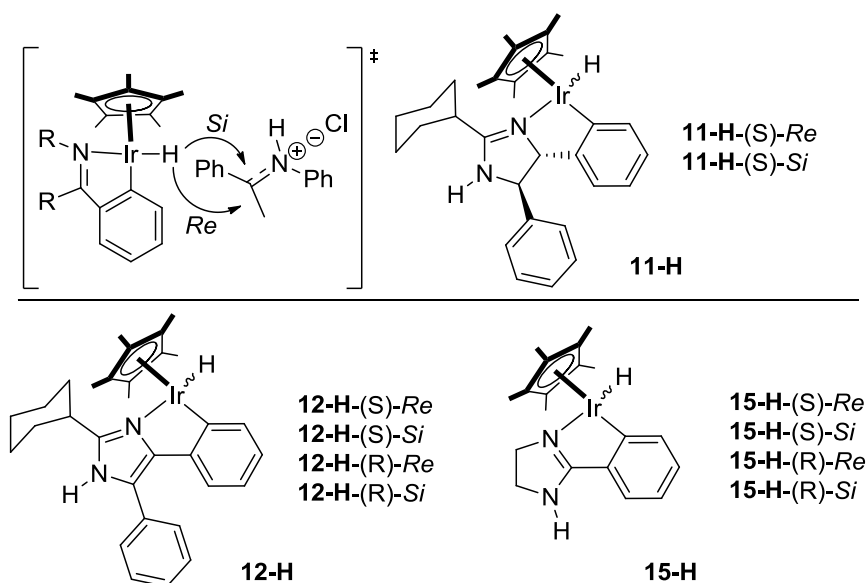


Figure 4.11: An overview of the transition states located for each complex.

All transition states were located and confirmed with only one imaginary frequency corresponding to delivering the hydride to the iminium carbon. The figure below shows an overview of the activation energy from ground state to the transition state for each of the complexes. A general trend is immediately obvious (Figure 4.12). The more reactive **15-H** has a 7-10 kcal/mol smaller activation energy than **12-H**, which has a much smaller gap of 2-4 kcal/mol to the non-reactive **11-H** (Figures 4.13-4.15). This trend matches the observed experimental results for the imine reduction (Table 4.3).

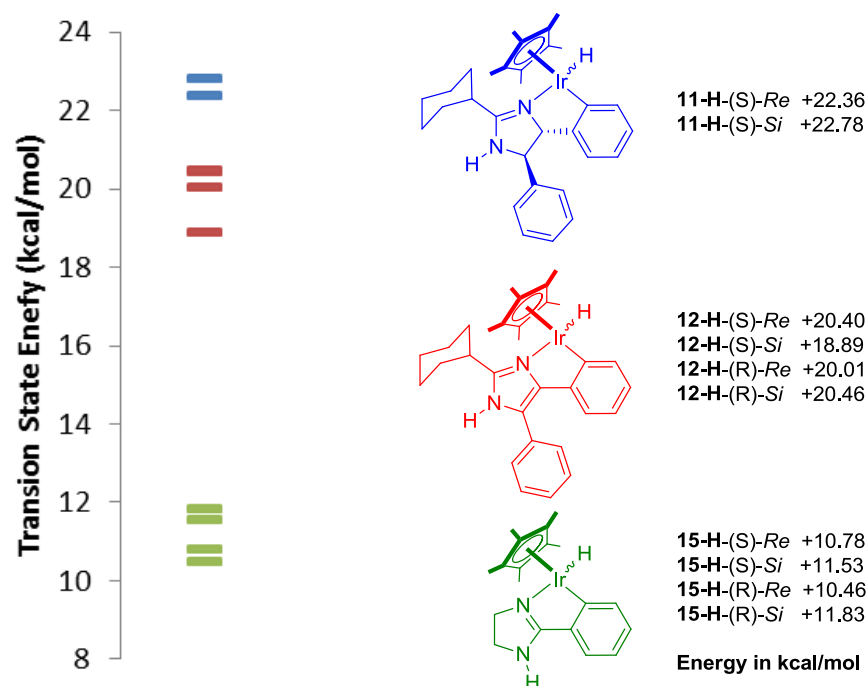


Fig 4.12: Energy profile showing the activation energy for complexes **11-H**, **12-H**, and **15-H**.

Energies relative to the starting materials **11-H/12-H/15-H** + 20.

Analysis and comparison of the transition state structures allowed for the factors influencing these energy differences to be elucidated. The main difference between **11-H** and **12-H** is the change from the imidazoline ring to a more conjugated imidazole ring; this has the effect of a change of structure. The imidazoline ring adopts a puckered confirmation, bringing the outer phenyl ring and cyclohexyl ring in closer proximity to the rings of the iminium in the transition state. When **11-H**-(S)-(Si) is compared directly to the analogous **12-H**-(S)-Si a difference in the contact distances between these rings and the iminium is seen (3.182 Å in **11-H** vs. 3.282 Å in **12-H**, distance measured between the two closest carbons on each of the rings) and consequently, a larger bond distance for the hydride to the carbon for delivery is observed (1.505 Å in **11-H** vs. 1.442 Å in **12-H**) (Figure 4.16).

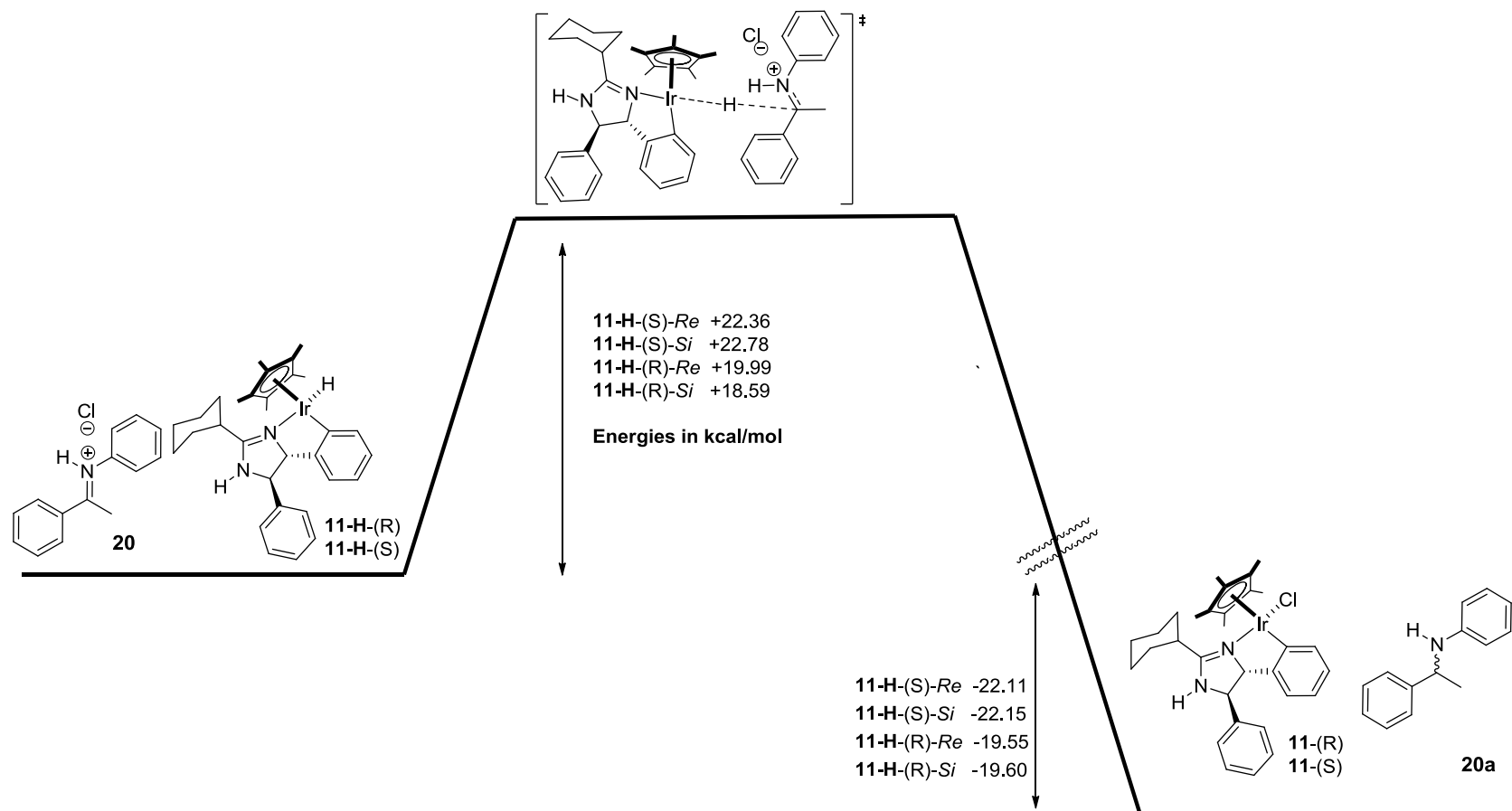


Figure 4.13: Energy profile for hydride delivery for **11-H**.

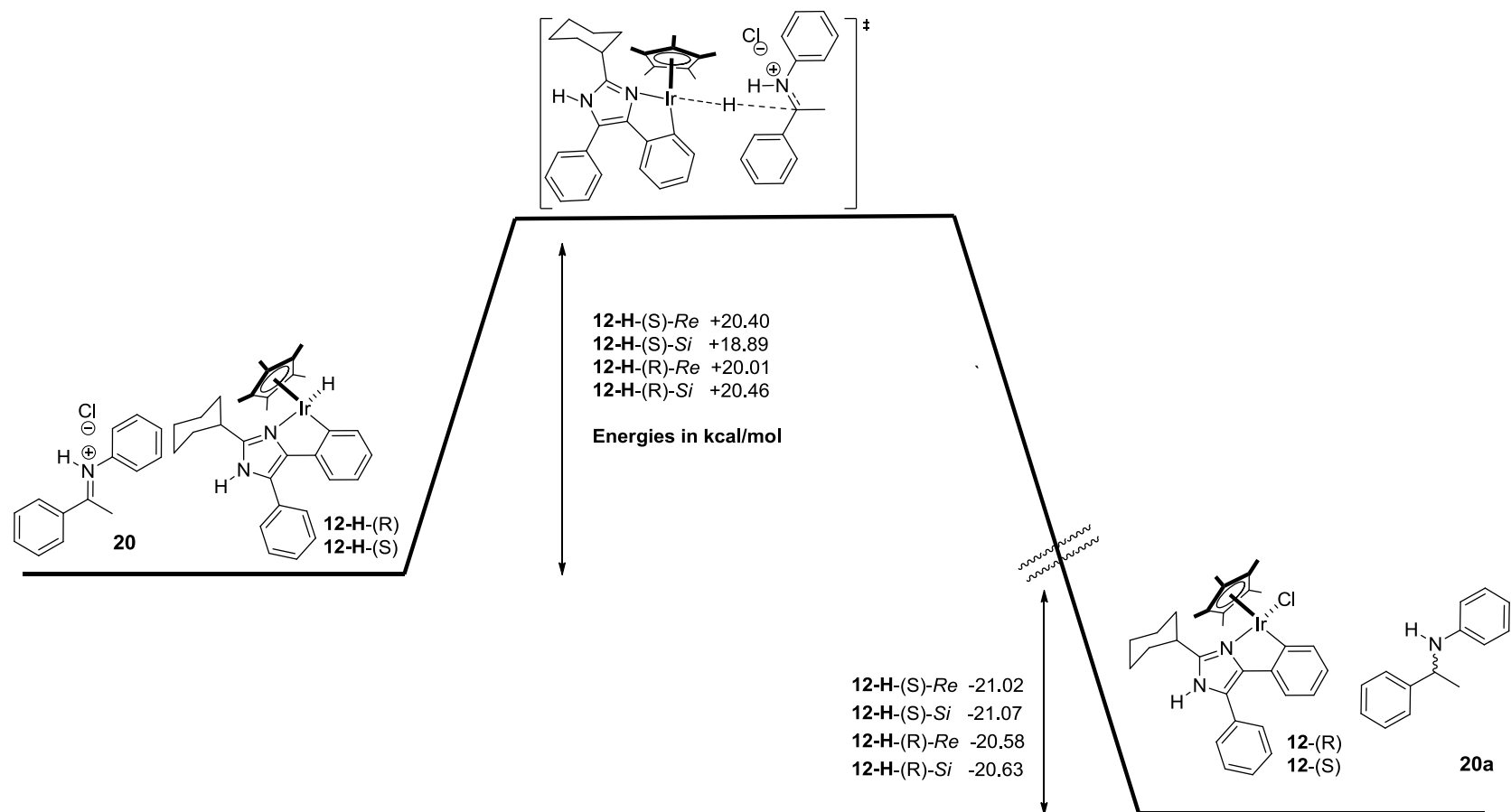


Figure 4.14: Energy profile for hydride delivery for **12-H**.

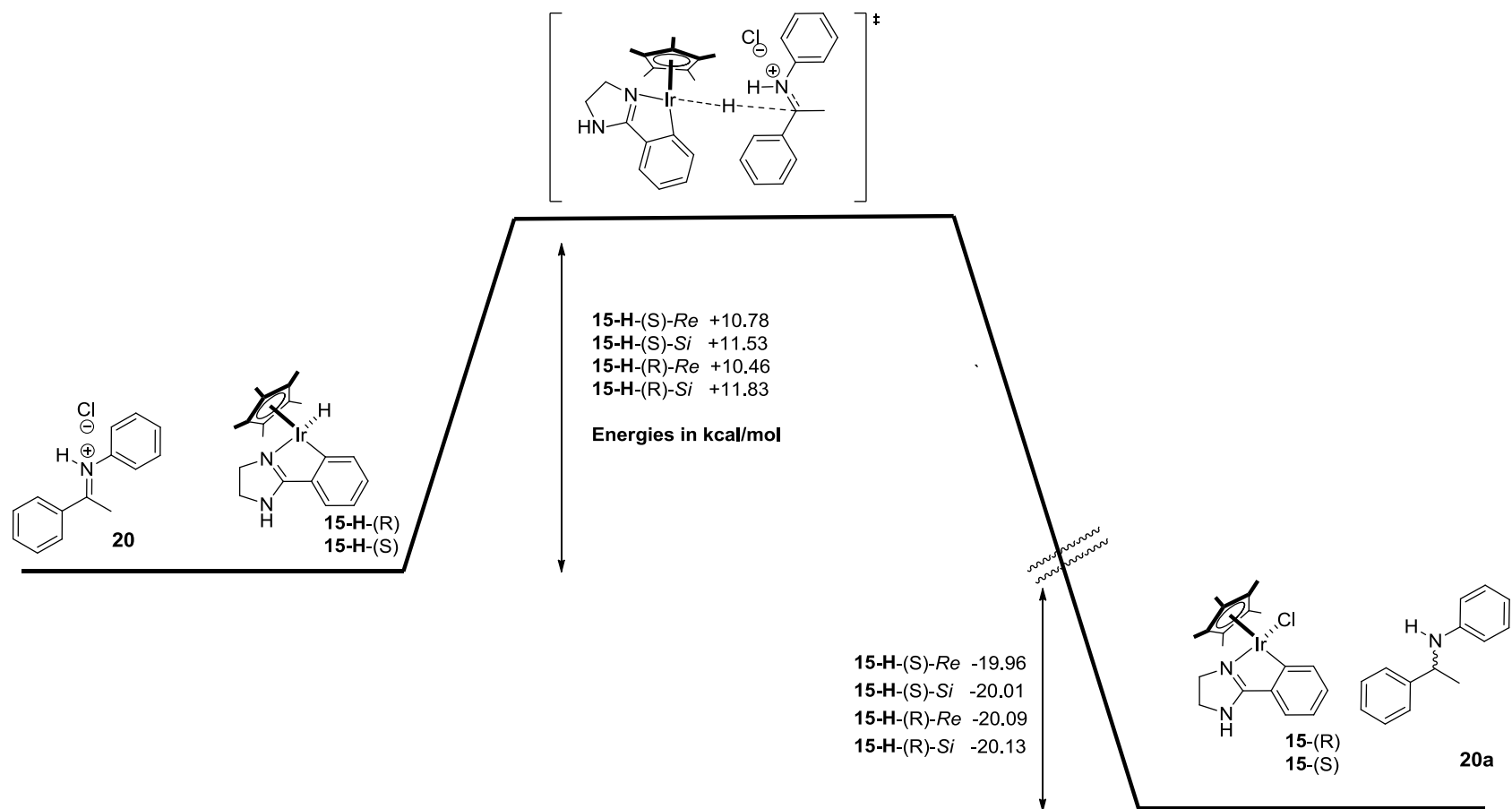


Figure 4.15: Energy Profile for hydride delivery for **15-H**.

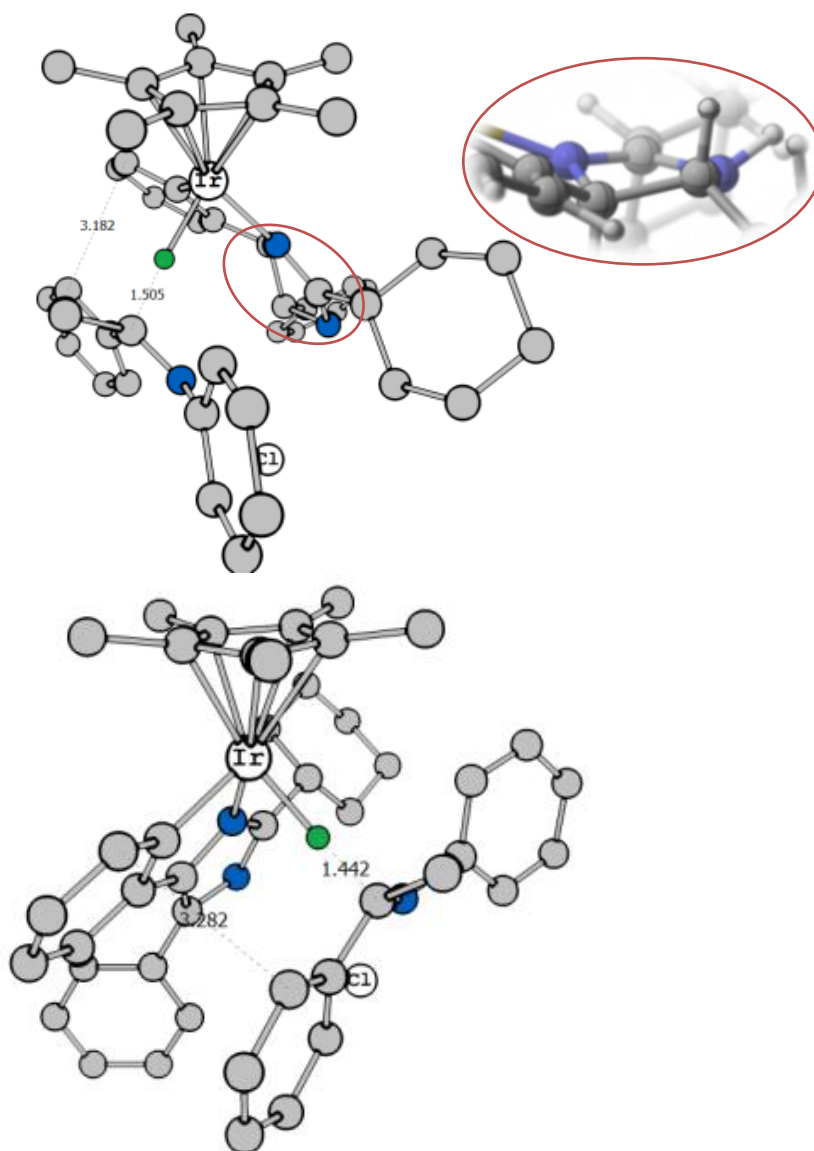


Figure 4.16: **11-H**-(S)-(Si) and **12-H**-(S)-Si showing hydride delivery distances of the transition states accounting for the energy difference. Change in shape of the imidazoline ring of **11-H** (inset). Green = hydride, blue = N, grey = C, remaining protons omitted for clarity.

When the transition states of **15-H** are analysed, the first most notable observation is the lack of the phenyl and cyclohexyl outer rings seen in the previous complexes (Figure 4.17). The larger gap between **12-H** and **15-H** cannot be solely attributed to this removal of the rings, as the complex **16**

possess the steric bulk **15-H** lacks and gives high activity (97% vs. 80%, Table 4.3 entries 5 & 6).

The difference in reactivity between **11-H** and **12-H** is a steric contribution. There is no trend seen in the change in charge (extracted from the natural bond order (NBO) analysis) from ground state to transition state when compared (Ir = -0.095(**11-H**, average) vs. -0.101(**12-H**, average)) This steric difference gives an energy difference in the transition states of **11-H** and **12-H** of 2-4 kcal/mol. In comparison there is a 7-10 kcal/mol difference between **12-H** and **15-H**. This leads to the conclusion that there must be more factors than just a steric effect present to account for this large difference.

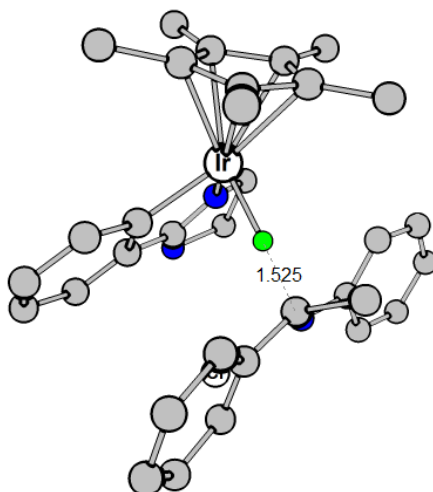


Figure 4.17: Transition state for **15-H**-(S)-(Si).

Comparison of the NBO charges of the transition states of **15-H** with **12-H** and **11-H** gives information on how the charge is delocalized through the complexes. The change in charge on each of the key atoms from the ground state to the transition state gives an indication on how the ligand helps to stabilize the build-up of charge during the hydride transfer step (Table 4.5).

Table 4.5: NBO charge comparison of ground states and transition states of complexes **11-H**, **12-H** and **15-H**.

	Charge			
Transition State	Ir	Hydride	N-Ir	C-Ir
11-H -(S)- <i>Re</i>	0.51	0.003	-0.516	-0.155
11-H -(S)- <i>Si</i>	0.514	0.011	-0.533	-0.152
12-H -(S)- <i>Re</i>	0.508	0.019	-0.479	-0.132
12-H -(S)- <i>Si</i>	0.518	0.032	-0.489	-0.126
12-H -(R)- <i>Re</i>	0.518	0.031	-0.489	-0.126
12-H -(R)- <i>Si</i>	0.508	0.019	-0.479	-0.132
15-H -(R)- <i>Re</i>	0.51	0.003	-0.521	-0.106
15-H -(R)- <i>Si</i>	0.514	0.008	-0.512	-0.116
15-H -(S)- <i>Si</i>	0.51	0.003	-0.522	-0.106
15-H -(S)- <i>Re</i>	0.514	0.007	-0.521	-0.114
Ground State	Ir	Hydride	N-Ir	C-Ir
11-H -(S)	0.417	-0.057	-0.474	-0.133
11-H -(R)	0.408	-0.019	-0.473	-0.136
12-H -(S)	0.411	-0.031	-0.457	-0.117
12-H -(R)	0.411	-0.031	-0.456	-0.117
15-H -(R)	0.426	-0.03	-0.49	-0.104
15-H -(S)	0.426	-0.03	-0.49	-0.104
Difference from TS	Ir	Hydride	N-Ir	C-Ir
11-H -(S)- <i>Re</i>	-0.093	-0.06	0.042	0.022
11-H -(S)- <i>Si</i>	-0.097	-0.068	0.059	0.019
12-H -(S)- <i>Re</i>	-0.097	-0.05	0.022	0.015
12-H -(S)- <i>Si</i>	-0.107	-0.063	0.032	0.009
12-H -(R)- <i>Re</i>	-0.107	-0.062	0.033	0.009
12-H -(R)- <i>Si</i>	-0.097	-0.05	0.023	0.015
15-H -(R)- <i>Re</i>	-0.084	-0.033	0.031	0.002
15-H -(R)- <i>Si</i>	-0.088	-0.038	0.022	0.012
15-H -(S)- <i>Si</i>	-0.084	-0.033	0.032	0.002
15-H -(S)- <i>Re</i>	-0.088	-0.037	0.031	0.01

During the hydride transfer the iridium atom experiences a build-up of positive charge; the NBO analysis shows this increase for all complexes from the ground state to transition state. There is a smaller change in this charge on the iridium for **15-H** than the other two complexes on average (-0.086 (**15-H**) vs. -0.095 (**11-H**) & -0.102 (**12-H**)). This trend also extends to the hydride atom (-0.035 vs. -0.064 & -0.056), with the more positive charge in the transition state being better stabilised by complex **15**.

Analysis of the nitrogen and carbon atoms immediately next to the iridium illustrates the conjugation present in the ligand. The conjugation present in **15-H** allows it to spread the resulting negative charge build-up over the ligand, giving a small change in charge at the N and C (0.29 and 0.004). The cross conjugation in **12-H** does not allow for stabilisation of the metal centre. It does, however, allow for the charge to be distributed across the ligand with the N and C having a small change in charge in comparison to the non-conjugating ligand of **11-H** (0.30 and 0.12 **12-H**) vs. (0.051 and 0.021 **11-H**).

This demonstrates that the conjugated ligand of **15-H** helps to stabilise the build-up of charge on the iridium in the transition state compared to **11-H** and **12-H**, proving that the presence of conjugation involving the iridium and the ligand is crucial.

4.3 Conclusions and future work

This study has shown that a combination of steric and electronic factors influences the reactivity of a series of cyclometallated iridium complexes. Small changes in the nature of the arylimidazoline ring of the ligand can

change the shape of the catalyst causing reduced reactivity. The presence of conjugation is however, the major factor in reactivity differences. Conjugation that involves both the ligand and the metal centre is crucial to stabilising the positive charge build up that occurs in the hydride transfer step.

Future work should focus on the modelling of the larger conjugated complex **16** for the same hydride transfer to **20**, to ascertain if the transition states fit into the trend so far observed. The same process should also be carried out for **12** with the attached phenyl and cyclohexyl rings removed, to quantify the exact magnitude of the steric effect. Modelling of the same complex set for hydride transfer to substrates **17** and **18** should also add more evidence for the importance of the presence of conjugation. This work should enable the more effective design of catalysts for hydrogen transfer reactions.

4.4 Experimental

4.4.1 Computational details

All structures were optimized at the density functional theory (DFT) level by using the B3LYP functional.³⁶⁻³⁹ Initial structures were generated by use of a conformation distribution search carried out in Spartan '08 using molecular mechanics and a MMFF force field with default parameters.⁴⁰ The structures with a Boltzmann distribution greater than >0.2 were optimised using PC GAMESS.⁴¹ For all the optimisations the 6-31G** basis set was used for all atoms except Ir. Relativistic effects for Ir were addressed by using LANL2DZ effective core potential (ECP) together with the LANL2DZ basis set.^{42,43}

Vibrational frequency calculations were carried out to confirm the nature of the stationary point on the potential energy surface. Energy minima were confirmed with no imaginary frequencies less than -50 cm^{-1} . To locate the transition state certain inter-atomic distances were initially fixed as appropriate (e.g. C to H(Hydride), 1.6 \AA), the rest of the molecule optimised and the hessian calculated at the optimized coordinates. The structure and associated Hessian were used as an input to saddle point calculation (with no constraints) to locate the transition states. Transition states were confirmed by only one imaginary frequency with the associated atomic motion consistent with the mechanism. Partial atomic charges were calculated by NBO analysis.⁴⁴

All calculations were performed on the University of Liverpool linux clusters and graphical representations were generated using Chemcraft⁴⁵ and CYLview.⁴⁶

4.4.2 XYZ coordinates for all structures

All XYZ coordinates for the named structures involved in the calculations can be found in the attached electronic information.

4.5 References

- (1) Trofimenko.S *Inorg Chem* **1973**, 12, 1215.
- (2) Bruce, M. I. *Angew. Chem., Int. Ed.* **1977**, 16, 73.
- (3) Cope, A. C.; Siekman, R. W. *J Am Chem Soc* **1965**, 87, 3272.
- (4) Bennett, M. A.; Milner, D. L. *Chem. Commun.* **1967**, 581.
- (5) Keim, W. J. *Organomet. Chem.* **1968**, 14, 179.
- (6) Knoth, W. H.; Schunn, R. A. *J. Am. Chem. Soc.* **1969**, 91, 2400.
- (7) Levison, J. J.; Robinson, S. D. *J. Phys. Chem. A* **1970**, 2947.
- (8) Ainscough, E.; Robinson, S. D.; Levison, J. J. *J. Phys. Chem. A* **1971**, 3413.
- (9) Jerphagnon, T.; Gayet, A. J.; Berthiol, F.; Ritleng, V.; Mrcic, N.; Meetsma, A.; Pfeffer, M.; Minnaard, A. J.; Feringa, B. L.; de Vries, J. G. *Chem. Eur. J.* **2009**, 15, 12780.
- (10) Arita, S.; Koike, T.; Kayaki, Y.; Ikariya, T. *Angew Chem Int Ed Engl* **2008**, 47, 2447.

- (11) Arita, S.; Koike, T.; Kayaki, Y.; Ikariya, T. *Organometallics* **2008**, *27*, 2795.
- (12) Baratta, W.; Da Ros, P.; Del Zotto, A.; Sechi, A.; Zangrando, E.; Rigo, P. *Angew. Chem., Int. Ed.* **2004**, *43*, 3584.
- (13) Sortais, J. B.; Ritleng, V.; Voelklin, A.; Holuigue, A.; Smail, H.; Barloy, L.; Sirlin, C.; Verzijl, G. K.; Boogers, J. A.; de Vries, A. H.; de Vries, J. G.; Pfeffer, M. *Org Lett* **2005**, *7*, 1247.
- (14) Pannetier, N.; Sortais, J. B.; Dieng, P. S.; Barloy, L.; Sirlin, C.; Pfeffer, M. *Organometallics* **2008**, *27*, 5852.
- (15) Crabtree, R. H. *Organometallics* **2011**, *30*, 17.
- (16) Choi, J.; MacArthur, A. H.; Brookhart, M.; Goldman, A. S. *Chem Rev* **2011**, *111*, 1761.
- (17) Gupta, M.; Hagen, C.; Flesher, R. J.; Kaska, W. C.; Jensen, C. M. *Chem. Commun.* **1996**, 2083.
- (18) Gupta, M.; Hagen, C.; Kaska, W. C.; Cramer, R. E.; Jensen, C. M. *J Am Chem Soc* **1997**, *119*, 840.
- (19) Gupta, M.; Kaska, W. C.; Jensen, C. M. *Chem. Commun.* **1997**, 461.
- (20) Xu, W. W.; Rosini, G. P.; Gupta, M.; Jensen, C. M.; Kaska, W. C.; Krogh-Jespersen, K.; Goldman, A. S. *Chem. Commun.* **1997**, 2273.
- (21) Liu, F. C.; Pak, E. B.; Singh, B.; Jensen, C. M.; Goldman, A. S. *J Am Chem Soc* **1999**, *121*, 4086.
- (22) Zhu, K. M.; Achord, P. D.; Zhang, X. W.; Krogh-Jespersen, K.; Goldman, A. S. *J Am Chem Soc* **2004**, *126*, 13044.

- (23) Fortman, G. C.; Slawin, A. M. Z.; Nolan, S. P. *Organometallics* **2011**, *30*, 5487.
- (24) Wang, C.; Pettman, A.; Basca, J.; Xiao, J. *Angew Chem Int Ed Engl* **2010**, *49*, 7548.
- (25) Jiang, J. X.; Wang, C.; Laybourn, A.; Hasell, T.; Clowes, R.; Khimyak, Y. Z.; Xiao, J.; Higgins, S. J.; Adams, D. J.; Cooper, A. I. *Angew Chem Int Ed Engl* **2011**, *50*, 1072.
- (26) Wang, C.; Villa-Marcos, B.; Xiao, J. *Chem. Commun.* **2011**, *47*, 9773.
- (27) Barnard, J. H.; Wang, C.; Berry, N. G.; Xiao, J. L. *Chem. Sci.* **2013**, *4*, 1234.
- (28) Wei, Y. W.; Xue, D.; Lei, Q.; Wang, C.; Xiao, J. L. *Green Chem.* **2013**, *15*, 629.
- (29) Wang, C.; Chen, H.-Y. T.; Bacsa, J.; Catlow, C. R. A.; Xiao, J. *Dalton Trans.* **2013**, *42*, 935.
- (30) Wu, J.; Barnard, J. H.; Zhang, Y.; Talwar, D.; Robertson, C. M.; Xiao, J. *Chem. Commun.* **2013**, *49*, 7052.
- (31) Clayden, J.; Greeves, N.; Warren, S. G. *Organic chemistry*; 2nd ed.; Oxford University Press: Oxford ; New York, 2012.
- (32) Davies, D. L.; Al-Duaij, O.; Fawcett, J.; Giardiello, M.; Hilton, S. T.; Russell, D. R. *Dalton Trans.* **2003**, 4132.
- (33) Davies, D. L.; Donald, S. M. A.; Al-Duaij, O.; Macgregor, S. A.; Polleth, M. *J Am Chem Soc* **2006**, *128*, 4210.
- (34) Boutadla, Y.; Davies, D. L.; Jones, R. C.; Singh, K. *Chem. Eur. J.* **2011**, *17*, 3438.

- (35) Phelan, N. F.; Orchin, M. *J. Chem. Educ.* **1968**, 45, 633.
- (36) Becke, A. D. *J. Chem. Phys.* **1993**, 98, 5648.
- (40) Lee, C. T.; Yang, W. T.; Parr, R. G. *Phys. Rev. B* **1988**, 37, 785.
- (38) Vosko, S. H.; Wilk, L.; Nusair, M. *Can. J. Phys.* **1980**, 58, 1200.
- (39) Stephens, P. J.; Devlin, F. J.; Chabalowski, C. F.; Frisch, M. J. *J. Phys. Chem.* **1994**, 98, 11623.
- (40) <http://wavefun.com/products/spartan.html>.
- (41) <http://classic.chem.msu.su/gran/gamess/index.html> A. A. Granovsky *Firefly v7.1.G*
- (42) Feller, D. *J. Comput. Chem.* **1996**, 17, 1571.
- (43) Basis sets were used as from the Basis set exchange : Schuchardt, K. L.; Didier, B. T.; Elsethagen, T.; Sun, L. S.; Gurumoorthi, V.; Chase, J.; Li, J.; Windus, T. L. *Journal of Chemical Information and Modeling* **2007**, 47, 1045.
- (44) <http://www.chem.wisc.edu/~nbo5/>.
- (45) <http://www.chemcraftprog.com>.
- (46) <http://www.cylview.org> CYLview 1.0b; C. Y. Legault, **2009**.

Chapter 5

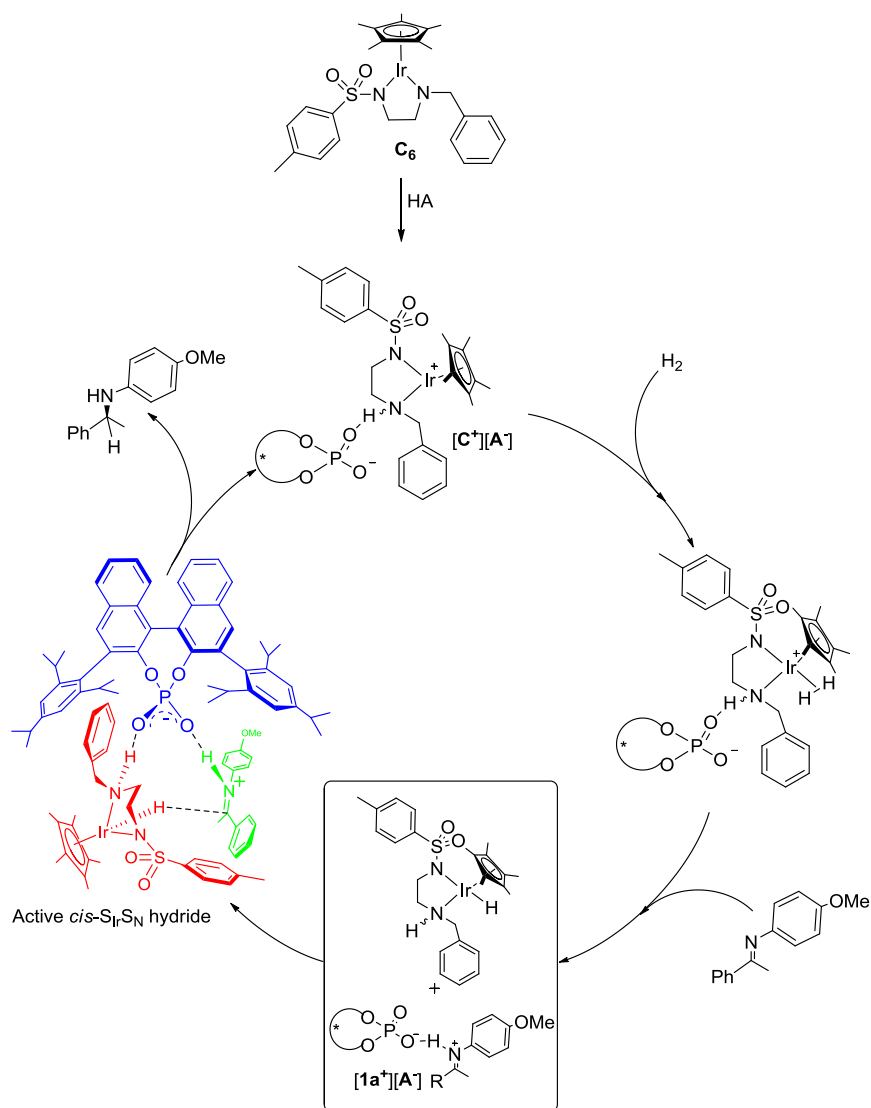
Conclusions and Future Perspectives

This thesis has described the investigation of the mechanisms of hydrogenation of imino bonds. The mechanism of action for a newly developed cooperative system involving both an achiral metal catalyst and chiral phosphoric acid has been determined in Chapters 2 & 3. The mechanism (Scheme 1) was shown to go via fast generation of four different hydrides from the starting 16 electron catalyst. From these four, only one *cis*-hydride was determined to be the active species giving the correct amine configuration. A combination of NMR studies and subsequent constrained computational modelling, showed that a range of non-covalent interactions were responsible for the selectivity observed.

The chiral acid was shown to be responsible for retarding the rate in comparison to other anions but this came with gain of selectivity. The chiral acid therefore plays a dual role of protonating the catalyst and helping enable selectivity in the key hydride transfer step.

The work in Chapter 4 explored how levels of conjugations present in a range of cyclometallated iridium complexes influenced reactivity of hydrogen transfer reactions. By modelling the hydride transfer step of the reduction of an iminium cation it was shown that a combination of steric and electronic factors

determined reactivity patterns. Ligands that had the ability to stabilise the positive charge build up on the metal centre through conjugation during the hydride transfer had increased reactivity. This was reflected in the trend of the barrier to reaction for the complexes matching that of the experimental results.



Scheme 1: The mechanism established for the asymmetric hydrogenation of imines going via a selective hydride delivery, involving both the chiral acid and *cis*-hydride.

The knowledge gained from this research can hopefully be used to help aid the design of future catalytic systems. The systems investigated have shown that a combination of factors help influence both reactivity and selectivity, such as steric effects, non-covalent interaction and electronic properties of the ligand. These should be taken into consideration when new catalysts are developed as they can play a dual role in helping to activate substrates and conversely deactivating reactive species such as the *trans*-hydrides in Chapters 2-3.

There is still a need for the asymmetric hydrogenation of imino bonds to move away from the more expensive metals such as iridium and target cheaper more sustainable metals. While examples have been reported with iron, the substrate scope is still limited. The exploitation of a range of interactions identified in this work could help to access cheaper and greener catalysts.

Computational modelling also has a role to play in catalyst discovery. The calculated tertiary structure in Chapter 3 along with the transition states located in Chapter 4 show the points where selectivity is achieved be it a hydrogen bonding donor or steric blocking group. It could then be envisaged that a strategy similar to pharmacophore searching in drug design could, with the right database, allow for the location of new catalysts. This knowledge led strategy for catalyst searching would allow for potential lead candidates to be located at relatively low cost compared to the current methods.